Construction and Calibration of a Setup for Micro-Pattern Gaseous Detectors Using UV Laser Photoelectrons

Dissertation zur Erlangung der Doktorwürde
Vorgelegt von

Kim Temming

Dezember 2013

Fakultät für Mathematik und Physik
Albert-Ludwigs-Universität Freiburg im Breisgau

After the discovery of the Higgs boson at the Large Hadron Collider (LHC) in summer 2012, the properties and couplings of the newly found particle need to be determined. To deliver the necessary amount of data, the LHC will raise its luminosity significantly and new detector technologies are needed that can withstand the demands due to the increased particle flux. New types of gaseous detectors like Micro Pattern Gaseous Detectors (MPGD) and especially the Micromegas that are foreseen for the ATLAS Muon New Small Wheel upgrade, show very good rate capabilities so far.

A test setup to investigate the properties of Micromegas has been designed and built. The setup uses photoelectrons created by a UV laser in the drift volume as the primary charge to probe the detector. The creation points and times are precisely known and the setup is independent of test beams. It includes a reference measurement system based on multi-wire technology and has been commissioned and fully calibrated.

A Micromegas test candidate unit with 8 different readout geometry zones and an additional cathode layer has been designed and the performance of a prototype was intensively investigated. Gain studies as well as drift and diffusion studies have been carried out successfully.

Studies and Garfield simulations regarding the discharge behavior of the Micromegas test candidate and the supplementary cathode on the bottom of the detector have been carried out and indicate a controllable influence on the electric field configuration in the amplification area by the additional potential.

Contents

Preface

In summer of 2012, the discovery of the Higgs boson at CERN (Organisation Européenne pour la Recherche Nucléaire) drew a lot of attention to particle physics and especially to the fundamental theories that try to explain the origin of the universe and the constituents and interactions of matter. Although there are still many open questions, the Standard Model of particle physics, that represents our current understanding of the processes and structures on the smallest sub-atomic scales, is consolidated further by the discovery of the Higgs boson. This confirmation of the Higgs theory had such a great impact on the world of theoretical physics and science in general, that Peter Higgs and François Englert were awarded the Nobel Prize in physics this year, 2013. Their relativistic quantum field theory formulated in 1964 includes an additional field, the Higgs field, that spontaneously breaks the symmetry group to allow gauge bosons to acquire a non-zero mass.

The prize gives credit to the scientists that formulate theories and try to describe with them the processes that happen in nature, but also in general to all the experimental physicists and technicians that build huge accelerators and experiments like ATLAS and CMS. Without the constant progress in the development of new acceleration and detection methods over the years and decades, pushing the technical limits further and further, this discovery would not have been possible. The increase of the magnetic field strength in the accelerator ring, better and more precise beam guidance for the LHC as well as the design and construction of the large experiments with new, reliable and extremely precise detectors, are the achievement of an international collaboration of scientists.

This pursuit of advancement may never come to a rest, since new questions and ideas pose new and different challenges to the world of experimental particle physics. To determine the characteristics of the newly found particle, like couplings and spin, higher statistics are necessary. Therefore the LHC will undergo a luminosity upgrade in several phases, which will push the rate capability of the experiments to its limits and even further. The upgrade and exchange of detector parts with new and better technologies are inevitable to guarantee best performance of the machines.

In the context of the LHC high luminosity upgrade, the Micro-Pattern Gaseous Detectors and especially the Micromegas are new and promising technologies. Micromegas are foreseen to be used to replace conventional drift tubes in the New Small Wheel upgrade, a part of the ATLAS Muon detection system.

This thesis focuses on the setup and calibration of a test chamber to study the properties of MPGDs like the Micromegas. The goal is to be able to determine and improve their character-

istics without the necessity of test beams, with a high precision and reproducibility of results and a compact setup. The primary ionization, that is used as a probe charge, is produced via photoelectric effect on aluminium strips with the help of a UV laser in a gas-filled drift volume. Part of the structure that creates the drift field can be used as a multi wire proportional chamber acting as a reference readout system. It provides a quantitative calibration of the photoelectron creation process and helps to compare the results with other measurements that were achieved under different conditions.

The thesis comprises 6 chapters. Chapter 1 gives an overview about the present knowledge of particle physics, the Standard Model. It presents the accelerator LHC and gives insights into the technical details of the ATLAS experiment with focus on the muon detectors. The motivation for the high luminosity upgrade of the LHC is given, in particular for the New Small Wheel muon upgrade. Finally recent results on the Higgs physics are given and a short outlook regarding the future direction after the upgrade is given. Chapter 2 briefly illustrates the basic working principles of gaseous detectors for particle detection and introduces Micro-Pattern Gaseous Detectors and particularly Micromegas with their special characteristics and challenges.

The setup of the MPGD test chamber and field simulations to ensure best functionality of the reference system are explained in chapter 3. In the fourth chapter, measurements and approaches to understand and calibrate the reference readout system and all conversion factors that are describing the operation of the test chamber are explained. The fifth chapter presents a custom-built Micromegas with different readout configurations and a first set of measurements, like gain studies. Also drift time and diffusion of the primary electrons in the drift space have been investigated. Moreover, studies regarding the discharge affinity of the custom-built Micromegas under the influence of an additional cathode potential are shown.

Chapter 6 gives a summary of the main activities and results with a short outlook regarding the continuation of this work and future measurement possibilities. Several appendices contain more technical information and detailed field and signal calculations.

Parts of the work in this thesis, in particular the setup and the reference readout gain studies, have already been presented by me in oral contributions at the IEEE 2011 Nuclear Science Symposium and Medical Imaging Conference (NSS/MIC), Valencia [1] and IEEE 2012 Nuclear Science Symposium and Medical Imaging Conference (NSS/MIC), Anaheim [2].

1. Introduction

This chapter gives a short overview over the present status of the fundamental theory of particle physics, the Standard Model. The latest confirmation of this theory, the discovery of the Higgs boson, still leaves open questions and room for physics beyond the Standard Model, which is also discussed briefly. The Lange Hadron Collider (LHC) at CERN (Organisation Européenne pour la Recherche Nucléaire), the biggest and most prosperous particle collider under operation these days, is introduced. One of the two multi-purpose LHC experiments ATLAS (**A T**oroidal **L**HC **A**pparatu**S**) is described in detail. Results of the first physics run are presented and a short outlook into the future of ATLAS during the phase of the super-LHC is given. Also an overview about the future of the LHC with its high-luminosity upgrade is presented.

1.1. The Standard Model

The Standard Model of particle physics (SM) has been developed during the past 50 years and is a quantum field theory that describes most processes and interactions in the universe regarding visible matter. In this theory, all observable matter is composed of 12 elementary particles (and their antiparticles). They can be divided into 6 quarks (**u**p, **d**own, **c**harm, **s**trange, **t**op and **b**ottom) and 6 leptons (electron (e), muon (μ) and tau (τ), and their corresponding neutrinos ν_e, ν_μ and ν_τ). A sub-division into 3 families is possible, as shown in table 1.1. All quarks and leptons are fermions and carry spin $\frac{1}{2}$. The electric charge of the neutrinos is 0, while all other leptons carry a charge of -1 (antiparticles +1). Quarks have either charge $-\frac{1}{3}$ or $+\frac{2}{3}$. Their masses span several orders of magnitude. While neutrinos have been measured to have a mass below $1\,\mathrm{eV}$ [3], the quark and the charged lepton mass increases in the three families from electron to tau.

Table 1.1.: Quantum numbers of quarks and leptons (fermions) in the Standard Model

fermions	family			electric charge in units of e	color	spin
	1	2	3			
leptons	ν_e	ν_μ	ν_τ	0	-	$\frac{1}{2}$
	e	μ	τ	-1		
quarks	u	c	t	$+\frac{2}{3}$	r, b, g	$\frac{1}{2}$
	d	s	b	$-\frac{1}{3}$		

Table 1.2.: The exchange bosons in the Standard Model

interaction	couples to	exchange boson	mass	spin
strong	color	8 gluons (g)	0	1
electromagnetic	electric charge	photon (γ)	0	1
weak	weak charge	$W^{\pm}, Z^0$	$\approx 10^2$ GeV [3]	1

Besides the particles listed above, the Standard Model describes three different types of forces between particles: the strong force, described by QCD, the electrodynamic interaction, involving electrically charged particles, and the weak interaction, which affects all particles. The forces are described by the exchange of mediator or gauge bosons. The electromagnetic and weak interactions have already been merged by Glashow, Salam and Weinberg in the 1960's forming a single theory of electroweak unification (GSW model). Table 1.2 shows the corresponding charges and exchange bosons of the three interactions of the Standard Model. The Standard Model mathematically is a gauge-invariant theory based on the symmetry group SU(3) × SU(2) × U(1). It predicts the existence of four massless gauge bosons, which stands in contradiction to the large $W^{\pm}$ (91.2 GeV) and Z^0 (80.2 GeV) masses [3], which have been measured in the early 1980's at LEP2 and have been confirmed by all later experiments. The solution to this can be a mechanism called spontaneous symmetry breaking, if at least one additional massive particle, the Higgs boson H is inserted into the theory.

Such a Higgs-like particle has been found in summer 2012 by ATLAS and CMS in the mass region of 125 GeV [4]. It still needs to be determined by further measurements, whether this particle is the Standard Model Higgs particle or if it has different properties and may be evidence for other new physics.

Open Questions: Physics Beyond the Standard Model
No experiment so far showed proof that the Standard Model is incorrect in its fundamental structures. It delivers precise predictions for the strong and electroweak interaction and describes nature in a very elegant mathematical framework. But there are several open questions that it cannot answer in its present state. This leads to the assumption that the Standard Model of Particle Physics cannot be the last and final theory. It might be regarded as a "low energy approximation" of some theory, and must be complemented by more general theories.

- Visible and stable matter in the universe consist of only electrons, up- und down-quarks. Why are there 3 generations of leptons and quarks that seemingly only differ in their increasing masses? Why are there for both, leptons and quarks, the same number of generations, while they do not seem to be linked otherwise?

- The Standard Model in its present form includes 18 free parameters that have to be determined by experiments and cannot be calculated from the theory. This is not considered

particularly elegant by many theoreticians and leads to the question, if the values for the free parameters are somehow correlated.

- The masses of the Standard Model particles differ by several orders of magnitude and there is no intrinsic reason for this in the theory.

- Why is physics not symmetric between matter and antimatter? CP-violation is not strong enough to explain the matter-domination in the universe. Where did all the antimatter go?

- Gravitation, an important force in macroscopic processes, has far less influence in microscopic interactions because of its weakness, but at higher energies gravitational quantum effects become stronger. But so far, all attempts to include it into a quantum field theory have failed and gravity is not included in the Standard Model.

- The *fine tuning* problem of the Standard Model: Contributions of loop-corrections to the Higgs mass are leading to very high values for the Higgs mass in loop calculations, while it has been found to be around 125 GeV by ATLAS and CMS at CERN. This issue can be solved by an extremely precise 'fine tuning' of some parameters in this calculation. But this is considered to be 'unnatural' by many physicists.

- Closely related to the previous is the *hierarchy* problem: Why is the electroweak scale where W/Z (about 1 TeV) physics is important so much less than the Planck scale (around 1.22×10^{19} GeV)?

- A closer look at the couplings of the 3 forces in the Standard Model reveals that they are basically arbitrary and do not unify in a single point at higher energies. A Grand Unified Theory (GUT) would provide such unification of the couplings, based on a more fundamental symmetry group that might be broken at lower energies.

- It is known from astroparticle physics experiments that luminous (baryonic) matter can only make up about 4% of the total matter density. About 21% are assigned to be Cold Dark Matter (CDM), while the remainder is called Dark Energy, but the Standard Model does not explain either of the latter two.

There are several possible new theories to extend the Standard Model and explain some of the questions above. The two most commonly favoured theories are the following:

Super Symmetry (SUSY)

SUSY is a space-time symmetry and postulates the existence of a supersymmetric partner for all Standard Model particles that only differs in its spin. The assigned operator Q changes the spin of a Standard Model particle by $1/2$ which changes fermions into bosons and vice versa. This establishes a symmetry between bosons and fermions, which results in a very elegant theory. The particles and their supersymmetric partners (sparticles) are expected to have the same masses, since the only difference should be the spin, but so far, no sparticles have been found in

experiments. This leads to the assumption that the symmetry must be broken at some point. The supersymmetric partners cannot have been already found, since the SUSY theory predicts a partner for every Standard Model particle known so far. In addition, SUSY has a need for at least two Higgs-doublets to support the masses of up- and down-quarks and to cancel out gauge anomalies. SUSY would provide solutions to the following open questions in the Standard Model:

- Fine-tuning problem: The divergences in the mass terms cancel each other with less fine-tuning, while it is possible to find a construct to let SUSY break symmetry and allow for different gaugino and sfermion masses.

- Unification of gauge couplings: If the masses are in the order of $1\,\mathrm{TeV}$, a unification of the couplings around $10^{16}\,\mathrm{GeV}$ might be possible.

- Dark Matter could be explained by a large number of the lightest supersymmetric particle that has no further decay possibilities due to R parity conservation and therefore is stable in some SUSY models.

- Electroweak symmetry breaking occurs naturally in SUSY, while this mechanism does not exist in the Standard Model without SUSY and must be introduced artificially through certain parameters in the Higgs potential.

But also SUSY does not provide answers to solve the hierarchy problem, nor why there are three generations of fermions. Also particle masses and mixing angles are still to be determined in experiments. Furthermore, even more free parameters are introduced and until so far, data from LEP, the Tevatron and LHC Run 1 (ATLAS and CMS) has lead to the exclusion of SUSY particles up to a mass of about $700\,\mathrm{GeV}$ [5], [6] in most SUSY models and channels.

Other Physics beyond the Standard Model
Apart from Super Symmetry, there are more proposed theories that try to explain the open questions which the Standard Model cannot answer. Grand Unified Theories, based on larger symmetry groups try to implement the strong force as a third force to the gauge theory. New models like extensions of the Kaluza-Klein theory, string theories and superstring theories and more exotic ones, like loop quantum gravity, technicolor or other models of dynamical symmetry breaking could not be proved right or wrong yet.

1.2. The Large Hadron Collider at CERN (LHC)

The Large Hadron Collider is the world's largest and most energetic particle accelerator. It is a machine that serves the purpose to understand the constituents of matter and their interactions by colliding particles and investigating their remnants. This principle of measurement has already been used by Rutherford in the beginning of the 20th century. He proved that the atom is mostly empty by scattering α-particles on few layers of gold atoms. The amount of energy of
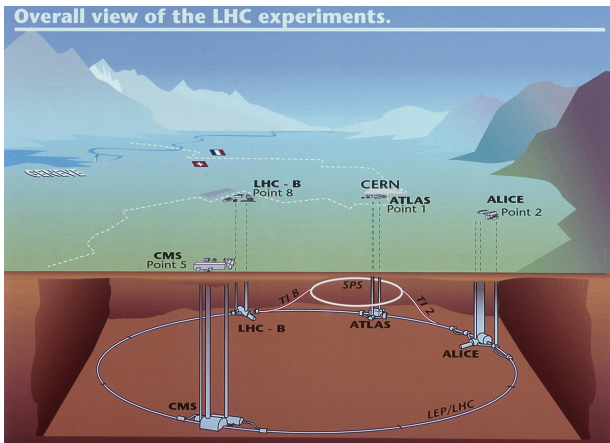
Figure 1.1.: The LHC accelerator and the four main experiments are situated at the Swiss border to France near Geneva. The LHC tunnel is about 85-90 m underground. Particles pass several stages of acceleration before entering the main LHC ring, including the SPS and PS accelerator. Picture from [7].

the particles, which was needed to penetrate the atoms of the gold foil, was small. Far higher energies are needed to crack up a nucleon and to resolve the structures inside it or to observe interactions of the quark-gluon plasma. While Rutherford could accelerate his α-particles to a few MeV with a linear accelerator, ring colliders have proven to have several advantages over the linear accelerators. With a circular structure it is possible to use so-called 'storage rings', where the particles are kept inside a closed vacuum beam pipe and accelerated by the same sections of the ring repeatedly until they reach the desired energy E. Then they are extracted from this pipe by a magnet and lead to the target. The center of mass energy E_{cm} compared to the particle beam energy is only about $\sqrt{E}$ for a fixed target experiment. To reach even higher collision energies, it is common to use two particle beams and let them collide head-on to use the full beam energy for the collision, which is nearly $2E$ in this case. Depending on mass and charge of the collision partners, they can be stored in the same ring of magnets, circulating in different directions in two separated beam pipes until they are brought to collision.

The LHC was built in the same 27 km long tunnel that hosted the Large Electron-Positron Collider (LEP) before. This e^+-e^- collider was shut down in November 2000, after a very successful running period, to be replaced by the new proton-proton (p-p) accelerator. The LHC also accelerates and collides lead ions ($^{208}\mathrm{Pb}^{82+}$) to investigate the quark-gluon plasma at a center-of-mass energy around 2.76 TeV per nucleon. Figure 1.1 shows a schematic drawing of the CERN accelerator complex, with locations of the main experiments at the LHC. The LHC is a double-ring collider that consists of 1230 superconducting dipole magnets in eight sections. The design allows for two beam pipes in the same magnet line with protons circulation in opposite directions. The magnets are operated at a temperature of 1.9 K which requires a large and efficient cryogenic system. The magnetic field can reach up to 8.33 T to allow a beam energy of 7 TeV per beam, which results in a center-of-mass energy of $\sqrt{s} = 14$ TeV. The LHC can reach far higher energies than the previous collider LEP ($\sqrt{s} = 105$ GeV), with the same circumference of the accelerator. This is possible due to the fact that the beam energy reachable by an e^+-e^- collider is limited by radiation losses. Since synchrotron radiation is proportional to γ^4 (with $\gamma = E/mc^2$ and m is the

mass of the accelerated particle) and protons are about a factor of 2000 heavier than electrons, the unavoidable synchrotron radiation losses are considerably lower for a proton-proton collider.

The LHC is designed for a bunch-crossing rate of 40 MHz which results in a time between two collisions of only 25 ns. Electronics, data transfer and triggering as well as data storage had to be adapted to this technical difficulty. Also event pile-up in the detectors of the experiments need to be handled. A design luminosity of $1 \times 10^{34} \, \mathrm{cm}^{-2} \, \mathrm{s}^{-1}$ allows for high collision rates in the experiments at the four Interaction Points of the LHC. These experiments are

- ATLAS (**A T**oroidal **L**HC **A**pparatu**S**) and CMS (a **C**ompact **M**uon **S**olenoid) are multi-purpose detectors. At the Interaction Points inside the detectors two beams collide head on that were circulating in opposite directions in the LHC ring. These experiments can provide deeper insights on the open questions for the Standard Model, such as the properties of the recently found Higgs particle as well as on other possible new phenomena in p-p collisions. While ATLAS and CMS share their goals and the overall experiment design, the single detector parts are using different technologies to provide the possibilities of technically unbiased measurements and cross-checks between their results.

- ALICE (**A L**arge **I**on **C**ollider **E**xperiment) is an experiment specifically designed and optimized to investigate the quark-gluon plasma that is produced in heavy ion collisions. This state represents a very early phase of the formation of the universe and can give deeper insights to the behavior of strongly interacting particles at high densities and temperatures.

- LHCb (**L**arge **H**ardon **C**ollider **b**eauty) is designed to measure properties of the decays of b-mesons and CP violation.

1.2.1. The ATLAS Experiment

This and the following sections describe and summarize the ATLAS experiment and the Myon System for a better overview and understanding of the general context of the work in this Thesis. Detailed descriptions can be found in the technical descriptions for ATLAS [8] and the Muon Spectrometer Technical Design Report [9].

With its height of 25 m and length of about 46 m ATLAS is the largest experiment in terms of covered detector volume. ATLAS is located at Interaction Point 1 at about 92.5 m underground (figure 1.1). The ATLAS detector is a complex machine consisting of many different subdetectors with different tasks in particle reconstruction and identification. An overview picture of the detector is shown in figure 1.2. It has a layered structure that consists of the Inner Detector, which is closest to the Interaction Point, the electromagnetic calorimeter, the hadronic calorimeter and the Muon Spectrometer on the outside of the detector. The shape of the systems comprises two main structural parts. A cylindrical section, the so-called barrel, that covers the area around the Interaction Point, and particle tracks perpendicular to the beam direction is supplemented by two circular sections, the endcaps. Their purpose is to detect and track particles that have a large momentum along the beam direction after collision and keep close to the beam axis. The
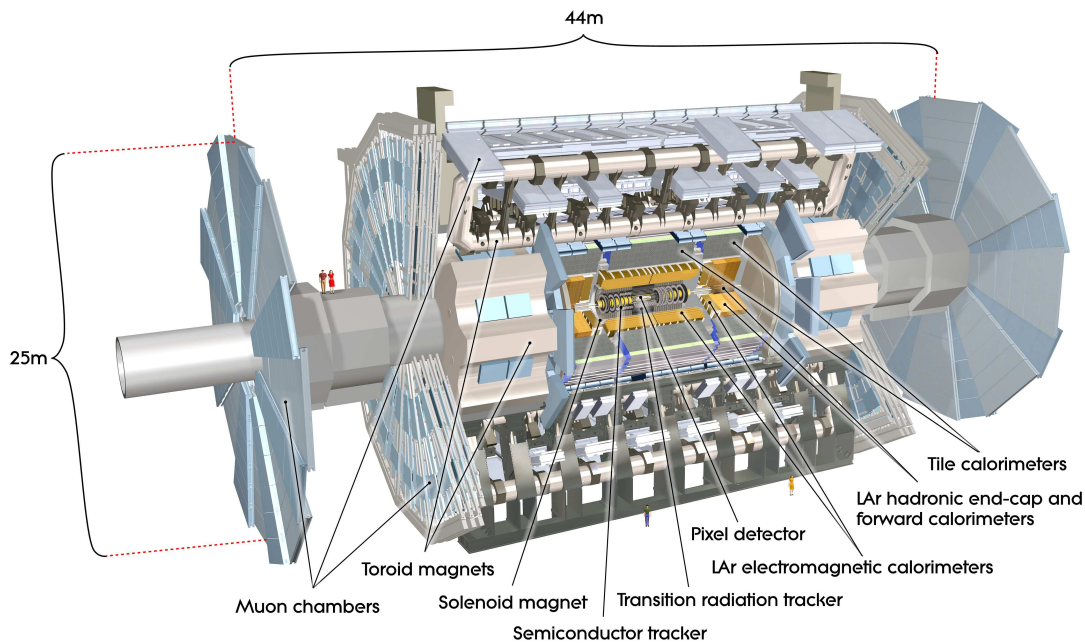
Figure 1.2.: The ATLAS detector consists of different components: Innermost, near the Interaction Point is the Inner Detector, a precise tracking system. Electromagnetic and hadronic calorimeters measure the energy of the particles while the muon system on the outside gives a good measurement of the muon momentum and muon tracking. Figure from [8].

different detector parts have different purposes and use a variety of techniques for particle tracking, identification and momentum measurement. Figure 1.3 illustrates the behavior of charged and neutral particles created during collisions at the Interaction Point of ATLAS in the different sections of the detector. The inner part of the detector is built up from three different precise tracking systems that also contribute to the momentum measurement of charged particles in the other detector parts. Those are the Pixel, the Semiconductor and the Transition Radiation Tracker (TRT). Surrounding the innermost section is a solenoid magnet, which bends tracks of charged particles and therefore allows momentum measurements in the transverse plane of the detector. Particles leaving the Inner Detector reach the calorimetry section of the ATLAS detector. It consists of the electromagnetic calorimeter at the inner side and the hadronic calorimeter at the outer side of the calorimetry section. Calorimeters are necessary to measure the energy of charged particles and jets, but especially of neutral particles (for example γ or n) that cannot be seen in the inner tracking section. While electrons and photons are stopped in the electromagnetic section, the hadronic section is needed for determining the energy of hadrons and hadronic jets. The calorimeters make a large contribution to the particle identification of photons or electrons. Most muons are passing the calorimeters without being stopped, since they are minimally ionizing

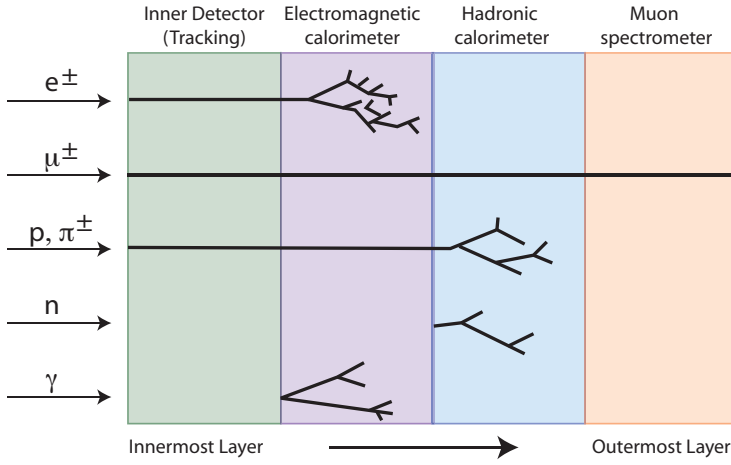Figure 1.3.: Different particles (charged, neutral, hadronic and leptonic) interact in different ways with the detection materials of the layered detector structure. Each layer is specialized on a certain type of particle and force. Neutrinos as they are only interacting via the weak force, leave the detector unseen, but can be reconstructed via energy and momentum conservation of the other collision remnants. Figure drawn after [10].

particles. For their identification as well as for their momentum and charge measurement, a Muon Spectrometer has been placed at the outermost part of the ATLAS detector. Due to the stringent requirements for the muon momentum resolution, it needs to be voluminous. A large toroidal magnet field bends muon tracks and therefore allows for an independent measurement of muon momentum additionally to the measurement in the Inner Detector.

Inner Detector (ID)

The Inner Detector is located inside a solenoid magnet of up to $2\,\mathrm{T}$ field strength. This detector part uses three different technologies to get a good tracking information on charged particles and being able to reconstruct very short-lived particles. Also the search for secondary vertices and the determination of the exact Interaction Point of the colliding particles are relying on this detector section. The innermost layer of the Inner Detector consists of silicon pixel detectors with a large number of channels (1.4×10^8). They provide a very good spatial resolution perpendicular to the beam axis ($12\,\mu\mathrm{m}$) as well as in beam direction ($60\,\mu\mathrm{m}$). The silicon micro-strip detector (SCT) in the barrel is arranged in concentric cylinders around the beam axis and the pixel detector. Its purpose is the precision measurement of 3-dimensional tracks. The silicon micro-strips cover a larger area than the pixels, while still obtaining a good resolution ($17\,\mu\mathrm{m}$ in r-phi direction, $580\,\mu\mathrm{m}$ in direction of the beam axis).

The Transition Radiation Tracker (TRT) covers the outermost regions of the Inner Detector part. Transition radiation photons are created, when charged particles cross layered stacks of pp/pe-foil. They are converted into electrons in the xenon based operating gas of straw tubes. This charge is further amplified by conventional gas amplification in a high electric field gradient. The TRT contributes to the e^-/π-separation and provides tracking information on the charged particles.
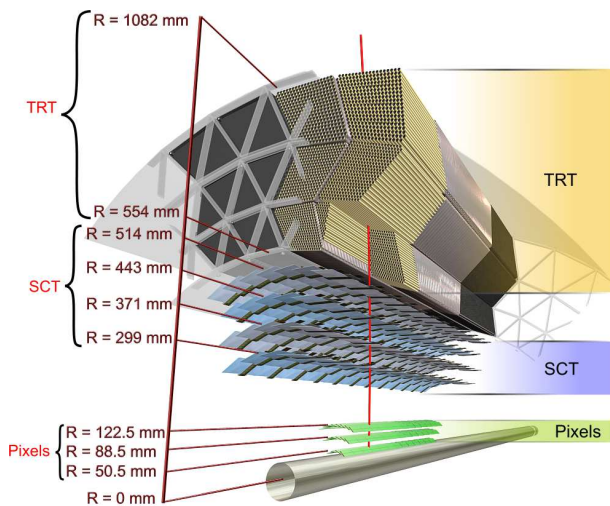
Figure 1.4.: The different detector elements (Pixels, SCT and TRT) as they are located in the Inner Detector around the beam axis ($R = 0$). Figure from [8].

Calorimetry

The calorimeter section of the ATLAS detector covers a radius of up to 4.23 m and measures the energy and position of charged and neutral particles, such as electrons, gammas, hadrons, taus and jets with the highest possible energy resolution while providing a good jet containment. This is needed to provide useful information on the particle identification and the reconstruction of the muon-momentum. ATLAS uses sampling-calorimeters, where absorber and detection material are alternating. The total shower energy must be estimated because of the losses in the dense absorber material, but it also causes a shower that evolves quickly, which saves detection material and space.

The calorimeter part is divided into two layers. The inner section is the electromagnetic calorimeter (ECAL) that measures the energy of electromagnetic showers and is a liquid-argon sampling calorimeter in accordeon layout with lead absorber plates and liquid argon in between them. Finely segmented electrodes collect the primary charge that was deposited by a passing particle in the argon. The granularity of the ECAL must be very high near the Inner Detector part, but a coarser granularity on the outside regions and the end-caps is sufficient for jet re-constructions and missing energy measurements. The energy and position resolution both at the same time are good for the ECAL.

The hadronic calorimeter (HCAL) is specialized for the exact determination of the energy of hadronic showers and nuclear fragments. In the barrel region it consists of iron absorbers interspaced with plastic scintillators, while in the end-cap region the hadronic calorimeter is again liquid argon based. The energy resolution is about $10\%/\sqrt{E} \oplus 0.5\%$ (E in GeV) for the ECAL and $50\%/\sqrt{E} \oplus 3\%$ (E in GeV) for the hadronic calorimeter with a segmentation of $\Delta\eta \times \Delta\phi = 0.1 \times 0.1$ [1]. The calorimeters must have a certain thickness in order to stop most jets and provide a low probability for leaks into the muon section.

---

[1] ATLAS has a cartesian coordinate system (X, Y, Z) and cylindrical coordinates (r, ϕ, θ). The origin of both systems is the Interaction Point. The Z-axis is parallel to the beam axis, the X-axis points to the center of the
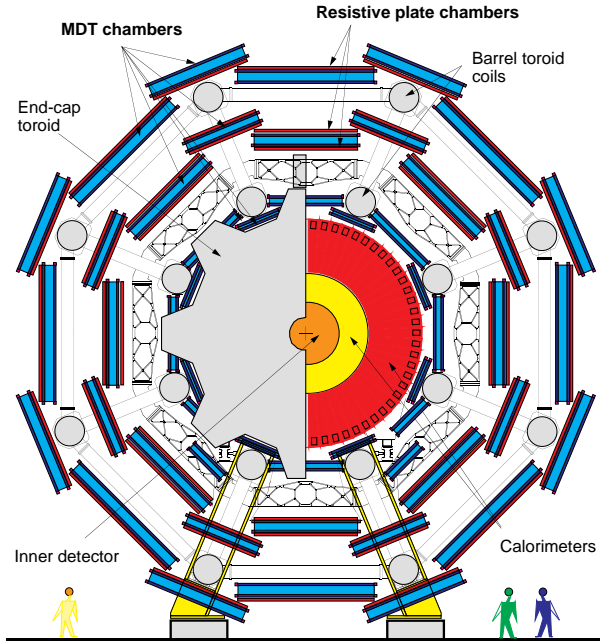
Figure 1.5.: The Barrel cross section of the AT-LAS Muon Spectrometer section. The muon chambers are arranged in concentric circles around the beams axis to cover a large volume and are positioned between and around the eight superconducting coils of the toroid magnets. Figure from [9].

Magnet System

ATLAS comprises a large magnet system with the purpose of bending particle tracks in the tracking regions of the detector. Bent particle tracks are needed in order to be able to determine the particle momentum from the curvature. The central solenoid is located between the Inner Detector and the calorimetry section and creates a magnetic field in the ID of up to 2 T. It is needed for the momentum reconstruction of low-energetic and very short-lived particles in the tracking section. The superconducting coil operates at a temperature of 4.5 K and uses the surrounding detector structures of the calorimetry section as a flux return. The outmost part of ATLAS is equipped with three big toroid magnets, consisting of 8 coils each. Their field lines are surrounding the detector axis azimuthally. The superconducting toroids have air cores and cover a large volume while reaching a magnetic peak field strength of 3.9 T at the barrel region and 4.1 T at the end-caps.

1.2.2. ATLAS Muon Spectrometer

The Muon Spectrometer is the biggest subdetector of ATLAS in terms of covered volume. Various techniques are used in the different sections to provide the best possible focus on the detection and tracking of muons. An overview about the different types of detectors and their location in the ATLAS muon system can be found in figure 1.6.

Monitored Drift Tubes (MDT) are used in the barrel region and also in the end-cap except

---

LHC ring, and the Y-axis is perpendicular to X and Z, pointing upwards. Then $\phi = \arctan\left(\frac{\sqrt{X^2+Y^2}}{Z}\right)$ and $\theta = \arctan\left(\frac{y}{x}\right)$ with pseudo rapidity $\eta = -\ln\tan\left(\frac{\theta}{2}\right)$.
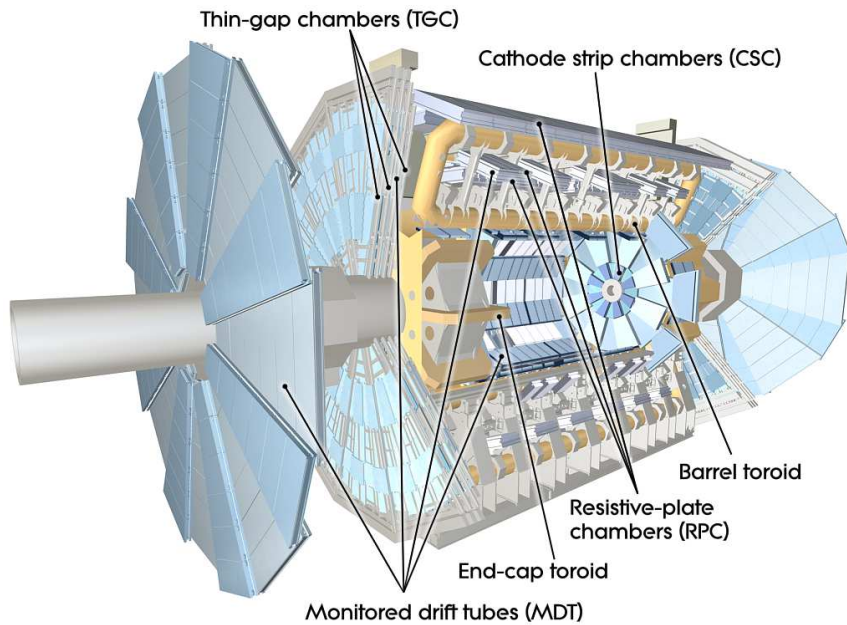
Figure 1.6.: The ATLAS Muon System as a cross section of the barrel region with the two different types of chambers: Tracking chambers (MDT and CSC) and the trigger chambers (RPC and TGC). Figure from [8].

the innermost region to precisely track muons. The tracks in the muon chambers are curved by the toroidal magnetic field. This provides the possibility to measure the muon momentum precisely. They are combined with Resistive Plate Chambers (RPC) and Thin Gap Chambers (TGC) that are used for triggering purposes. The trigger chambers give a digital signal when a particle crosses their detector volume. With their fast readout they are used to decide whether an event is interesting and should be stored or discarded.

The chambers in the barrel are layered in three concentric circles around the beam axis. The three layers have a distance from 5 m up to 10.5 m to the beam axis. Chambers in the barrel section have a rectangular shape and their maximum length is about 6.3 m. See also 1.6 for a cut-view of the barrel Muon Spectrometer.

In the inner layer of the end-cap region Cathode Strip Chambers (CSC) are used instead of MDTs because of their better capability in handling the high particle flux near the beam axis. Chambers in the end-cap region have a trapezoidal shape and form two large disks. While the disks themselves are oriented perpendicular to the beam line, the CSC chambers are inclined about 15 degrees to be perpendicular to most of the incoming particles from the Interaction Point. A short description of the different chamber types follows, for more information on the Muon Spectrometer see also [9].

Figure 1.7.: Drawing of a barrel MDT chamber with a rectangular shape. Two multilayers of drift tubes form the chamber. The shape of the chamber is surveilled by an in-plane monitoring system in combination with temperature sensors. Figure [9].

MDT and CSC: Precision Tracking

MDT chambers are built up from layers of drift tubes. These have a cylindrical shape with an inner diameter of $3\,cm$, filled with gas ($ArCO_2$) and are operated at $3\,bar$ absolute pressure. Inside is a thin ($50\,\mu m$) metal wire that has a high positive potent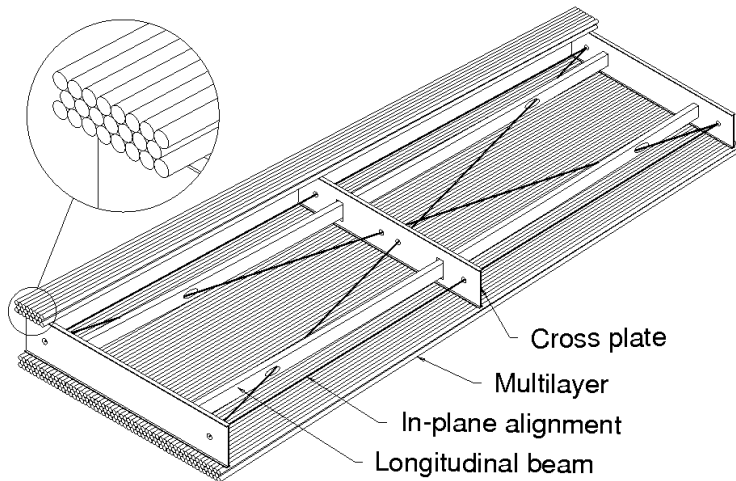ial against the surrounding neutral tube walls. The resulting radial drift field causes any negative charge inside the tube to drift to the wire and the positive charge to drift away from it. Charges are created in the gas-filled volume, when a charged particle like a muon traverses the drift volume and creates on its track primary ionization. When the electrons reach the region around the wire, gas amplification occurs and the initial charge is multiplied by a factor around 20000 in an avalanche process. By measuring the time it takes the charge to drift towards the wire, it is possible to get timing information on the track of the charged particle inside the tube. About 380,000 MDTs exist in the muon system, arranged in 1194 chambers. The Muon Spectrometer was designed to provide a transverse momentum resolution of $\frac{\Delta p_t}{p} < 10^{-4}\,\frac{p}{GeV}$ for $p > 300\,GeV$, which requires a resolution of $\lesssim 80\,\mu m$ in each of the wire tubes. The relative position of the wires and tubes with respect to each other must also be known very precisely (about $35\,\mu m$). This knowledge is provided by the so-called 'in-plane-alignment' that continuously monitors and records information about the shape of the chamber. A CCD-camera is watching a chessboard-pattern over a distance. The slightest structure movements are registered by this core feature of the MDTs that adds the monitoring aspect to the drift tubes.

CSC chambers are used as high-precision tracking chambers, like the MDT in the innermost layer of the end-cap ($|\eta| > 2.0$) because of their higher rate-capability while still providing high time and track resolution. They can withstand the rate and background conditions that would exceed the limits for safe operation of the MDTs. Therefore CSCs are replacing the MDTs in this region. CSC are multiwire proportional chambers (MWPC). They have cathode planes that are segmented into strips in orthogonal directions and wires oriented in radial direction. With this setup it is possible to measure both coordinates of the induced charge distribution of the crossing

charged particle. CSCs are arranged in the end-cap region in two disks with each 16 chambers. Four planes allow four independent measurements in ϕ and η along a muon track with a resolution of about 40 - 60 μm in the bending plane.

RPC and TGC: Trigger Decisions

For the triggering of the detector, chambers with a very fast response (few ns) are needed. Drift times must be short for this purpose and an excellent time resolution provides high probability for a correct Bunch-Crossing Identification (BCID) of the current event. Trigger chambers are split into two different systems. Resistive Plate Chambers (RPC) cover the barrel region in three concentric circles around the beam, while Thin-Gap Chambers (TGC) are used in the end-cap region of the muon detector. TGCs are MWPC with extremely thin spacing between anodes and cathode. The short drift distances and the special electrical field configuration provide good time resolution (1.5 - 4 ns) and a very fast response. All TGC wires are positioned parallel to the MDT wires. A 2-dimensional readout of the tracks is possible, because not only the signal from the wires is used for position determination, but also the signals from strips attached to the cathode that are oriented othogonally to the wires.

RPCs are made of pairs of parallel bakelite plates, filled with a gas mixture based on tetrafluoroethane ($C_2H_2F_4$). The distance between the plates is small and the plate material as well as the working gas have a high resistivity. High voltage of several kilovolts is applied to the two plates. Any primary ionization induced by a crossing particle drifts towards the plates and is multiplied by gas amplification. The readout is realized via capacitively coupled metal strips on the bakelite surface. The strips in the top layer are oriented perpendicular to the strips in the layer on the bottom surface and therefore 2-dimensional track information of the particles is provided. The time resolution of the RPCs is about 1.5 ns.

Alignment System

The high resolution of the muon system can only be obtained if not only the distances inside a chamber and between the wires of the MDT are known with high precision, but also the distances and relative orientation between the chambers themselves are continuously measured. The muon system is large, with diameters up to 22 m. Movements of the chambers with respect to each other of several mm can happen when the toroid magnets are switched on or off and also temperature changes can cause major distortions of the whole muon system. The so-called 'global alignment system' monitors the positions of the total Muon Spectrometer geometry and all chambers and stations in it. It consists of optical sensors controlling the positions of the chambers and proximity sensors. In some regions reference bars between the chambers are used, whose own distortion is monitored by an optical system.

1.2.3. Trigger and Data Acqusition

Because of the high bunch crossing rate of the LHC (40 MHz), corresponding to a proton-proton interaction rate of about 10^9 Hz at design luminosity, the data volume created by all events in the
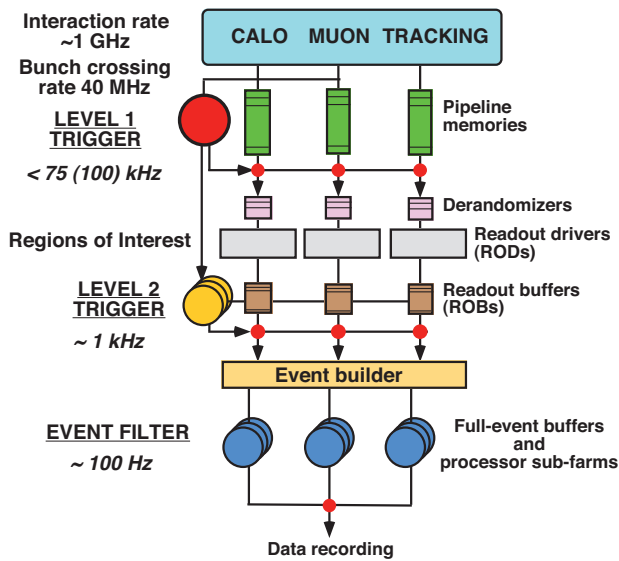
Figure 1.8.: The ATLAS trigger system is split into three levels and provides preselection for the high event rate. It reduces the data rate from initially about $1\,\mathrm{GHz}$ to approximately $300\,\mathrm{Hz}$. Figure from [11].

different detector parts is too high to be stored without severe preselection. The total number of stored events must be reduced to a data volume that is compatible with the technological and resource limits. The necessary high rejection rate of about 5×10^6 is reasonable, because most events are not of any interest from particle physics point of view. A final data rate of about 300-500 Hz is desired and can safely be stored. ATLAS uses a 3-level trigger system for this data rate reduction. It is shown as a sketch in figure 1.8. Each trigger level adds more and stricter decision criteria and reduces the event rate that is passed on to the next trigger level. These criteria have to be chosen wisely, because the data rate needs to be reduced drastically. At the same time signatures for possible new physics phenomena must have a chance to pass the trigger, even without knowing these signatures precisely in advance. The Level-1 trigger is hardware-based and gets input for its decision from the trigger chambers of the Muon Spectrometer and the calorimeters. Because the decision finding process takes about $2.5\,\mu\mathrm{s}$, which is longer than the time between two collisions $(2.5\,\mathrm{ns})$, the data needs to be stored in the mean-time in long data buffers before passing the selected events to the next trigger stage. The following High-Level-Trigger is built up from the level-2 trigger that is only partially hardware-based and the purely software-based Event Builder and the level-3 trigger (Event Filter). The High-Level-Trigger output rate is about $300\,\mathrm{Hz}$ and the triggers are adjusted regularly during data taking to keep it at a constant level, despite changing detector and accelerator conditions like the actual luminosity and the detector status. For more information about the Trigger System of ATLAS see [11].

1.2.4. High Luminosity LHC Upgrade

This section will give a short summary of the planned LHC and ATLAS New Small Wheel activities during the upgrade phases in the next years. Details are given in the New Small Wheel Technical Design Report [12].
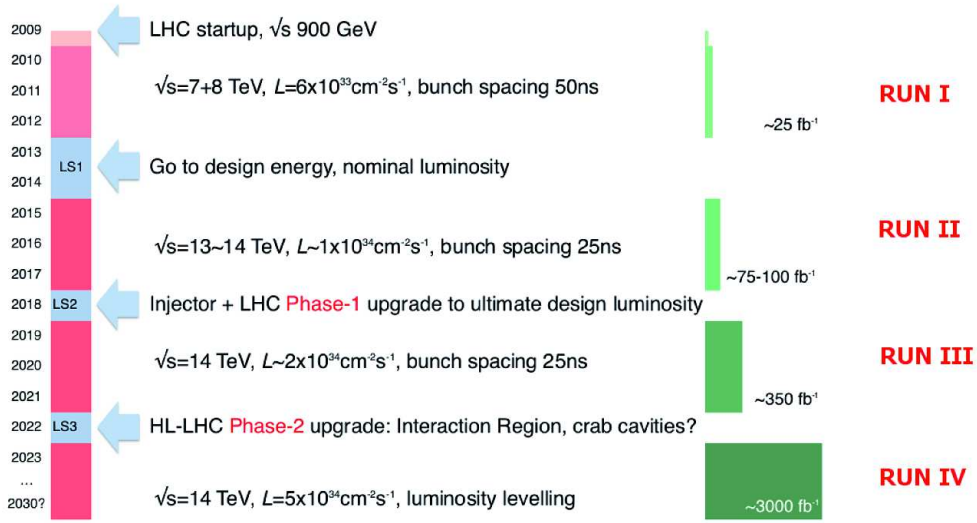
Figure 1.9.: Estimated timeline for the high luminosity LHC and ATLAS upgrade activities. [12]

After a very successful first period of data taking (RUN I) with about $25\,\mathrm{fb}^{-1}$ collected data at 7-8 TeV center-of-mass energy, the LHC accelerator machine will be upgraded and improved. This will be carried out in several phases and will increase the center-of mass energy to the design energy of $\sqrt{s} = 14\,\mathrm{TeV}$ and the luminosity up to $5 \times 10^{34}\,\mathrm{cm}^{-2}\,\mathrm{s}^{-1}$. The time schedule for the LHC-upgrade is shown in figure 1.9. The LHC upgrade will allow the experiments to collect data at the highest possible rates and extend the reach of the physics program significantly by providing the necessary data to measure the mass and the properties for the new found boson. It will be possible to determine, if it is the Minimal Standard Model (MSM) Higgs particle and if there are more new particles in the energy range up to 14 TeV. The successive implementation of technical improvements will take place in the period between 2013 and 2018. Major replacements of several accelerator parts in the LHC proton-injection chain will be necessary and also the two big general-purpose experiments ATLAS and CMS need to undergo modifications and enhancements.

The LHC accelerator will be upgraded in 2 phases: in 2014-2015 the LHC will be operational again after the current shutdown and the next physics run will take place. The physics run is planned to have a pp-energy of about 13-14 TeV with a expected luminosity of $1 \times 10^{34}\,\mathrm{cm}^{-2}\,\mathrm{s}^{-1}$. The expected integrated luminosity for this phase is around 75 to $100\,\mathrm{fb}^{-1}$. Phase-1 upgrade will be primarily the upgrade to ultimate design luminosity $2 \times 10^{34}\,\mathrm{cm}^{-2}\,\mathrm{s}^{-1}$ with 25 ns bunch spacing. About $350\,\mathrm{fb}^{-1}$ data shall be collected from 2018 onwards in this phase. After a longer period of run time in 2022 the phase-2 upgrade is planned, in order to reach an even higher luminosity. From the physics point of view, after running with phase-2 configuration and collecting data of about $350\,\mathrm{fb}^{-1}$, the Higgs spin-parity should be known with about 5σ and the ratios of the couplings to about 30 % to 50 %. Fine details of the Higgs-potential take more time and make more data
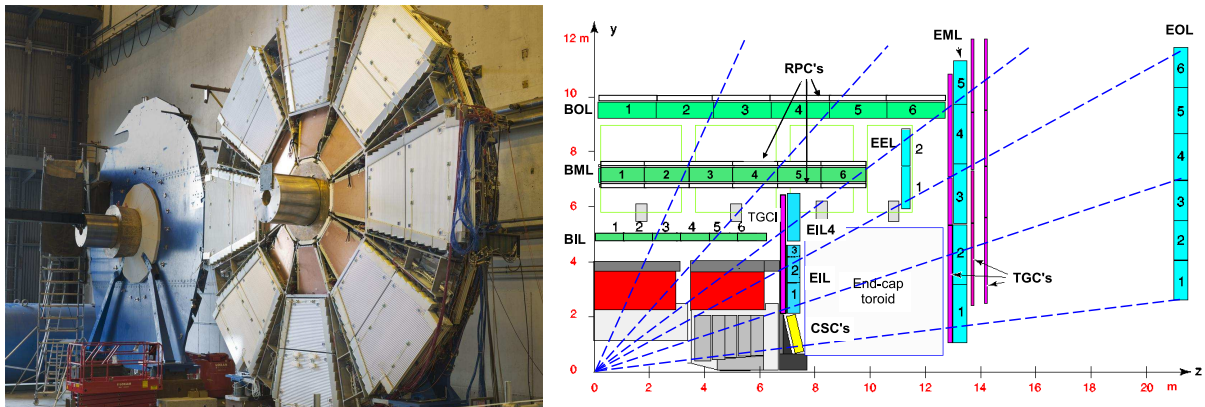
Figure 1.10.: Left: The present muon small wheel during assembly. On the outside are the MDT chambers, but in the inner area, CSC chambers provide better resistance against the high background near the beam axis. The picture is taken from [7]. Right: Cut-view of the end-cap muon system. The small wheel consists of the CSC (yellow) and the MDT parts above that are directly connected to the CSC. Figure from [8].

collection necessary. Multi-Higgs-couplings could maybe be measured after $3000\,\mathrm{fb}^{-1}$ in LHC phase-2 upgrade configuration. The physics goal for the luminosity-upgrade of the LHC can only be to investigate and to explore new and previously unreachable energy regions and phase space for new physics phenomena. A big step in this direction might already be the upgrade during the current shutdown in 2013/2014 from $8\,\mathrm{TeV}$ to 13-14 TeV, where we might already cross a threshold for possible new physics phenomena and unknown particles. For more detailed studies and precise measurements of the parameters of the new found particle, that might be the Minimal Standard Model Higgs Boson, a new e^+-e^- collider is essential that can provide a much cleaner environment than the LHC.

ATLAS Upgrade

For the High Luminosity LHC upgrades the ATLAS experiment needs to prepare well during the next years. The higher luminosity that will provide access to the necessary higher statistics for the Higgs measurements will impose new requirements for the detector with respect to increased rate capability and a higher robustness against aging effects as well as coping with the more demanding background environment. Some detector parts will also reach their lifetime span during the earlier phases and need to be exchanged or renewed.

The ATLAS upgrade phases will be timed consistently with the LHC accelerator upgrades. The phase-1 upgrade (2018) will focus on the level-1 trigger system. Level-1 calorimeter and level-1 muon triggers need to be improved to prevent significant loss of acceptance for interesting physics processes. The trigger threshold turn-on will be sharpened and the background discrimination improved while the low transverse-momentum threshold must be kept.
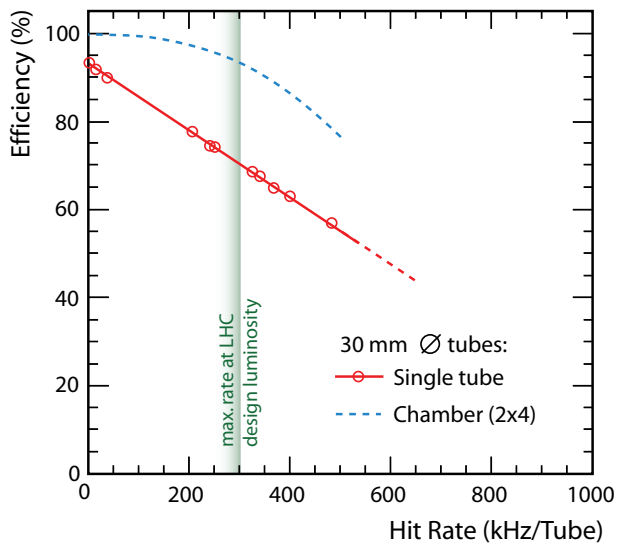
Figure 1.11.: MDT singe tube hit and track segment efficiency as a function of tube rates estimated with test beam data, after [12].

In phase-2 of the ATLAS upgrade a full replacement of the central tracking system as well as major upgrades of the trigger and readout systems are planned.

In this context, focus will be given to the Muon Upgrade and especially to the New Small Wheel, since it is mainly driving the work in this thesis.

Muon System Upgrade: The New Small Wheel

The largest impact of the LHC luminosity upgrade will be noticeable in the muon end-cap system, and especially in the end-cap detector disks that are closest to the Interaction Point, which are called the Small Wheels. The present configuration of the Small Wheel can be seen in figure 1.10. It uses two different technologies for charged particle detection. For tracking purposes MDTs are used in the outer region. Close to the beam line, CSCs are needed due to the higher background that would exceed the MDT safe operation limits. TGCs give trigger signals to the level-1 triggering system. The Muon System needs to be upgraded in order to be able to provide best performance for the high luminosity LHC upgrade. Especially the Small Wheel located nearest to the Interaction Point in forward direction, where the highest radiation rates are expected, needs to be replaced. During Run III the luminosity will already exceed the design luminosity of the LHC. With 55 to 80 interactions per bunch crossing (up to 140 in Run IV) the expected pile-up in the detector is very high.

The hit rates in the detector are caused by the so-called 'cavern background', which is composed mainly of low-energy γ and n generated by other p-p interactions in the same event or even in earlier bunch crossings. The counting rates under the new conditions for Run III and IV are predictable and will exceed the safe limits for the existing MDT system by far with up to about $15\,\mathrm{kHz\,cm^{-2}}$.

The track finding algorithm in the Muon Spectrometer operates the following way: Short track segments are built from single hits in the different stations of the detector. Matching segments

Figure 1.12.: Left (a): η distribution of muon trigger rates with $p_T > 10\,\text{GeV}$ matched to offline well reconstructed muons [12]. Right (b): p_T distributions with $p_T > 20\,\text{GeV}$ with different cuts for rate reduction applied [12].
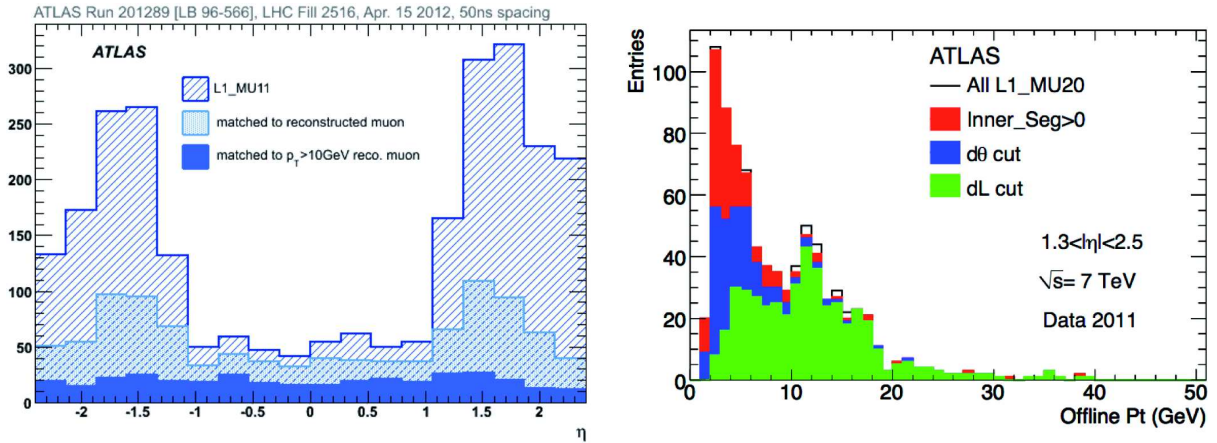
are put together to form a track that can be assigned to a muon in the offline reconstruction. Figure 1.11 shows the efficiencies of single tubes and of the segment finding in a chamber dependent on the hit rates. The single tube hit efficiency decreases quickly and linearly with the hit rate, while the segment finding efficiency stays at an acceptable level up to about 300 Hz, which is the calculated tube hit rate for the LHC design luminosity $1 \times 10^{34}\,\text{cm}^{-2}\,\text{s}^{-1}$. The single tube hit efficiency has already decreased about 35 % at this point, and more will lead unavoidably to a significant degradation of the spectrometer performance. Also the position resolution deteriorates with higher hit rates due to space charge effect in the drift tubes of the MDT system.

Performance studies of collision data showed unexpectedly high trigger rates in the endcaps. The distribution of trigger rates selected by level-1 muon trigger with $p_T > 10\,\text{GeV}$ in dependence of the angular distribution in η can be seen in figure 1.12(a). The end-cap regions ($\eta > 1$) show a significantly higher trigger rate than the barrel region, while the offline reconstructed muons that are matching the triggers, show a far smaller dependence on η. This excess in trigger rate arises from fake triggers in the endcap region due to the high cavern background in forward direction, especially close to the beams axis. Trigger simulations for a center-of-mass energy $\sqrt{s} = 14\,\text{GeV}$ and a luminosity of $3 \times 10^{34}\,\text{cm}^{-2}\,\text{s}^{-1}$ with a transverse momentum selection of $p_T > 20\,\text{GeV}$ leads to level-1 muon trigger rates of about 60 kHz, while the overall level-1 trigger rate may only be 100 kHz.

To reduce the overall level-1 trigger rate, the most appropriate method is to apply hardware cuts in the level-1 trigger decision process that can efficiently separate the fake muon triggers from the events with real muon tracks. By performing an offline analysis of the reconstructed muons it is possible to find suitable conditions for these cuts. Figure 1.12(b) shows the total number of

level-1 muon triggers against the offline values of p_T and the rates with the different cut conditions applied. The requirements for the cuts are the following: there must be a track segment found in the Small Wheel, not only uncorrelated hits (number of track segments in Small Wheel > 0). The corresponding distribution in the histogram in figure 1.12(b) does not show a significant rate reduction yet. The blue distribution is the result of the application of the dθ cut that requires that the Small Wheel segment points to the Interaction Point (IP) with an angle θ (|dθ| less than 10 mrad). Another quite significant fake rate reduction can be achieved by applying a third cut, the dL cut, where the Small Wheel segments need to match a Big Wheel segment in (η - ϕ) with less than 0.1 mrad. The biggest rate reduction effect is visible for all cuts in the region below the trigger threshold $p_T > 20$ GeV, which is the expected energy range of the fake triggers.

Similar cuts need to be applied in the online trigger level-1 decision process on hardware basis. This will provide a fake rate reduction down to a level comparable to the overall rate of the MDT barrel system, which would be around 22 kHz for a luminosity of 3×10^{34} cm^{-2} s^{-1}. For further improvement of the fake rates also the Big Wheel trigger resolution will be increased during the ATLAS phase-II upgrade. Best results are achieved, if the resolution for both systems is the same. Therefore the Small Wheel needs to fulfill already these higher requirements after its replacement during phase-I upgrade.

All this leads to the following requirements for the New Small Wheel detector: its performance should be at least as good at the highest luminosities in the high-energy upgrade, as the MDT performance at design luminosity. Therefore, the transverse momentum p_T of passing muons should be measurable with a precision of 10 % for 1 TeV muons over the full area of the Small Wheel. Also the above mentioned specifications must be met for the track segment reconstruction resolution, segment finding efficiency.

Since the detector cannot be accessed at any time during the runs for replacement work, a multi-plane detector can handle a failure of one plane more safely. A good radiation hardness is also required for the expected 10^{12} hits/cm^2 that will be collected over the total ATLAS lifetime in the hottest detector regions. Overall efficiency and resolution stability at very high particle momenta over 5 years at phase-2 luminosity (about 3000 fb^{-1}) is essential for the new system as well as cost effectiveness, robustness and low needs for cooling.

The ATLAS community chose Micromesh Gaseous Detectors (MicroMeGas, see also chapter 2.2.1) in combination with small-strip Thin Gap Chambers (sTGC) as the new technologies that could be able to fulfill all requirements for the New Small Wheel. Since Micromegas are the main type of detector that will be investigated in this thesis, they will be described in detail in chapter 3.

1.3. Physics at the LHC

In this section a short overview about the current status of the LHC measurements and results will be given. Especially the Higgs discovery in 2012 and the related physics as the driving reason for the LHC high luminosity upgrade will be focused.

(a) Gluon fusion

(b) Higgs production associated with top pair

(c) Vector boson fusion

(d) Higgs-Strahlung
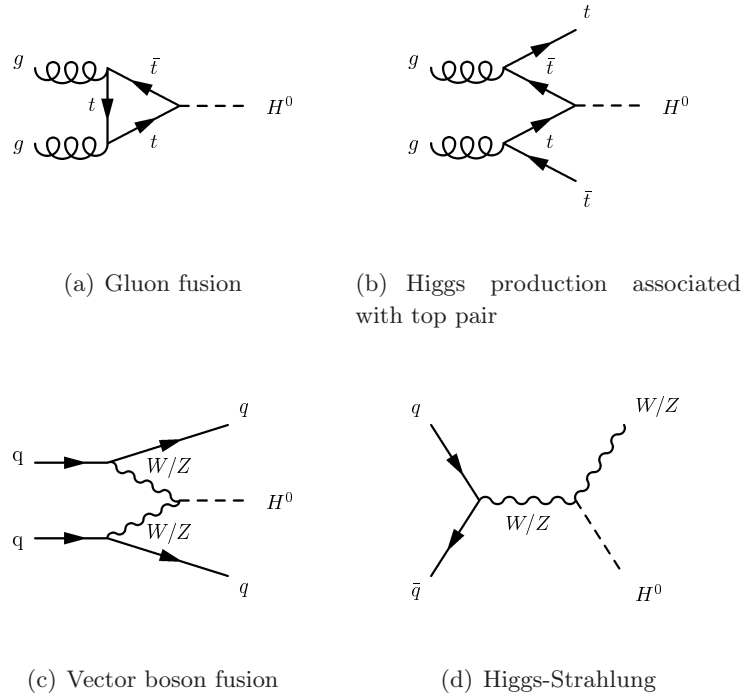
Figure 1.13.: The four main Standard Model Higgs production channels, lowest-order Feynman diagrams.

The LHC performance in the first two runs in 2011 and 2012 exceeded all expectations. It was possible to run the LHC with higher luminosity than previously planned. This was done with 50 ns proton bunch spacing, which resulted in a larger pile-up. The detectors were able to deal with the higher number of interactions per beam crossing that even exceeded the nominal value for the design luminosity at peak times. The analysis was, on the other hand, more challenging, since due to the pile-up the background understanding needed to be improved. But the higher integrated luminosity gave the chance to collect enough data for the Higgs search.

The results in this last physics run were matching all expectations. Precision measurements and test of the Standard Model QCD processes were done quite successfully. The most important background constituents for the Higgs searches and other new physics searches like WW, WZ, ZZ, $W\gamma$, $Z\gamma$, $\gamma\gamma$, and $t\bar{t}$ were measured in detail and improved the understanding of the background and the detector.

While SUSY searches and general searches for physics beyond the Standard Model showed no indication of any new particles, a Higgs-like boson was found at 125 GeV in July 2012. But there are still open questions regarding this Higgs-like boson: is it the only one or are there more? What is its spin-parity? And if it is the only one, is it the expected and long predicted Standard

(a) $H \to b\bar{b}$, 57.7 % br.r.

(b) $H \to WW \to ll\nu\nu$, 21.5 % br.r.

(c) $H \to \tau\bar{\tau}$, 6.3 % br.r.

(d) $H \to ZZ \to 4l$, 2.6 % br.r.

(e) $H \to \gamma\gamma$ ($\tau\tau$), 0.23 % br.r. together with 1.14(f)

(f) $H \to \gamma\gamma$ (WW and ZZ pairs)
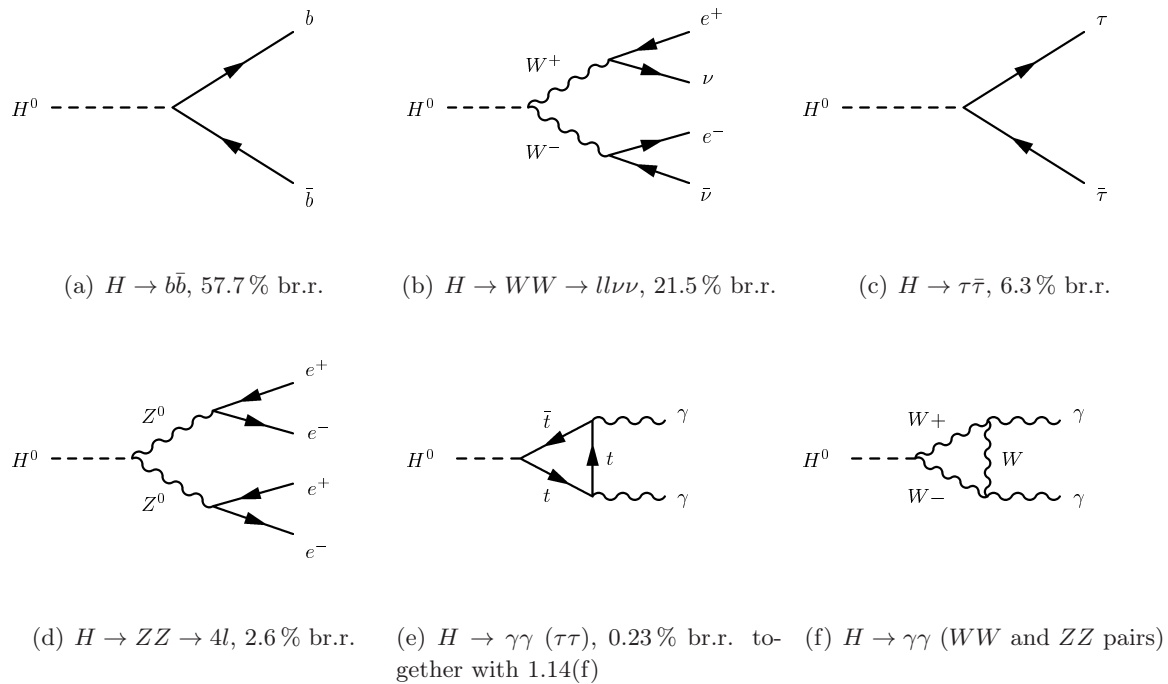
Figure 1.14.: The main Higgs decay channels as Feynman diagrams for a Higgs mass of about 125 GeV.

Model Higgs boson that the whole physics world was looking after?

Higgs Physics

To gain more knowledge about the newly found particle, further measurements are needed to determine its properties. They can be compared to those expected from the Minimal Standard Model (MSM) Higgs. The dominant Higgs boson production processes in the Standard Model in pp collisions are the following: gluon Fusion is a process with a large cross section, the most important process for Higgs production. The Feynman diagram is shown in figure 1.13(a). Vector boson fusion, as shown in figure 1.13(c) and associated production with a pair of W or Z bosons (figure 1.13(d)) have smaller cross sections. There is also the process of associated production with a top quark shown in figure 1.13(b).

For the decay of the Higgs bosons, it is important that the background is well understood and that it can sufficiently be distinguished from the signal. The decay modes with the highest relative branching ratios at a Higgs mass around 125 GeV are shown in figure 1.14. A value of 125 GeV for the Higgs mass is one of the best possible scenarios to study the Higgs, since a large number of channels is available with a comparatively high branching fraction. The branching ratios as a function of the higgs mass are shown in figure 1.16(a). To judge whether a channel is a suitable

Figure 1.15.: Higgs mass plots for the channels $H \rightarrow \gamma\gamma$ (left) and $H \rightarrow ZZ \rightarrow 4l$ (right) with the Higgs particle resonances at $126.8 \pm 0.2\,(stat) \pm 0.7\,(syst)\,\text{GeV}$ for the $\gamma\gamma$ channel and $124.3^{+0.6}_{-0.5}\,(stat)^{+0.5}_{-0.3}(syst)\,\text{GeV}$ for the 4-lepton channel. Plots from [4].

Higgs discovery channel, not only the branching ratio has to be evaluated, but also the 'purity' of the corresponding final state of the channel (which depends on the signal-to-background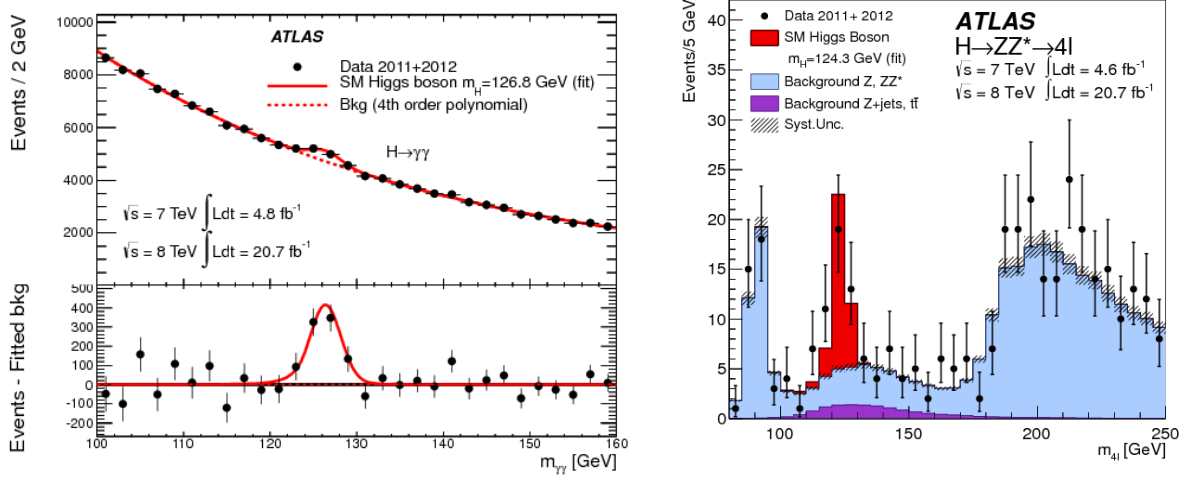-ratio of the final state) needs to be high enough to perform an analysis with sufficient statistics. For example, the channel $b\bar{b}$ has a high branching ratio, but is disfavored because of its very challenging signature in the final state.

Two of the best channels to measure the Higgs mass are the $\gamma\gamma$ and the 4-lepton final state. The Higgs signal plots versus the Higgs mass are shown in figure 1.15. The fits correspond to a Higgs mass peak position of $124.3^{+0.6}_{-0.5}\,(stat)^{+0.5}_{-0.3}(syst)\,\text{GeV}$ [4] for the 4-lepton channel and $126.8 \pm 0.2\,(stat) \pm 0.7\,(syst)\,\text{GeV}$ [4] for the $\gamma\gamma$ channel. This results in a combined Higgs mass $M_H = 125.5 \pm 0.2\,(stat)^{+0.5}_{-0.6}(syst)\,\text{GeV}$ [4]. All branching ratios and couplings can be calculated, if we make the assumption that the new-found particle is exactly the one that is described in the MSM. The relative abundance of the signal in the observed channels is a measure of the probability that this assumption is correct. It is usually measured as the observed rate divided by the expected rate of events and is called signal strength $< \mu >$. ATLAS has measured this variable and it is shown for all available decay channels in figure 1.16. ATLAS observes more events than expected in most of the analyzed channels, as the combined value for the signal strength $1.33 \pm 0.14\,(stat) \pm 0.15\,(syst)$ [4] reflects. The probability that this signal strength is in agreement with the Standard Model expectations is about 7 % [4], which will improve with more statistics. A second possibility to crosscheck whether the new found boson is the MSM Higgs is to compare the relative strength of fermion and boson couplings, but more data is needed to verify this measurement. The spin-parity of the MSM Higgs is expected to be $J^P = 0^+$. This can

(a) Higgs Branching Ratio

(b) Signal Strength

Figure 1.16.: Left plot shows the Higgs branching ratios of the different decay channels in the possible mass ranges from 80 to 200 MeV. Around the value of $M_H = 125$ MeV, most of the channels are near their branching ratio maximum. The right plot shows the signal strengths for the channels measured by ATLAS and the combined signal strength that is in agreement with the expected value for the signal strength, 1. Left plot from [13], right plot from [4].

be investigated by analyzing the angular distribution of the Higgs decay in three possible final states: $\gamma\gamma$, ZZ^* and WW^*. ATLAS can exclude some of the spins with several sigma significance so far, but also for these analysis, more data is needed to push those exclusion limits below the 5σ limit.

2. Gaseous Detectors

This chapter presents and summarizes useful basic knowledge about gaseous detectors and the processes that happen inside this type of detector. Most of the terminology and the presentation follow the work of F. Sauli *Principles of Operation of Multiwire Proportional & Drift Chambers* [14]. More detailed explanations of the covered topics can be found there.

Gaseous detectors are detectors for charged particles that are used in a large variety of applications like for example radiation protection, medical imaging and also homeland security. They are also an absolutely essential component of every high energy physics experiment due to their numerous advantages. Their radiation hardness is very good, because the detection medium (gas) can easily be replaced continuously. In addition, their production costs are relatively low compared to solid state detectors based on silicon. If used with a drift space as in a Time Projection Chamber (TPC) they can provide timing information on the signals and therefore give information on the 3-dimensional track of the charged particle. The radiation length of the materials used is comparatively small, so this type of detector is preferred for layered detector structures.

2.1. Principle of Operation

The basic processes occurring in a gaseous detector will be described in the example of the simplest and most commonly used gaseous detector, the wire tube. Operation modes of the wire tubes will be explained and the multiwire proportional chamber as a related type of detector that is used as part of the setup of the MPGD test chamber is introduced.

2.1.1. Setup of Wire Tubes

Wire tubes have been one of the first types of detectors for charged particles. Their working principle is simple and they have a high detection efficiency. Particles that traverse a gas-filled detection volume cause primary ionization of the gas atoms. The resulting charges are further separated by a drift field pulling the positive ions to the cathode and the negative electrons to the anode, where the signals are registered.

Since the resulting signals are very small, it is useful to further amplify the number of electrons arriving on the anode by gas amplification in a high electric field. To achieve a symmetrical, but inhomogeneous field for the gas amplification, often the anode is realized as a wire, which leads to a radial symmetric field with the cylindrical cathode around it. The electric field in this simplest
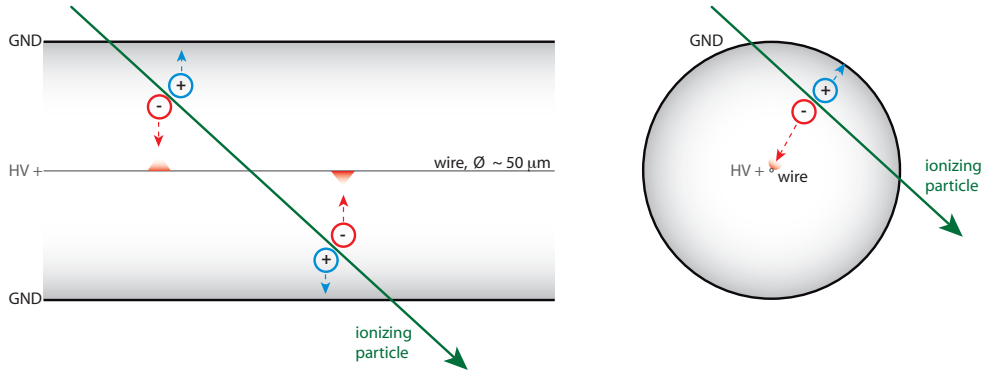
Figure 2.1.: The construction of a classical wire tube. Left: Cut-view lengthwise though the tube with charge amplification of induced charge, right: cut-view perpendicular to the wire direction.

form of a wire chamber at distance r from the center wire is of the form

$$E(r) = \frac{V}{\ln(\frac{r_t}{r_w})} \frac{1}{r},$$

(2.1)

with r_t being the tube (cathode) radius, r_w the wire (anode) radius and V the applied potential between them. In figure 2.1 a picture of a classical wire chamber is shown. The diameter of the cathode tubes is often in the range of several centimeters, while the wires must be thin (some $10\,\mu$m) to create a high electric field in the close proximity for the avalanche process.

Even though the electrons drift towards the anode, the electron signal is not the main component of the signal formation. The ions that were produced in the avalanche process induce a much larger signal while they drift away from the anode. For details see appendix A.1.

The Monitored Drift Tubes (MDT) used for the ATLAS Muon System are of this type of wire tube. They use a $50\,\mu$m thin wire in a tubular cathode with radius $1.5\,$cm. A voltage of $3080\,$V creates the drift and amplification field in the tube that is filled with $ArCO_2$ with $3\,$bar pressure. The gain of the MDTs has been measured to be $G = 2 \cdot 10^4$ [9].

2.1.2. Primary Ionization

Primary ionization is induced by charged particles or indirectly via the interaction of gamma radiation or neutrons with the molecules of a medium. Charged particles loose an average fraction dE of their energy due to Coulomb interactions while traveling a distance dx through a medium, that is given by the Bethe-Bloch equation [3]. This formula holds for the range of the incident particle velocity βc between the velocity of the orbital electrons of the medium, which is about $Z\alpha c$ (α is the fine structure constant) and the region, where radiation effects start to dominate the energy loss:

$$-\frac{dE}{dx} = Kz^2 \frac{Z}{A} \frac{1}{\beta^2} \left\{ \frac{1}{2} \ln \frac{2m_e c^2 \beta^2 \gamma^2 T_{max}}{I^2} - \beta^2 - \frac{\delta}{2} \right\}, \qquad \text{while} \quad K = 4\pi N_A r_e^2 m_e c^2, \qquad (2.2)$$

(a) Bethe Bloch equation [3]

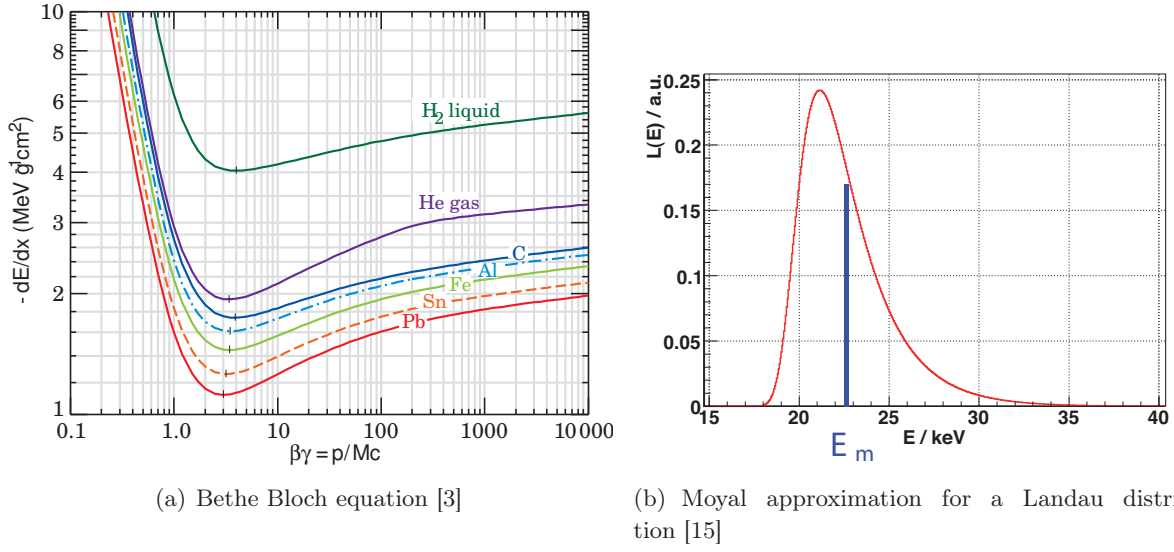(b) Moyal approximation for a Landau distribution [15]

Figure 2.2.: Energy losses of high energy charged particles in materials are described by the Bethe Bloch equation for different materials (left). The right graph shows the probability distribution for a minimum ionizing particle (MIP) in an ATLAS MDT.

with N_A being the Avogadro number, m_e and e the electron mass and charge, Z, A the atomic number and mass of the target material and I its effective ionization potential. T_{max} is the maximum kinetic energy that is possible to transfer to a free electron in a direct two-body collison. The attributes of the charged particle in the formula are z the charge and β the speed of the incoming projectile in units of speed of light, c. δ is a density effect correction. In figure 2.12(a) the form of $\frac{dE}{dx}$ is plotted against the energy of the incoming particle for different target materials (different A, Z and δ). The curves all show a minimum around the velocity βc, where particles are called 'minimally ionizing'.

If the energy loss of a single particle with a specific energy E in a medium of thickness Δx is measured, the lost energy distribution can be described by a Landau distribution. It is defined as a complex Integral, but can be approximated by [16]

$$L(\lambda) = \frac{1}{\sqrt{2\pi}} \exp\left(-0.5\left(\lambda + e^{-\lambda}\right)\right) \qquad \text{with} \quad \lambda = \frac{\Delta E - \Delta E^{mp}}{\xi}. \qquad (2.3)$$

ΔE is the actual energy loss in a slice of medium of thickness x, while ΔE^{mp} is the most likely energy loss calculated with equation 2.2. In figure 2.12(b) the energy loss of a minimally ionizing particle in an ATLAS MDT is shown. The distribution peaks at the most probable value, but the average energy loss E_m is higher. The shift is caused by collisions where the charged particle transfers an exceptionally high fraction of energy to an electron (so called δ-electron) that is knocked out of the gas atom and can create itself a track of ionized molecules and electrons.
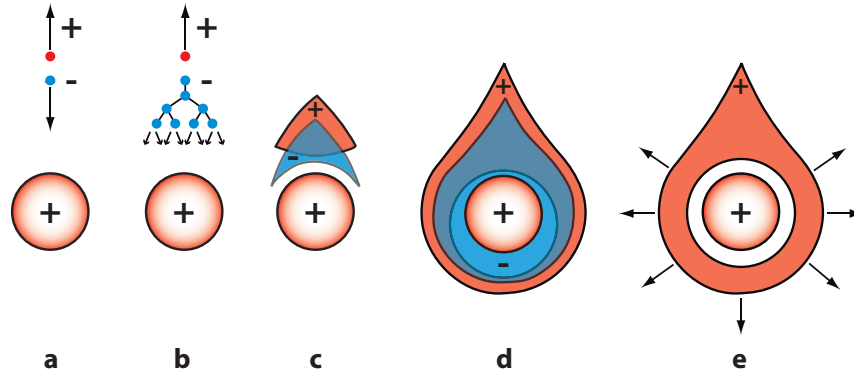
Figure 2.3.: The lateral avalanche development in a wire counter: A single primary electron gets amplified in a drop-like avalanche that quickly surrounds the wire. While the electrons are absorbed nearly instantly, the ions remain much longer in the detector volume, slowly drifting towards the cathode [14].

2.1.3. Gas Amplification

Close to the wire, in the region of the highest electric field, the electrons gain enough kinetic energy between the collisions to create secondary charges. After the collision with a molecule of the surrounding gas, the initial electron continues its travel to the wire anode. This charge amplification process can be described as an avalanche process. Figure 2.3 shows the time-development of an avalanche process in the proximity of a wire anode. Mathematically, this process can be described similarly to a decay process:

$$\mathrm{d}n = n_0 \cdot \alpha \cdot \mathrm{d}x, \tag{2.4}$$

where n_0 is the number of initial electrons at a given position, $\mathrm{d}x$ is the distance that the electron has drifted and $\mathrm{d}n$ the increase of electrons on this short distance. The first Townsend coefficient α is equivalent to the number of ion pairs produced per unit length of drift. This process, and therefore α, is highly dependent on the electric field E, the gas density ρ and the chemical composition of the surrounding gas with its typical ionization and excitation energies.

Integration of equation 2.6 leads to the gain factor G:

$$n = n_0 \cdot \mathrm{e}^{\alpha x} \qquad \text{and} \qquad G = \frac{n}{n_0} = \mathrm{e}^{\alpha x}. \tag{2.5}$$

For non-uniform e-fields, where $\alpha = \alpha(x)$, integration over x is necessary:

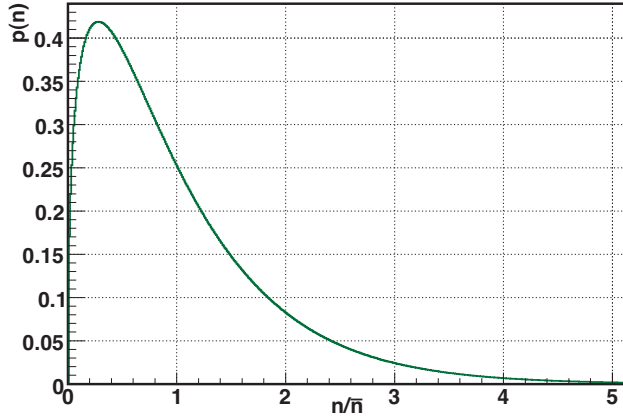$$G = \exp\left(\int_{x_1}^{x_2} \alpha(x)\mathrm{d}x\right). \tag{2.6}$$

Figure 2.4.: Polya Distribution with $\theta = 0.4$ [15]

If $\alpha(E)$ is known for all energies the gain of any possible field geometry can be computed. For a simple radial wire tube geometry and a limited range of the electric field strength (10^2 to 10^3 V/(cm Torr)), one can assume that there is a linear dependence of α on E. This leads to the Diethorn formula [17]:

$$ G = \frac{U}{r_a \cdot \ln(r_c/r_a) \cdot E_{min}(\rho_0) \cdot (\rho/\rho_0)} \exp\left(\frac{U \cdot \ln 2}{\ln(r_c/r_a)\Delta V} \right), \tag{2.7} $$

where the two constants ΔV and E_{min} must be measured in experiment. E_{min} can be interpreted as the threshold energy at a given gas density ρ_0 for the gas amplification process to set in. The anode and cathode radius are called r_a and r_c respectively, and the applied voltage is U.

The Diethorn parameters have been measured for the ATLAS MDT drift tube gas composition (ArCO$_2$ 93 %/7 %) to be $\Delta V = 34$ V and $E_{min} = 24$ kV cm^{-1} (at 1 bar and 25°C ± 10 %)[18]. This gas has also been used for the studies in this thesis.

The gain factor G only gives an average number for the gas gain. The fluctuations around the mean value $\bar{G}$ for multiple measurements of a single electron avalanche process can be described by a Polya distribution:

$$ P(n) \propto (\frac{n}{\bar{n}})^\theta \cdot \exp\left(-(\theta + 1)(\frac{n}{\bar{n}}) \right), \tag{2.8} $$

where n can be identified with G, and $\bar{n}$ with $\bar{G}$. The parameter θ can be chosen and a value of $\theta = 0.4$ [19] describes data reasonably for avalanche processes. As an example such a Polya distribution is shown in figure 2.4.

2.1.4. Operation Modes of a Wire Tube

The processes that take place in the drift volume and the amplification region of a wire tube are strongly dependent on the applied voltage between cathode and anode. Figure 2.5 shows the different modes of operation for a cylindrical wire tube.

If the electric field in the drift volume is too low, the probability of recombination of the primary charges is high and only part of the drifting electrons reach the wire. If the electrons gain enough energy form the electric field to ionize more gas particles on their way, the avalanche starts and the chamber is in *proportional* mode. The signal on the wire is directly proportional to the primary charge and depends on the applied electric field.

For even higher values of the electric field, the *Geiger-Müller* mode is reached and photons get created inside the avalanches. Some of them leave the avalanche region and their energy is high enough to create another electron-ion pair, which can start separate additional amplification processes. Another possibility to create further avalanches are electrons created by photons hitting the outer metal tube. These avalanches spread over the whole wire region and the signal charge is no longer proportional to the primary charge. The amplification process is either stopped by the increasing space charge in the tube or by a quenching gas that absorbs the photons and emits them with a longer wavelength that cannot induce more charges.

In *streamer* tubes, the content of the quenching gas is high enough to limit this effect to a small section of the tube by stopping the lateral propagation of the photons effectively after a few μm. This prevents regions that were not affected by the initial hit from the development of space charge in the drift region after every streamer or breakdown. Space charge reduces the field strength in the avalanche region and as a consequence lowers the gain of the detector or even inhibits any avalanche for the next few hundred ms until the ions are neutralized at the cathode.

Electric fields that are too high cause uncontrollable plasma discharges to happen in the gas volume that can damage and destroy the thin anode wires or in general the anode structures. Photons created in the gas amplification spread the avalanche processes all over the whole gas volume. The high density of the positive space charge in the closest wire region leads to an increase of the electric field seen from greater radii and therefore to uncontrollable break-downs. The limit for safe operation of any gaseous detector is $\alpha x \approx 20$ or $G = 10^8$, which has been found empirically by Heinz Raether [20]. For most detector geometries in proportional mode operation, it is best not to raise the gain over $G = 10^6$ to avoid even rarely occurring discharges, since this is a statistical process that has no threshold energy.

Not only the applied high voltage, but also the gas mixture and the gas pressure have a measurable influence on the gain of any wire chamber. For a non-cylindrical shape of the cathode, also the exact shape of the field in the wire region determines the behavior and the gas amplification of the chamber.

2.1.5. Multiwire Proportional Chambers

Multiwire proportional chambers (MWPC) are mainly used for tracking purposes in high energy physics experiments. A layer of equally spaced anode wires is symmetrically positioned between two cathodes with a high potential difference between the layers, as shown in figure 2.6. Their lateral resolution is limited by the anode wire spacing s that cannot be far less than about $2\,\mathrm{mm}$ for mechanical reasons. The distance h between anode and cathode is about 3 or 4 times larger
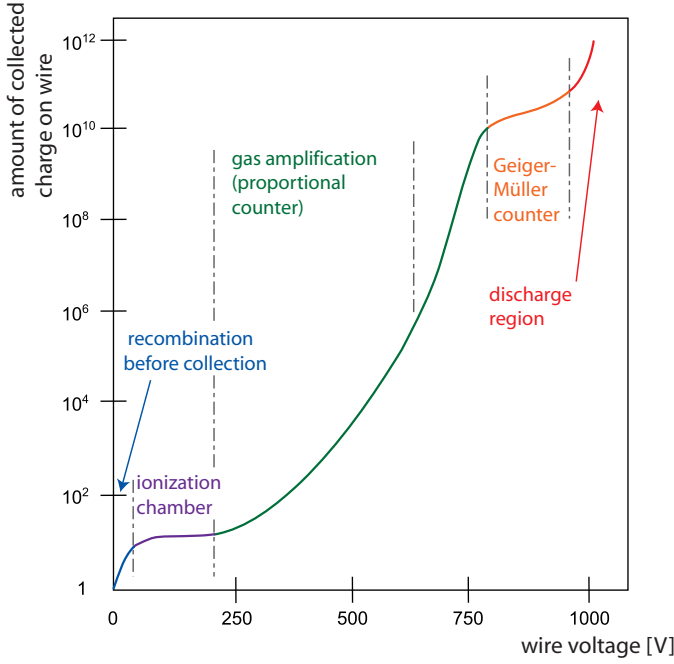
Figure 2.5.: The different operation modes of a wire chamber as a function of the wire voltage (after [14]).

than the wire spacing s to guarantee a symmetric electrical field around the wires that is not influenced too much by the near presence of the cathodes.

Charges induced by primary ionization follow the drift field lines to the wires and get amplified in the high electric field close to the wires. The electric field of such a geometry has been derived in chapter A.1.3 and can be written as:

$$E(x,y) = 2C^*V_a \frac{\pi}{s} \left(\frac{\cosh 2\pi y/s + \cos 2\pi x/s}{\cosh 2\pi y/s - \cos 2\pi x/s} \right)^{\frac{1}{2}}. \tag{2.9}$$

with C^* being the capacitance per unit lengths (total wire length l), defined as

$$C^* = \frac{1}{\ln (r_c/r_a)^2} = \frac{C}{4\pi\varepsilon_0 l} \qquad \text{with} \qquad C = \frac{4\pi\varepsilon_0 l}{\ln (r_c/r_a)^2} \tag{2.10}$$

The approximation for the near and far region electric fields of the wires gives the already known expressions for the single wire chamber and the parallel plate geometry:

$$\text{for} \quad x, y \ll s : \qquad E(x,y) = 2C^*V_a/r \qquad \text{(coaxial field).} \tag{2.11}$$

$$\text{for} \quad \cosh(2\pi y/s) \gg 1 : \qquad E_x = 0, E_y = \pm 2\pi C^*V_a/s \qquad \text{(uniform field).} \tag{2.12}$$

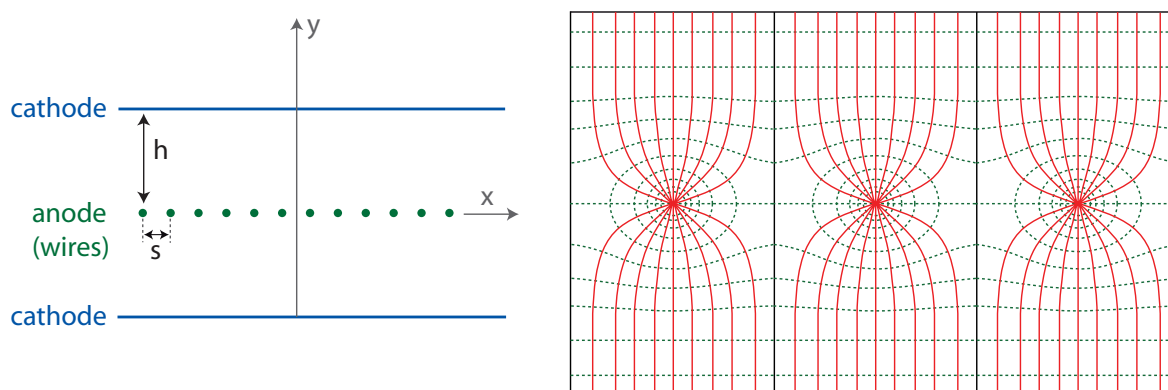Figure 2.6.: Left: Principle of construction of a MWPC: Thin wires are sandwiched between two cathode planes. Right: Field lines (red) and equipotential lines (dashed, green) around the wire region for a MWPC, from [14].

2.2. Micro-Pattern Gaseous Detectors (MPGD)

Conventional wire tubes and multiwire proportional chambers in a large variety of implementations and sizes have been dominating all applications for detection of charged particles, in particular the high energy physics for a long time. However, with the new generation of collider experiments, such as the LHC, the need for even higher rate capability and superior time und position resolution drove the development of a new type of gaseous detector with even finer segmented readout structures.

With the new type of detector, much smaller readout structures are possible and the signal rates can be increased drastically. Apart from the high time and lateral resolution, the new type of detector provides a high flexibility in design and a good mechanical stability. Also a low material budget, good operational stability, radiation hardness and aging properties as well as much lower production costs, compared to silicon pixels for example, can be seen as advantages of this new technology.

This new type of gaseous detector can introduce new ideas and applications to the fields of high energy particle accelerators and experiments in nuclear and astroparticle physics. Also industrial applications such as medical imaging, material science, and security inspection can benefit from the decreasing equipment size and cost savings that this new technology might bring.

2.2.1. Setup and Working Principle of MPGD

The working principle of MPGDs is similar to that of conventional wire tubes. The main difference is that the whole amplification and readout setup is based on very small distances and structures. The electric amplification field is usually formed by a parallel plate geometry of electrodes and the readout plane can even coincide with the anode. Many of these small detector structures
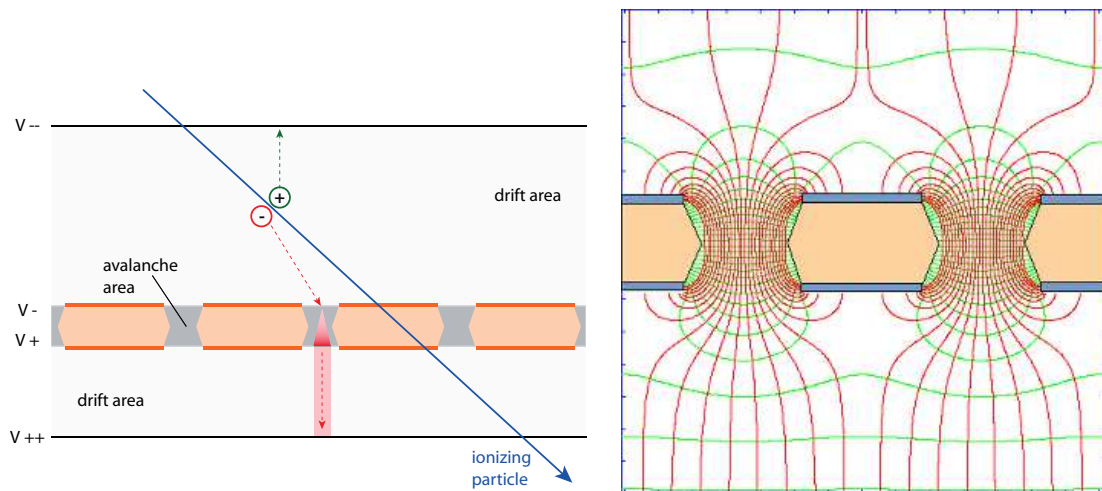
Figure 2.7.: Working principle of a GEM (left). An ionizing particle enters the drift space and creates primary electron-ion pairs. The electrons get multiplied in the region of the highest field strengths, which is between the top and the bottom side of the GEM foil. A closer view of one hole with field lines and equipotential lines (right)[21].

can be realized in copper layers or ceramic layers on printed circuit boards. The limits for the position resolution are the fabrication tolerances in the photolithographic production processes, which have improved a lot in the past years and the progress in this field has not come to a halt yet.

Gas Electron Multiplier (GEM)

The GEM was invented by Fabio Sauli in the 1990s [22]. The working principle is shown in figure 2.7. Primary electrons that are created by an ionizing particle in the drift area follow the electric field down to the GEM. It consists of a thin polymer foil or printed circuit board with thin copper surfaces and holes. Top and bottom surface are set onto different potentials, creating a very high, but locally limited electric fileld only inside the holes. While the electron drifts through this tiny hole, a charge amplification process sets in with possible gains of about 10^3 to 10^4.

The GEM is only an amplifier and does not provide any readout function which has to be added separately using additional readout strips or layers. There are ongoing research activities on the field of ThickGEMs and stacked multi-GEM arrays that could provide even higher gains and solve the problem of ion back flow through the detector, which can drastically limit the detector operation and lifetime by causing secondary electron emission on the cathode.

Micromesh Gaseous Detectors (Micromegas)

In contrast to the GEM being a pure charge multiplier, the basic Micromegas setup already includes the readout as a part of the detector. Similarly as for the wire tubes, the anode coincides with the readout, but the overall detector geometries differ a lot. Figure 2.8 shows the basic
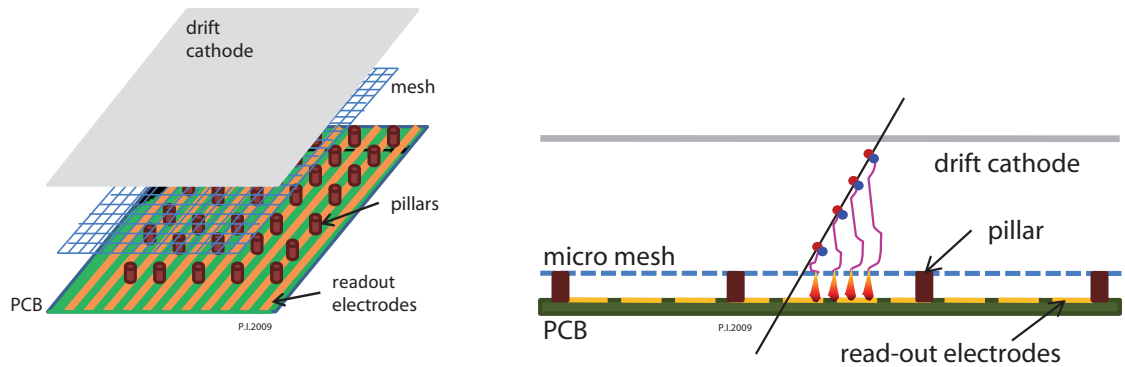
Figure 2.8.: In a Micromegas electrons created at various points in the drift field are amplified between mesh and anode strips [12]. The anode strips build up the readout which is integrated into the detector design.

working principle and setup of this type of detector.

For the Micromegas, the drift space and the amplification area are separated by a thin metal mesh that can be set to high voltage. Ceramic pillars are etched via photolithographic techniques onto the anode surface and hold the mesh in place without providing electrical contact. All surfaces like anode, mesh and cathode are strictly parallel and therefore allow for a homogeneous drift of charged particles and amplification fields.

Primary charges created in the drift area are guided by the drift field through the mesh into the amplification area, where the avalanche processes start and charges get multiplied.

All dimensions are very small, especially the distance between mesh and anode, which is only about 100-150 μm for most Micromegas. This leads to very short ion collection times and very locally limited avalanches. The result is a remarkably lower dead time fraction and an improved rate capability compared to common wire tubes. Coming along with the miniaturization of the readout are also a good position and time resolution. The readout geometries itself vary from strips of various widths and lengths to pixels on pads depending on the general requirements for the specific application.

Needed voltages for detector operation are comparatively low and the units are easy to handle and affordable. A production process has been developed which creates qualitatively good detectors. Efforts to produce large area (about $1\,\mathrm{m} \times 2\,\mathrm{m}$) detector units for the use within large high energy physics detector modules show first promising results.

2.2.2. The Problem of Discharges for Micromegas Detectors

One major drawback of the Micromegas design is the incidence of discharges in the amplification area. They can heavily damage the mesh and the readout electronics of the detector. It can also

(a) Parallel plate geometry: Micromegas
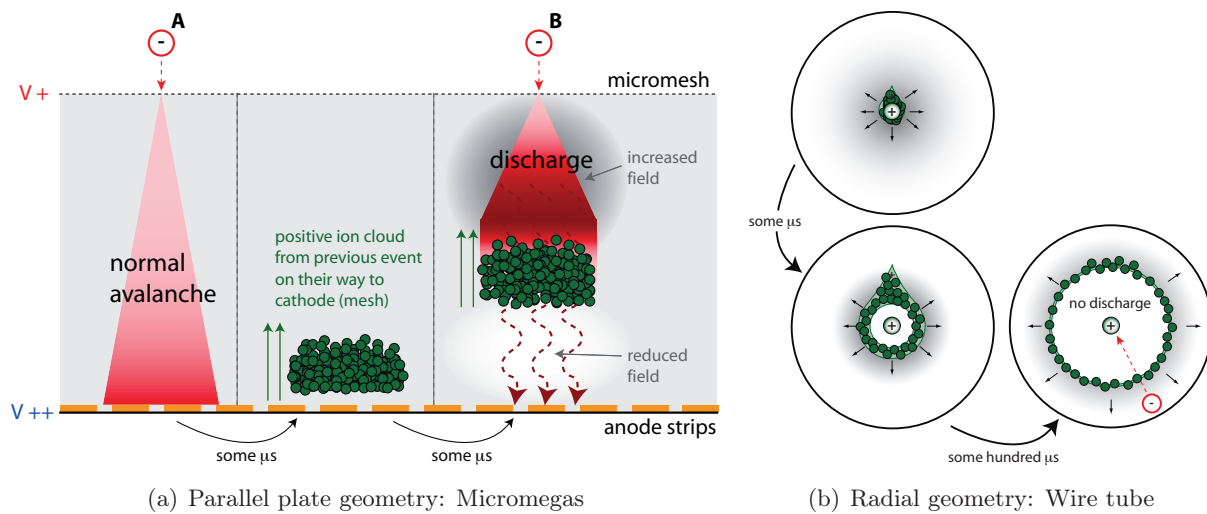
(b) Radial geometry: Wire tube

Figure 2.9.: Left figure: Development of a streamer or discharge in a parallel plate geometry of a Micromegas. Right figure: Distribution of charge in radial geometry avoiding discharges.

lead to increased detector dead times as a result of possible HV breakdowns.

This problem arises from the fact that high gains (comparable to those of the classic wire tubes) are wanted for many applications, because stronger signals simplify the data acquisition and have a much better signal-to noise ratio. Amplification factors around 10^4 are needed in order to guarantee a good signal, but for local charge developments in a single avalanche of the order of 10^7 up to 10^8, the Raether limit is reached. If these conditions are reached by a rare high energetic particle, a discharge is unavoidable. But in a high energy physics detector environment, it can easily happen that a slow alpha particle or some debris from neutron-interactions produce the critical primary ionization of around 1000 electrons over the typical lateral extent of an avalanche, which causes discharges.

The development of a streamer or discharge in a parallel plate geometry of a Micromegas is illustrated in figure 2.9(a): After the first event (A), the ions that were produced in the avalanche keep close together because of the homogeneous electric field and drift as a cloud towards the mesh. The drift process only takes a short time, since the distance between mesh and anode are very small (i.e. $128\,\mu$m for typical Micromegas), but in the whole area the electric field is high enough for gas amplification to take place. The probability of a new primary electron entering this area increases with the overall particle rate in the detector. The next primary electron coming from the drift area of the detector (B) arrives in an area of increased field strength, because the positive space charge increases the field above it, but decreases the field below it. The avalanche starts and develops quickly into a critical discharge. Even though the field strength below the ion cloud is significantly lowered, the numerous avalanche electrons are able to drift though this area and reach the wire.
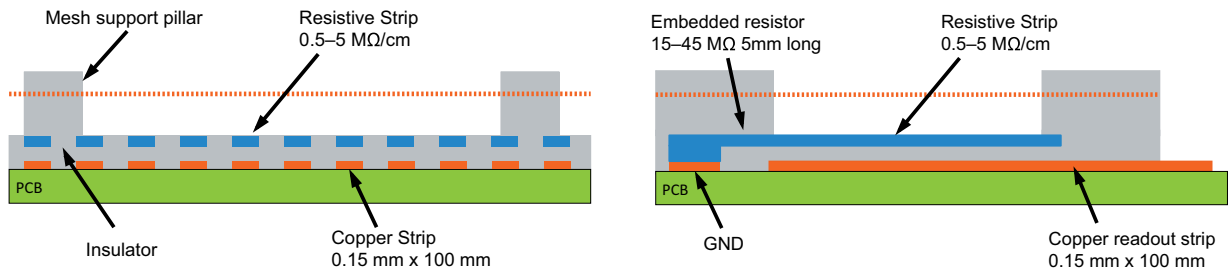
Figure 2.10.: The spark protection system uses resistive strips and capacitive coupling to decrease discharge intensities and prevent the readout from damage [12].

If the field strength and the incident particle flux is very high, it can also happen that a continuous plasma discharge is ignited and does not quench anymore by itself, which can seriously damage the mesh.

There are several approches to deal with this critical issue or to avoid it. One is to avoid the high concentrations of charge by spreading the charge quickly after creation over a larger area. This will affect the design and the geometry of the readout area. Another possibility is to make the detector insensitive to sparks by protecting the vital parts of the readout and limiting the discharge currents.

Classical Wire Chambers: Radial Fields

Classical wire detectors also show the phenomenon of sparking, but the reachable gains without sparks are much higher. The charge of an avalanche is created around the whole circumference of the wire. Also the distribution of charge for a radial geometry is much more efficient than for parallel plate geometry, where essentially only the diffusion causes the charge to spread out.

The increase of the electric field only affects the area between cathode and ions. After creation in the avalanche, ions almost immediately leave the amplification area with the high electric field in the closest vicinity of the wire and spread quickly, while the volume of the cloud increases with 2π times the radius, as shown in figure 2.9(b).

The radial electric field is the key effect for the decreasing discharging affinity of the wire tubes with respect to the Micromegas, which have parallel plate geometry for cathode and anode. A more radial electric field in the amplification area of the Micromegas could raise the limits for the gain in safe operation of the detector. A possibility would be to influence the field geometry with additional potentials, trying to reach a field configuration similar to a MWPC, see also chapter 5.1 and 5.4.

Resistive Layers

Another possibility to solve the discharging issue is to not prevent the discharges to occur, but to protect the sensitive parts of the detector. A spark-protection system consisting of a layer of resistive strips on top of the anode strips can be used to make the readout insensitive to the sparks.
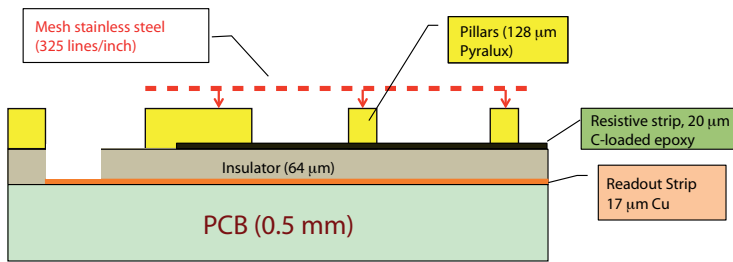
Figure 2.11.: ATLAS chose to use this Micromegas setup for the NSW with resistive layer technology [12].

It is no longer directly exposed to the charge created in the avalanche area. The readout strips are capacitively coupled to the resistive strips. The general setup of such a resistive spark-protection can be seen in figure 2.10.

The resistance of the additional layer also causes the spark intensity to decrease by approximately three orders of magnitude. The electronic signals of the avalanches are not lost through the resistive layer, but a reduction in signal height cannot be avoided. The complete electric separation of the Micromegas and the readout electronics provides additional safety for the data acquisition, on the other hand the exclusively capacitive coupling of the signals may lead to additional noise and crosstalk, which needs to be studied carefully.

Micromegas for the New Small Wheel in ATLAS

Despite the discharge issues, the mentioned advantages of the new technology and the detector properties lead to the decision that Micromegas in combination with other technologies will be suitable for the New Small Wheel design to replace the existing CSCs and MDTs in the high particle flux area of the ATLAS muon detector. The design for the Micromegas used in the NSW also uses the spark protection consisting of the additional resistive strips as shown in the previous section. It can be seen in figure 2.11. The amplification gap is chosen to be $128\,\mu$m and the strip pitch will be between 0.425 mm and 0.445 mm. The usual potential setup used for most Micromegas applications sets the mesh on a negative voltage and the readout on ground, but test measurements showed a more stable operation with the mesh on ground and the readout on positive high voltage. Additionally, the voltage stability on the mesh after a discharge is better for a grounded mesh.

2.3. Other Physics Effects Related to Gaseous Detectors

Between creation of the primary ionization and the gas amplification near the anode in a gaseous detector, electrons an ions travel according to the applied electric potentials and fields to the anode or respectively the cathode. Drift behavior and diffusion processes of these particles in the surrounding gas atmosphere become therefore significant. In the avalanche process the *Penning effect* leads to a remarkable increase of the gain. This will shortly be described here, as well as the photoelectric effect that creates the probing electrons for the investigation of the test MPGD.

(a) Ramsauer curve for Argon [24]
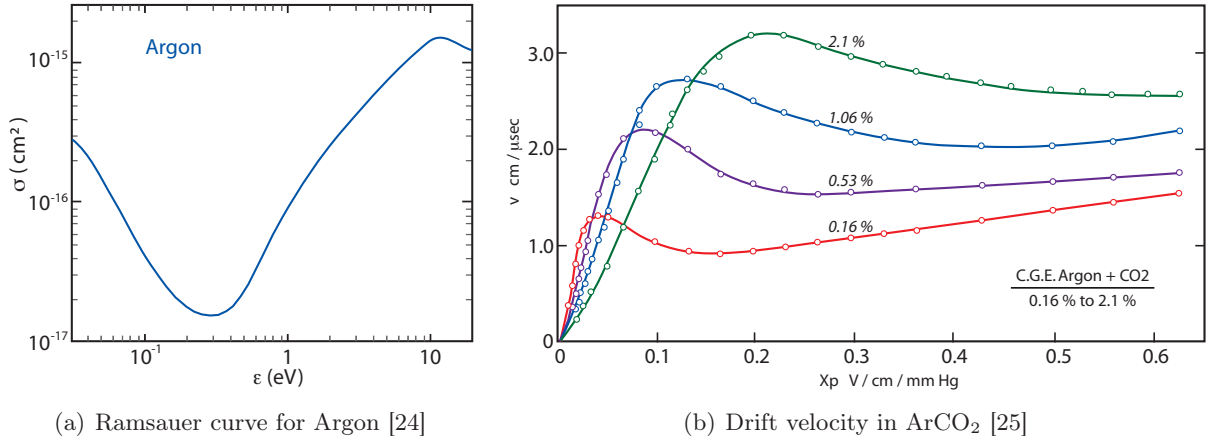

(b) Drift velocity in $ArCO_2$ [25]

Figure 2.12.: The drift velocity of electrons in gas can be a highly non-linear process and depends on the Ramsauer effect (here for argon gas). The example of a drift velocity curve ($ArCO_2$) shows a maximum which is strongly depended on the gas composition and the CO_2 fraction [14] (right).

2.3.1. Electron Drift

In the presence of an electric field electrons follow the gradient of the potential towards the anode. The electromagnetic force accelerates them, while collisions with the surrounding gas molecules slow them down. After a short time they reach an average drift velocity that depends on the field E and on τ, the mean time between collisions, depending on pressure, temperature and the specific gas composition. The drift velocity w can, according to Townsend [23], be expressed as

$$w = \frac{e}{2m_e} E\tau. \tag{2.13}$$

The drift velocity curve can be very non-linear and is characteristic for the drift gas, since τ can vary strongly with E for some gases, also called 'non-linear' gases. It can even have maxima and minima due to the Ramsauer effect that causes large variations in the the cross sections of the electron interaction with the gas molecules due to quantum effects. An example of such a drift curve of the gas mixture $ArCO_2$ for varying parts of CO_2 is shown in figure 2.12.

For given temperature T, pressure p and under the assumption that only an insignificant fraction of electrons undergo ionizing collisions, the energy distribution of the drifting electrons can be written as [14]

$$F(\varepsilon) = C\sqrt{\varepsilon}\exp\left(-\int\frac{3\lambda(\varepsilon)\varepsilon\mathrm{d}\varepsilon}{[eE\lambda(\varepsilon)]^2 + 3\varepsilon kT\Lambda(\varepsilon)}\right) \tag{2.14}$$

with $\lambda(\varepsilon) = 1/(N\sigma(\varepsilon))$, N being the Avogadro constant and $\Lambda(\varepsilon)$ the energy lost on each inelastic collision. $F(\varepsilon)$ can be computed if the elastic and inelastic cross sections of the gas are known. This leads to

$$w(E) = -\frac{2}{3}\frac{eE}{m_e}\int\frac{\partial[F(\varepsilon)\,u^{-1}]}{\partial\varepsilon}\,\mathrm{d}\varepsilon \tag{2.15}$$
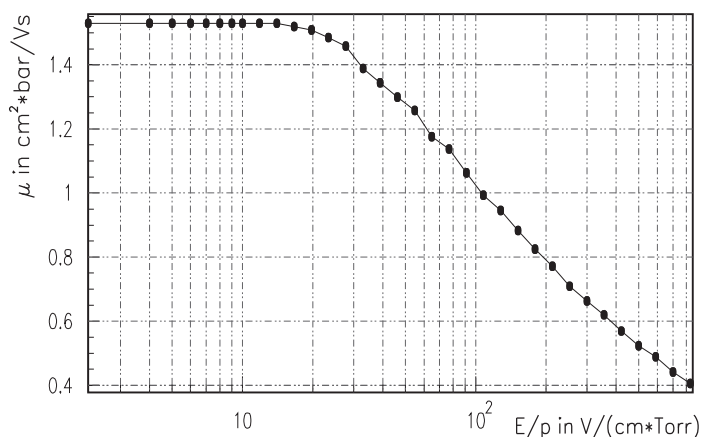
Figure 2.13.: Ion mobility of Ar^+ in Ar [26]. The ion mobility is constant except in the higher electric fields that are present only in the nearest wire proximity (typically less than $100\,\mu$m around the wire anode for a wire tube)

for the drift velocity with $u = \sqrt{2\varepsilon/m_e}$ as the instant velocity of the electrons of energy ε.

For gas mixtures the cross sections of the gases i need to be weighed with their fractions p_i:

$$\sigma(\varepsilon) = \sum_i p_i\sigma_i(\varepsilon) \qquad \text{and} \qquad \sigma(\varepsilon)\Lambda(\varepsilon) = \sum_i p_i\sigma_i(\varepsilon)\Lambda_i(\varepsilon). \tag{2.16}$$

2.3.2. Ion Drift

Most of the ions in a gaseous detector are produced near the anode wire in the avalanche process. They are attracted by the cathode and drift in the opposite direction of the electrons with a constant average speed of

$$v_{ion} = \mu \cdot \frac{E}{p}, \tag{2.17}$$

if the reduced electric field E/p is not too high, with E being the electric field strengths and p the gas pressure in the drift space. The mobility μ of ions in gases strongly depends on the gas composition. Figure 2.13 shows the mobility of Ar_+ ions in Ar for different reduced electric field strength E/p. For values up to $20\,\text{V}\,\text{cm}^{-1}\,\text{Torr}^{-1}$, μ can be considered to be independent of E/p.

For gas mixtures of gases G_i the mobility μ_i^+ of the ion G_i^+ is

$$\frac{1}{\mu_i^+} = \sum_{j=1}^n \frac{p_j}{\mu_{ij}^+}, \tag{2.18}$$

with p_j being the gas concentration of gas G_j in the gas mixture and μ_{ij}^+ the mobility of ion G_i^+ in gas G_j. Ions can transfer their charge in collisions to the gas admixture with the lowest ionization potential. Therefore, for some mixtures the mobility can considerably differ from the values for the pure gases.

2.3.3. Diffusion

Diffusion of molecules or charge inside another medium occurs naturally due to the thermal energy of the molecules. They undergo a random walk and spread out inside the surrounding medium over time. This results in a complete mixing of all different types of molecules in a volume for long times. Unavoidable natural diffusion is very often the limiting factor of the position resolution of any type of drift detector.

Fick's Laws: Classic Diffusion

Adolf Fick published his studies on the process of diffusion in 1855. Fick was able to describe it mathematically and to define a diffusion coefficient D. It is a proportionality constant between the diffusive flux due to thermal movement of the surrounding medium particles and the gradient in the concentration of the medium. Fick formulated two basic laws in his theory. One is called 'Fick's first law' and gives the relation between the diffusive flux J to the concentration of a probe medium ϕ under the assumption of steady state, which means that the medium properties are constant in time.

$$J = -D\,\frac{\mathrm{d}\phi}{\mathrm{d}x} \tag{2.19}$$

When combining the continuity equation with Fick's first law, the second law is obtained.

$$\frac{\mathrm{d}\phi}{\mathrm{d}t} + \frac{\mathrm{d}}{\mathrm{d}x}\,J = 0 \qquad \Rightarrow \qquad \frac{\mathrm{d}\phi}{\mathrm{d}t} - \frac{\mathrm{d}}{\mathrm{d}x}\,(D\frac{\mathrm{d}}{\mathrm{d}x}\phi) = 0 \tag{2.20}$$

If D is constant in time and in lateral dimension, the following modifications to the equation are allowed:

$$\frac{\mathrm{d}\phi}{\mathrm{d}t} - D\frac{\mathrm{d}}{\mathrm{d}x}\,\frac{\mathrm{d}}{\mathrm{d}x}\phi = 0 \qquad \Leftrightarrow \qquad \frac{\mathrm{d}\phi}{\mathrm{d}t} = D\frac{\mathrm{d}^2\phi}{\mathrm{d}x^2} \tag{2.21}$$

Ion and Electron Diffusion Without Electric Fields

After their creation in an ionization process, charged particles undergo multiple collisions with the surrounding gas molecules and quickly get the average value of the thermal energy of the surrounding gas. This is known to be $\varepsilon_T = (3/2)\,k_B\,T$, which is around $0.04\,\mathrm{eV}$ at room temperature. The Boltzmann constant k_B has a value of $k_B = 8.6173324 \cdot 10^{-5}\mathrm{eV} \cdot \mathrm{K}^{-1}$. The distribution of the energies follows the Maxwellian probability distribution:

$$F(\varepsilon) = C\,\sqrt{\varepsilon}\exp{(-\frac{\varepsilon}{k_B T})}. \tag{2.22}$$

Without any external forces like electric or magnetic fields, point-like charge distributions drift away from their center and the charge density fraction $\mathrm{d}N/N$ in the element $\mathrm{d}x$ gets a gaussian shape:

$$\frac{\mathrm{d}N}{N} = \frac{1}{\sqrt{4\pi Dt}}\exp{(-\frac{x^2}{4Dt}\,\mathrm{d}x)}. \tag{2.23}$$
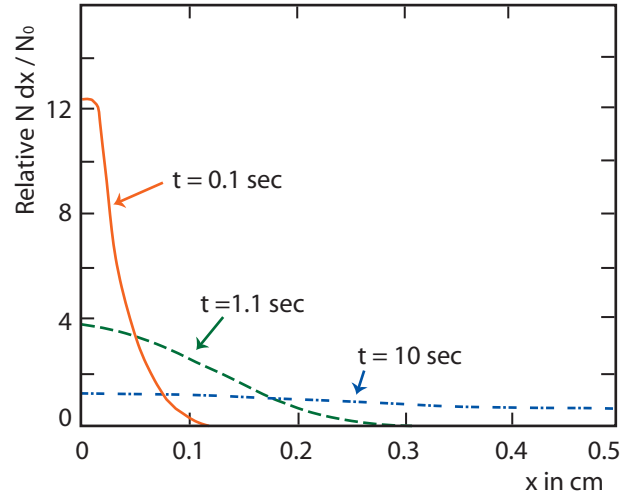
Figure 2.14.: Space distribution of ions in air for different time snapshots, from [14].

D is the diffusion coefficient, while t is the time passing. For $t \to 0$ this shape is a delta peak, while for all other times t, a root mean squared σ of the gaussian is defined:

$$\sigma_l = \sqrt{2Dt} \qquad \text{or in 3 dimensions} \qquad \sigma_V = \sqrt{6Dt}. \tag{2.24}$$

Figure 2.14 shows the space distribution in one dimension of an ion cloud in air after several time intervals ranging from $0.1\,\text{s}$ to $10\,\text{s}$.

With an electric field applied in drift direction, longitudinal and transversal diffusion are not the same anymore. As an approximation, the diffusions in transversal and longitudinal direction will be considered being independent from each other and the transversal diffusion still be described by the above equations.

Diffusion in Magboltz

The Magboltz program [27] was developed by Stephen Biagi in order to be able to determine drift gas properties under given E- and B-fields with a simulation program. The working principle is to simulate an electron inside a gas and considering the external forces, the diffusion and the forces acting between particles in collisions. The program can work with applied electric and magnetic fields at arbitrary angles. The program solves the Boltzmann-equation numerically, which describes the statistical behavior of a thermodynamic system while it is not in its thermodynamic equilibrium:

$$\frac{\partial f}{\partial t} = \left(\frac{\partial f}{\partial t}\right)_{\text{force}} + \left(\frac{\partial f}{\partial t}\right)_{\text{diff}} + \left(\frac{\partial f}{\partial t}\right)_{\text{coll}} \tag{2.25}$$

The probability density function $f(\mathbf{r}, \mathbf{p}, t)$ dependent on the position $\mathbf{r}$ and the momentum $\mathbf{p}$ of the particles changes over time according to the sum of the influences from external forces,

diffusion and collisions between particles. With $\mathbf{F}(\mathbf{r}, t)$ being the external force field (in this case the electric field) and m the mass of the particles, this can be written as:

$$\frac{\partial f}{\partial t} + \frac{\mathbf{p}}{m} \cdot \nabla f + \mathbf{F} \cdot \frac{\partial f}{\partial \mathbf{p}} = \left(\frac{\partial f}{\partial t}\right)_{\text{coll}}. \tag{2.26}$$

In a mixture of gases, this equation holds separately for each of the different particle species, while the collision term also gets components that describe the interactions between each two of the involved particle species according to the corresponding differential cross sections.

Magboltz computes drift velocity, longitudinal and transversal diffusion, gain and attachment of electrons in gases. Therefore, it needs as an input the scattering cross sections and the energy loss per collision, which have been measured before by various experiments and are stored in the Magboltz database.

In the measurements done as part of this thesis, the simulated gas consists mainly of Argon (93%) with a small admixture of CO_2 (7%). The electrons drift at 1.1 bar pressure and the applied E-fields range from 200 to 900 $\frac{\text{V}}{\text{cm}}$, which leads to a range of about 180 up to 800 $\frac{\text{V}}{\text{cm} \cdot \text{bar}}$ for the reduced E-field.

Diffusion in Magboltz is given in units of $\frac{\text{cm}^2}{\text{s}}$ [27]. For the simulations in these studies Magboltz version 9.01 (released 12.05.2012) was used.

2.3.4. The Penning Effect

In certain gas mixtures, the electron multiplication in an avalanche process is higher than the predicted gain value from calculations using the Townsend coefficients only. This so-called Penning effect occurs in an avalanche gas amplification process and can increase the effective gain by a large factor, depending on the gas composition. It increases the number of free charged particles in a specific given gas composition. A metastable bound state of a noble gas atom with an excited noble gas atom is called an excimer. If such an excimer has a larger energy value than the energy needed for ionization of one of the gas components (often organic gases), collisions with the organic gas molecules or radiative decay of the excimers can lead to a secondary ionization. The electron created in this collision participates in the avalanche process and increases the number of free charged particles and therefore the effective gain of this gas composition. In the avalanche, a balance between the rate of transfer reactions and non-ionizing decay of the excited states like excitement of vibration or rotation modes defines the strengths of the gain increase in the given gas composition.

The effective gain increase by the Penning effect is also dependent on the fraction of the admixture of the organic gas, even though already small fractions of organic gas admixtures in noble gases can have a large impact on the gain value. This is explainable by the fact that the total number of excited atoms in a gas is often very high, because the energy threshold for an excitation process is much lower than for ionization, even though the ionization cross sections are much higher than the excitation cross sections.

2.3.5. Photoelectric Effect

The photoelectric effect describes the process in which an incoming photon of an incident beam is absorbed in solids, liquids or gases and an electron is emitted from the surface. It is only possible if the energy of the incoming photons exceeds the energy work function W_L of the cathode material, which are often metals. The photon energy is given by $E_\gamma = h\nu$, with ν being the frequency of the incoming light. Therefore only light with a frequency higher than ν_{th}, the threshold frequency, liberates electrons from the material. All photons with less energy undergo reflection or absorption without electron emission, like excitation of the metal atoms. The work function of the metal is the same as the average electron binding energy and depends on the atomic number and the surface structure of the metal. The photon energy is completely transferred to the emitted electron. If the beam energy exceeds W_L, the remainder of the energy is converted into kinetic energy of the liberated electron:

$$E_{kin} = h\nu - W_L. \tag{2.27}$$

Above the threshold frequency, the rate of the emitted electrons is directly proportional to the incoming beam intensity, but not to the frequency of the light. For linear polarized light, like laser light for example, the direction of the emission of photoelectrons peaks into the direction of the polarization of the incoming beam [28].

3. Setup of the MPGD Test Chamber

This chapter gives an overview over the full setup of the MPGD Test Chamber and describes the steps that have been taken to determine its characteristics and improve them. The chamber was built to measure properties of Micromegas, GEMs or other new types of gaseous detectors for charged particles. It is designed to investigate possible geometries of readout structures for any Micro Pattern Gaseous Detector (MPGD) to study how to eliminate or minimize discharges that can damage the detector. Improving the rate capability without the application of resistive layers would be a key improvement to this new type of gaseous detector. Efficiency studies and single electron response tests are possible.

The measuring principle of the chamber is to imitate tracks of charged particles in a gas volume, rather than using a radioactive source or a test beam to actually create a real track. Photoelectrons are created on aluminum surfaces by a UV-laser in a 3-dimensional drift space above the test candidate and are guided towards it by a homogeneous drift field. They simulate the primary ionization created by a charged particle passing the active detector medium.

The advantages of this method are that no test beam or radioactive source are needed and the spatial and temporal conditions of the creation of the electrons are known very precisely. Due to the modular assembly of the drift space structures, it is easy to control and change the creation points of the electrons above the test candidate.

Also properties of electrons in various gases can be investigated, like diffusion or drift time studies. As an interesting side-aspect, it is possible to find out more about the UV laser photoelectron creation process itself. The chamber design is based on the same principles as the Freiburg Gas Monitoring (GMC) setup [29] used in ATLAS for monitoring the drift gas composition.

Optics, drift field design and the structural setup have been planned and realized with the help of a Diploma student, Stefan Weber [30].

3.1. General Setup

The technical setup of the test measurement chamber for MPGDs consists of the UV-laser and the optical system that splits, focuses and alignes the UV laser beams. They hit the targets inside the gas tight box with the drift field stack that also houses the MPGD test candidate (figure 3.2). A gas mixing system provides the possibility to change the gas composition inside the chamber and the MPGD. An additional readout system, consisting of 18 wires in MWPC layout is positioned just above the test candidate and may be used for reference measurements and control of the electron creation process at the aluminum targets inside the drift field. The readout and data
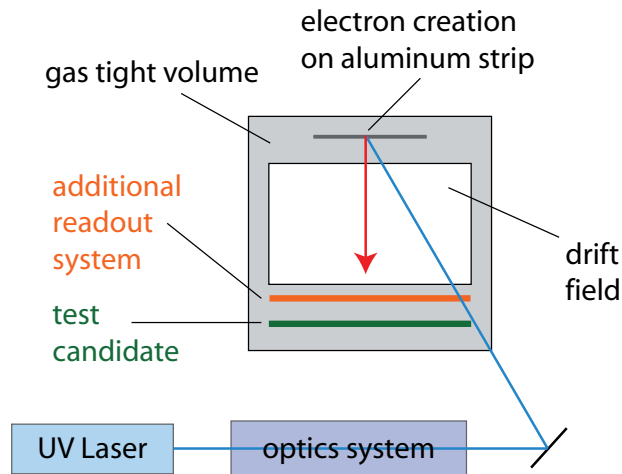
Figure 3.1.: Principle of the test chamber [30]: UV laser light passes the optics system, enters the gas tight volume and creates photoelectrons. Those are guided by the drift field to the test candidate, or to the additional control readout system.

acquisition of the chamber can handle large charge pulses from a wire readout as well as the small signals coming from the strips belonging to a Micromegas or even a GEM.

3.2. Optics and Laser

The purpose of the optics setup is to split up the laser beam into the desired number of partial beams and guide them to the various targets inside the drift space. The overall setup is shown as a technical drawing in figure 3.2. It consists of a 1.30 m x 1.30 m optical aluminum table with a high degree of flatness and good temperature stability.

The laser is placed in one corner and emits pulsed UV light with a wavelength of 266 nm. This is the fourth harmonic mode of the standard 1064 nm line of a Nd:YAG laser. The pulse length is specified to be shorter than 0.65 ns, which results in very small electron clusters with precisely known timings. The maximum output of the laser is about 5 μJ per pulse, it was manufactured by Horus Laser [1]. The laser intensity can be attenuated gradually by a neutral absorber from 97 % to 0 % transmissivity. The neutral absorber consists of a half-wave plate and a linear polarizer. The angle of the polarizer with respect to the half-wave plate determines the relation between the p-polarized and the s-polarized beams that are separated by the linear polarizer (figure 3.3). Only the p-polarized beam is used, while the other one is blocked.

After the neutral absorber the beam is split into 8 partial beams of about the same intensity by a system of seven 0.5/0.5 beam splitters. A drawing of this system can be seen in figure 3.4(a).

---

[1]Type: microchip-laser HLX-U-F002-x21 @ 266 nm, pulse length < 0.65 ns, pulse energy about 5 μJ per pulse, with external trigger option
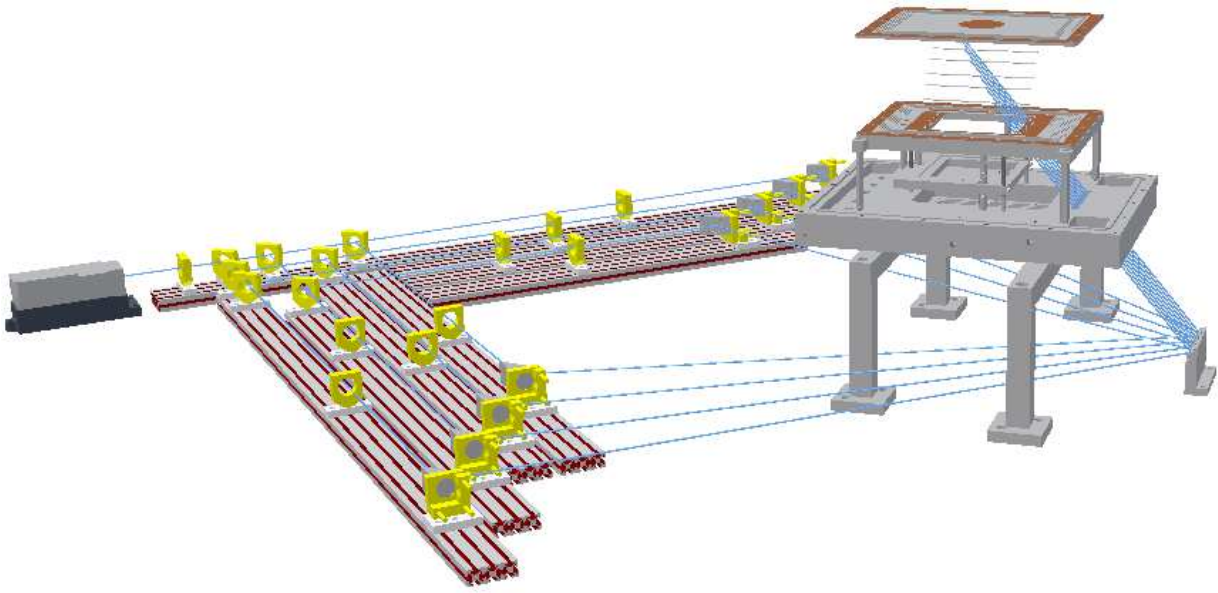
Figure 3.2.: The overall setup as a technical drawing with correct proportions and sizes [30]. The laser beam gets split up and the eight partial beams enter the chamber after being focused and reflected two times in a parallel bundle of beams. For better visibility only the topmost drift field board and the aluminium strips are drawn.

The splitters are specially coated glass plates that split a beam of 266 nm in the correct intensity fractions under an incoming beam angle of 45 degrees. Therefore a right-angled optical path setup is needed in the first part of the optical setup.

The positions of the strips inside the drift volume should be modifiable, so also flexibility of the laser focus points is needed. Technically, the easiest way to bring lasers into a gas tight volume is to use only one window as an entrance, but this unavoidably results in the need of parallel beams while entering the chamber. The distance between the strips in the drift space is fixed and small. Only 1.2 cm between the laser beams do not allow for big mirrors or splitters, because they would need to be placed in such a position that they would obstruct the neighboring beam lines. A special setup with 16 custom made UV mirrors and beam lines at odd angles needed to be designed to fulfill these strict constraints. The main mirror assembly that holds 8 small mirrors of 6 mm diameter is shown in figure 3.4(b). It collects the already split and individually focused laser beams and sends them parallel into the chamber gas volume at an angle of 40 degrees with respect to the perpendicular. For better transmissivity, the quartz window to enter the chamber was not aligned parallel to the surrounding structure, but perpendicular to the entering beam direction.

Pre-alignment and pre-focusing of the laser beams is done while the chamber is removed and the lasers hit an attachable calibration target, where their exact positions are marked. The lens

(a) Functioning principle of the neutral absorber for UV light at 266 nm.

(b) Calibration of the neutral absorber as continuous attenuator, graph provided by the manufacturer OPTIDA
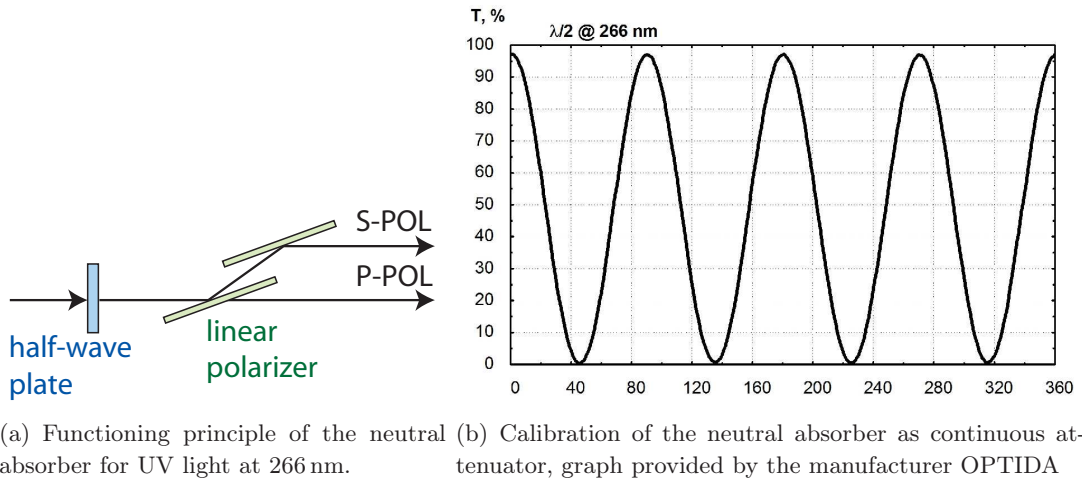
Figure 3.3.: Left: The half wave plate determines the polarization direction of the laser light. P and S-polarized parts are split and only P-polarized light is used in the following setup. Right: The calibration curve of the neutral absorber. The ratio of the P-polarized light as a function of the angle of the half wave plate determines the laser intensity behind the attenuator. A few percent of light are lost at each surface the light needs to pass.

system comprises one lens directly behind the laser, which just parallelizes the beam. While the focal length of the lens is 200 mm in horizontal direction, it does not focus the laser light in vertical direction at all. This special lens is necessary to adapt the existing divergence of the laser beam and create parallel light behind the lens. On each of the eight laser beam arms, a different lens with an individual focal length is used to focus the light onto the aluminum strip inside the drift volume. When the chamber is fully assembled the focusing and the alignment of the optics need to be finalized with the help of the wire readout signals and an oscilloscope. Since the positions of the strips in the drift space can be changed, the focusing system must also adapt all geometry changes over a wide distance range. Together with the other technical restrictions this leads to a large and complicated optical setup with custom made mirrors at individual angles and positions. This is necessary to be able to bring all beams parallel onto the correct places on the aluminum strips in the drift volume.

3.3. Electron Creation with Photo Effect

Inside the chamber the laser beams pass a narrow slit between the test candidate and the drift field stack before hitting the aluminum strips under an angle of 40 degrees. This angle was chosen, because two contrary effects needed to be taken into account. The electron creation efficiency due to the photo effect on the aluminum strips is higher, the smaller the deviation from a perpendicular
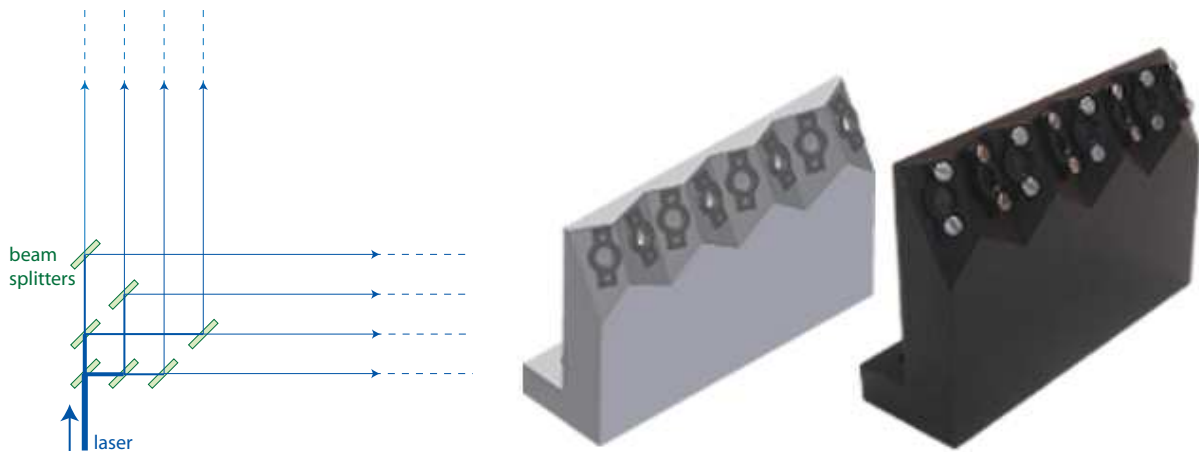
(a) The thickness of the beam line represents the intensity of the beam at this point in the splitting setup.

(b) The main mirror parallelizes the eight partial beams.

Figure 3.4.: Guidance of the laser beams. The parallelizing and splitting of the beam is drawn as a sketch in the left figure, while the in right figure the main mirror is shown as a technical drawing and a photo. It is used to reflect beam lines from various angles with an angle of 40 degrees into the chamber [30].

direction is. But for geometrical reasons, a higher angle reduces costs and the absolute voltage of the drift field stack. The aluminum strips are oriented lengthwise in relation to the laser beams in the drift field in order to avoid strips that are covering neighboring laser beams. Aluminum was chosen as a material, because the laser energy must exceed the electron extraction energy for photoelectron creation. The energy of the laser light is given by $E = h \cdot \nu$, which results in an energy of 4.66 eV for the 266 nm laser. The average extraction energy for electrons in aluminum is about 4.20 eV [31], but varies for different surface treatments. The surface of the strips has been treated to maximize electron creation efficiency even at a relatively high beam angle of 40 degrees. Experiments with different surface treatments in [29] showed that flat grooves on the strip surface perpendicular to the beam direction give best results regarding electron creation efficiency.

A picture of the electron creation geometry is shown in figure 3.5(b). The created electrons simulate the track of a charged particle in the 3-dimensional volume crossing from top left to bottom right, leaving clusters of ionization along the track at different heights and places. The electron creation places can be rearranged easily by changing the order of the drift field boards in the stack.

(a) Insight in the chamber (drawing).

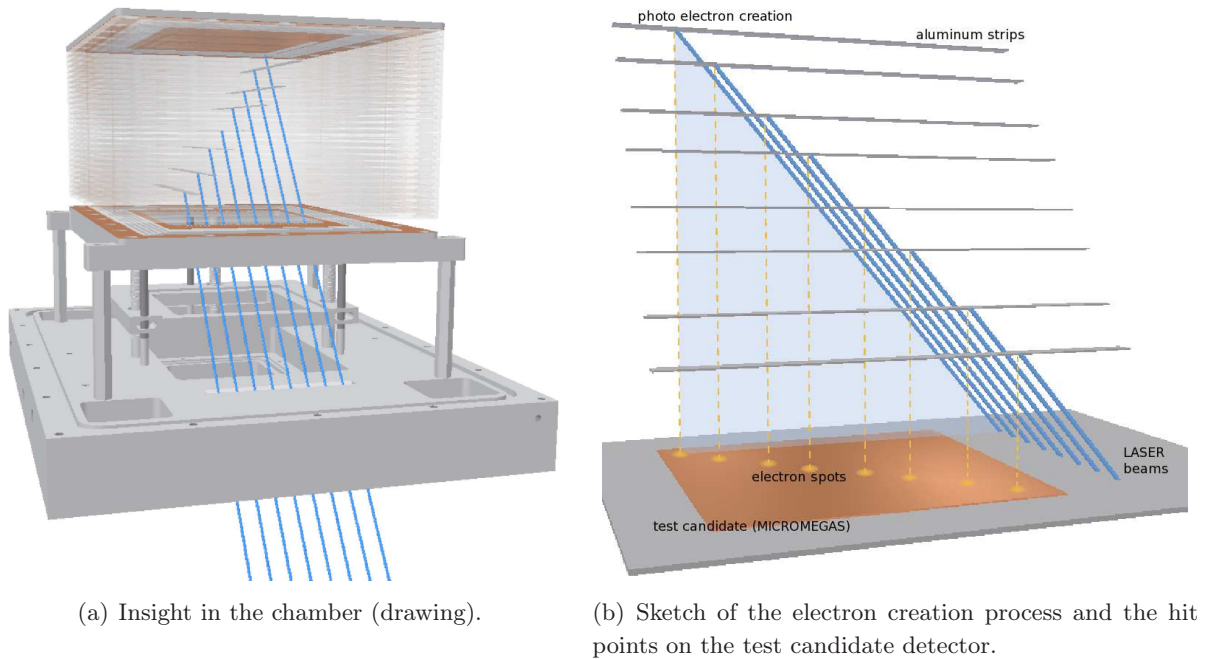(b) Sketch of the electron creation process and the hit points on the test candidate detector.

Figure 3.5.: The parallel laser beams pass a quartz glass window in the bottom of the chamber and enter the gas tight volume. Passing the test candidate narrowly, they enter the drift field from the bottom and hit the aluminum strips. Photoelectrons are created that drift towards the test candidate. The special arrangement of the strips simulate a diagonal passage of a charged particle in the drift space. The electron clusters hit the test candidate at different times and locations, as coming from a diagonal track [30].

3.4. Drift Field Creation and Properties

To guide the electron clusters to the surface of the test candidate without loss of lateral resolution except for unavoidable diffusion losses, the electric drift field must be absolutely homogeneous. This is realized technically by a stack of 29 printed-circuit boards on gradually increasing potentials from top to down, as shown in figure 3.6(a). Each board gets its precise voltage dependent of the overall drift stack voltage by a very precise high voltage divider chain. Its high resistivity limits the current in the divider chain to a maximum of some μA.

A drawing of one of the drift field boards can be seen as an example in figure 3.10(a). The 18 field wires per layer are connected to the surfaces of the boards and therefore are on the same potential as the boards. The wires between the drifting electrons stabilize the drift field inside the large cylindric drift volume of about $100\,\mathrm{cm}^2$. They are positioned with a precision of better than $0.2\,\mathrm{mm}$ and have a diameter of $50\,\mu\mathrm{m}$. The distance between the field wires is $6\,\mathrm{mm}$, with 18 wires per board and 29 boards resulting in a total number of 522 drift field wires. The thin
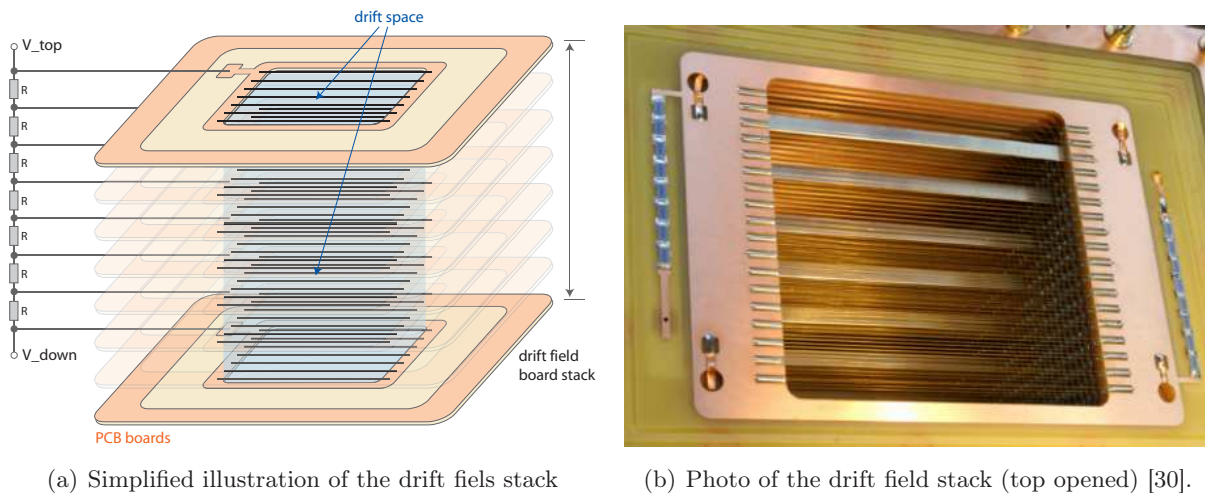
(a) Simplified illustration of the drift fiels stack

(b) Photo of the drift field stack (top opened) [30].

Figure 3.6.: The drift field stack provides a homogeneous drift field to guide the laser electrons without loss of lateral resolution to the test candidate detector. It also supports the aluminum strips inside the drift field mechanically. Right: simplified version of the drift field stack without strips, and less wires and boards. The boards are set on HV via a voltage divider chain. Inside the stack (colored in blue) is the drift volume.

aluminium strips (0.3 mm thickness) are fitted seamlessly into the electrical field design of the PCB boards. They are replacing exactly two neighboring wires by a solid surface and therefore are not disturbing the homogeneity of the electrical field in the surrounding electron drift lines. A photo of the drift field stack without the topmost board is shown in figure 3.6(b). The eight aluminum strips can be seen from the top view in the drift field.

The power scheme of the whole setup is shown in figure 3.9. The voltage of the top of the stack, the last drift field board and the readout board can be set independently. To stabilize the high voltage supplies, filters and bleeding resistors have been installed in the lines. The bleeding resistors permanently draw a small current ($20\,\mu$A) from the power supply to guarantee a stable performance of the HV unit. In the top high voltage line (U_1) a filter has been installed to avoid noise on the stack voltage that could be introduced by the 50 Hz net frequency. The average voltage drop for this filter is about 20 V. The 50 kΩ resistor in the line of U_3, the voltage supply for the reference readout system, has been calculated to cancel out signal reflections due to the open ends on the wires. It also decouples the signal and its small currents from the power supply. Additional power supply filters for U_2 and U_3 have been designed for a cut-off frequency below 50 Hz, but they were not necessary due to the different type and use of the three power supply units.

The voltage applied to the drift field stack can be adjusted from about 2200 V to 12,500 V. This results in a voltage difference of up to 420 V between consecutive boards. The distance

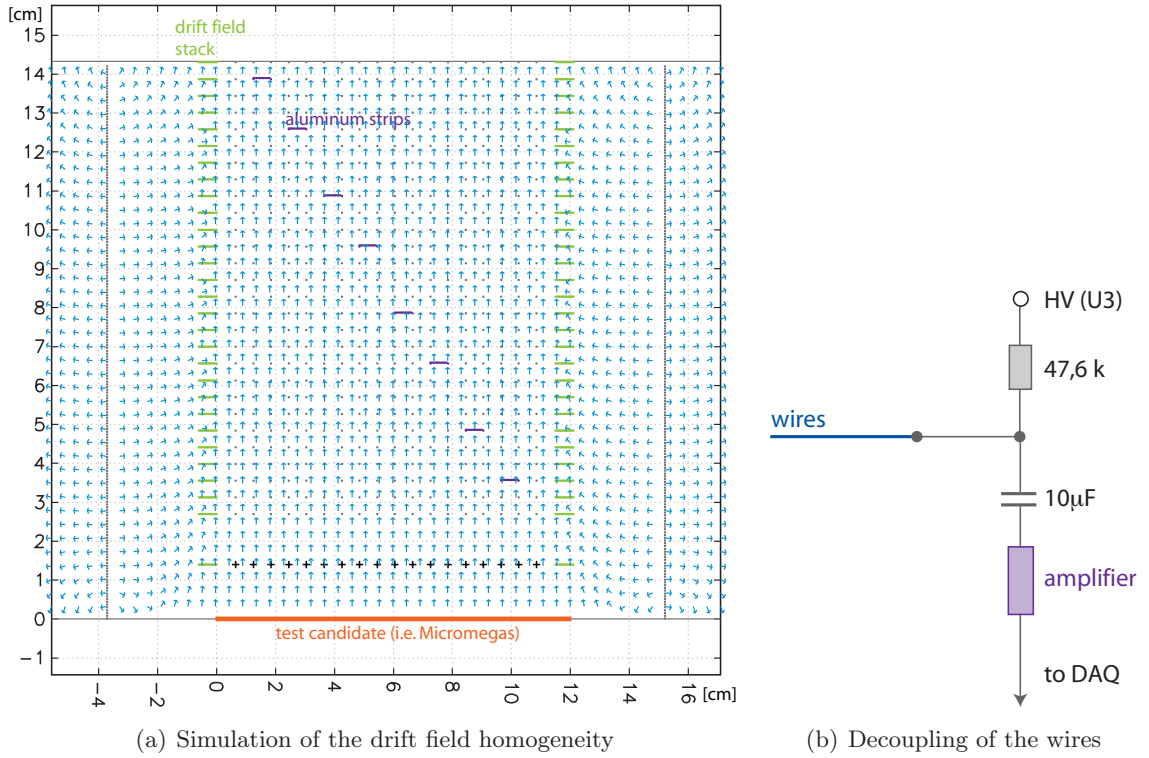(a) Simulation of the drift field homogeneity

(b) Decoupling of the wires

Figure 3.7.: Left: Small arrows show the electric field direction that ions would follow. Electrons created near the aluminum strips will drift into the opposite direction.

between two layers of wires is 4.3 mm, with the height of the board itself of 4 mm and 0.3 mm gap. The distance between the wire layers is set precisely to (4.30 ± 0.01) mm by copper spacers on a threaded bar. They have a low height tolerance and are directly touching each other, while the drift field boards are only held in place vertically by the spacers. The precision of the wires and strips on the boards is therefore around ± 0.02 mm in vertical direction. These specifications result in a total height of the drift field stack of 13.3 cm with possible electron drift distances from 12.9 cm to 2.6 cm.

The laser hits the strips entering the drift volume from the bottom. Simulations with Garfield simulation program show the quality of the drift field inside the drift space. Garfield is a calculation and simulation program for electric field configurations out of given potentials. It can simulate the drift of charged particles such as ions and electrons in these calculated drift fields. Also gas amplifications processes can be simulated with different processes such as ionization, excitation of molecules and elastic and inelastic collisions. The signals of incoming charge on an anode can also be simulated. All this is possible in various gas atmospheres thanks to a large database with cross sections for all the interactions that charged particles can undergo with the surrounding gas molecules.
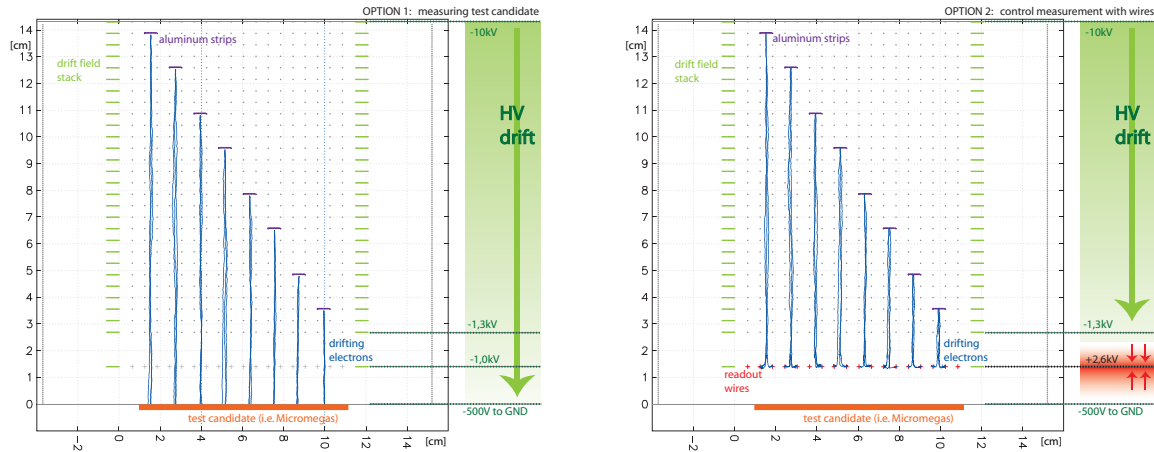
(a) Electron creation and tracking while the reference system is off: Electrons pass the reference system and proceed to the test candidate.

(b) The reference system is activated: Electrons are affected by the positive potential on the wire and get amplified near the wires like in a MWPC.

Figure 3.8.: Operation principle of the reference readout system: if activated, the electrons, which normally reach the detector surface of the test candidate, can be measured independently without changing the setup. Simulation done with Garfield.

The result of the Garfield simulations is shown in figure 3.7(a). The drift field lines are drawn as small arrows pointing towards the direction a positively charged ion would follow in this electric field, while electrons would drift in the opposite direction, towards the bottom. Inside the drift field stack, especially near and below the aluminum strips, the arrows are absolutely parallel, which shows a good homogeneity of the corresponding electric field. The design of the drift field boards is such that it can withstand high potential differences without high surface currents or discharges. A modular assembly and rearranging of the stack is possible with little effort. The test candidate is positioned on a table below the drift field. Its height can be changed easily and adapted to the specific circumstances of the planned measurement.

3.5. Reference System: Redundant Wire Readout

A reference readout system has been installed to verify the number of electrons created on the aluminium strips in the drift space at any time during the measurement. They simulate the primary ionization that is used to test the MPGD. This is why a good knowledge about time, place and number of created electrons is essential for all measurements with this chamber. The lowest board of the drift field stack is mounted with a free gap of the thickness of two boards to the rest of the stack. It can be decoupled via switches from the HV divider chain and be
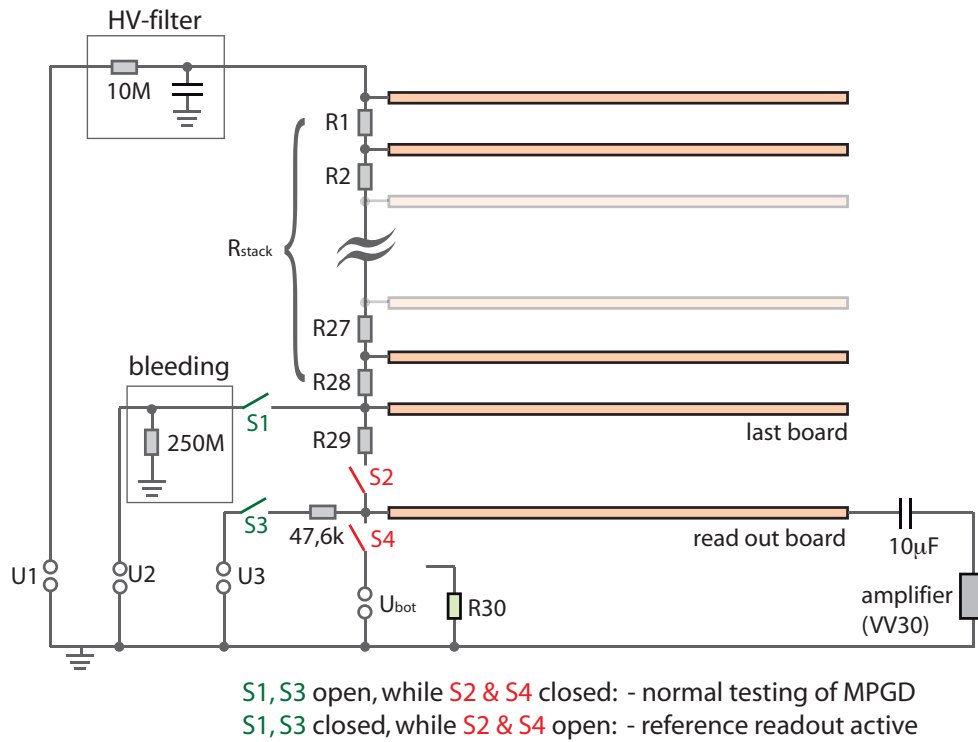
Figure 3.9.: Electric schematics of the chamber: the reference readout can be activated or deactivated, while the high voltage is switched off, but the chamber does not need to be opened or changed otherwise. Results are directly comparable between both modes.

set to a different adjustable positive voltage. Then this layer forms a MWPC together with the surrounding potentials, while it is invisible for drifting electrons in the normal operation mode. A cut-view of the chamber with drifting electrons simulated by Garfield is shown in figure 3.8(a). With the MWPC-mode enabled, the electrons do not pass the readout plane, but head towards the wires on high positive potential, where they get amplified in an avalanche and induce a signal on the wires.

The change between the two usage modes can be done by switches in the electrical setup without the need to open the chamber or modify the readout in any other way than changing some cable positions. The working principle of the reference readout is shown as a simulation in figure 3.8(b).

The signal on the wires in the reference mode is decoupled from the HV via capacitors and resistors (figure 3.7(b)), in order not to damage the following amplifier and the data acquisition, which are presented in section 3.7.

Modification of the Reference Readout System

During the design and assembly of the chamber, only one amplifier was foreseen for all 18 wires on the reference readout system. First measurements showed, however, that the quality of the
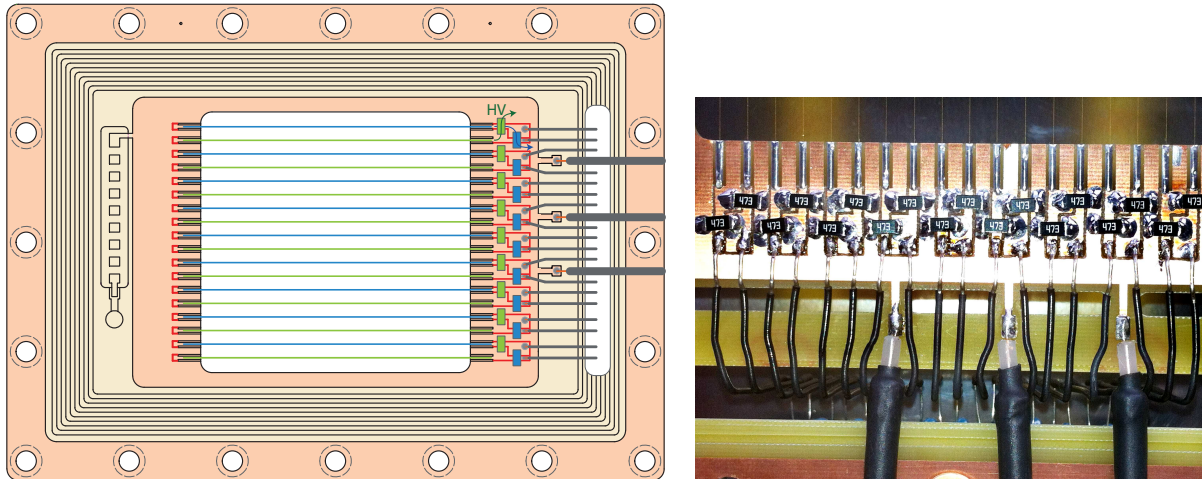
(a) The reference readout board, technical drawing with cuttings (red) and new decoupling resistors

(b) Realization of the separation of the wires

Figure 3.10.: An example for the layout of a drift field stack board. The reference readout wire needed to be separated according to this layout (left), which allowed for each channel an independent decoupling resistor (green and blue) and decoupling capacitor (hanging below the board).

signal was not good enough for precise calibration of the laser electron creation efficiency. Charge was induced on the neighboring wires and signals from different wires overlapped in time. The height of the signal was no longer proportional to the created electrons, because the charge signal was smeared too much over time and exceeded the integration time of the following amplifier.

The only possible solution to this issue was to separate the readout of all wires and to decouple all of them individually from the high voltage as shown in figure 3.10(b). Only small spaces are available and make an unconventional routing on the board necessary. Each wire needs to be decoupled individually by a $47.7\,\mathrm{k\Omega}$ resistor (SMD power resistors with $1\,\mathrm{W}$ maximum power consumption) and a $10\,\mu\mathrm{F}$ capacity. Also 17 additional amplifiers needed to be installed in electromagnetically shielded boxes with a very good ground connection.

3.6. Improvement of the Reference Readout System and Simulations with Garfield

Finding the correct field configuration is extremely important for a good performance of any wire readout. The overall gain value and the lateral gain uniformity strongly depend on the surrounding potentials and the field shape in the nearest wire region.

The existing geometry with readout and test candidate on ground and two different slightly

Figure 3.11.: Possible geometries to improve gain of alternative readout. Geometry A: The readout plane of the reference readout system is put on positive high voltage potential. Geometry B: Readout wires at ground, but additional wire plane shields ground potential of test candidate with strong negative high voltage potential.

changed geometries are possible candidates to realize an electrical field configuration, where all field lines end on the readout wires and gas amplification can take place with a reasonable gas gain that leads to well-defined signals.

- Geometry A: Set the reference readout on positive HV during measuring mode. An additional high voltage supply would be needed and all distances and potentials checked for possible discharges and surface currents that might appear due to the new electric configuration. This includes the geometry with readout on ground potential.

- Geometry B: Modify the drift field stack in such a way that another layer of negatively charged wires below the readout plane creates a repelling potential and forms a symmetrical field near the readout plane. The drift field stack needs to be changed severely in a time consuming procedure, but no additional equipment needs to be used.

All geometries were simulated with Garfield [32] version 9 to find the best possible field configuration for the given setup. A set of variables was defined for each geometry, which would be varied during the simulations, to find if there is a stable configuration of variables to operate the chamber with a high gas gain and smooth drift field lines around the readout wires.

The simulations concern the voltage on the wire readout (U_+), on the lowest drift field board (U_d) and the distance of the test candidate (d) for geometry A. Geometry B concentrates on the variation of the voltage of the retardation wire plane (U_-), while also looking at the voltage of the lowest drift field board (U_d) and the test candidate distance (d). The various simulation parameters are summarized in figure 3.11 for both geometries. The simulation allows to estimate the achieved gain for the given combination of input variables as well as the relation of the field strength above and below the readout wire plane. The latter is an indicator of the uniformity of the field in the avalanche region close to the wires and therefore also of the stability of the gain value for electrons created at slightly different locations on the aluminum strip in the drift field.
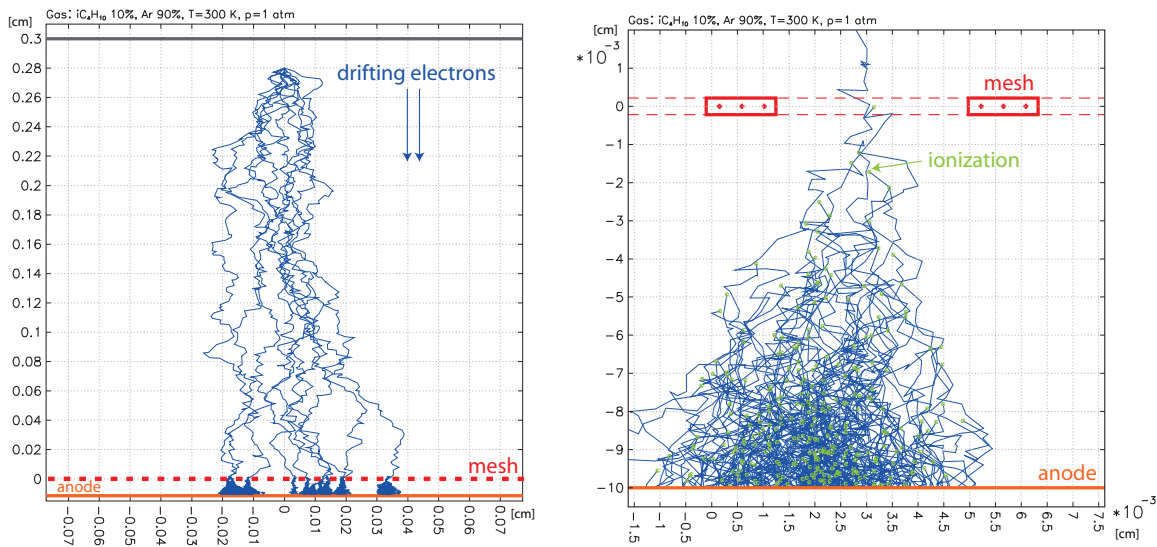
Figure 3.12.: The Garfield simulation program can also track particles in an electric field high enough for an avalanche amplification process. In the left picture, an example of an avalanche simulation is shown. Electrons start at a given point in the drift volume and are tracked to the Micromegas surface. The lateral width of the electron cloud is due to diffusion processes. Many changes of the moving direction show elastic collisions with the gas atoms. After passing the mesh, the electrons get amplified in an avalanche process, as shown in detail in the right picture.

Simulation Sequence

A geometry input file was generated automatically for each possible set of the parameters above. Due to very long computing times, each geometry input file was sent to a computing cluster to be processed with Garfield. Garfield computes the whole electric field configuration of the given potentials on the surfaces and wires in the geometry file. It creates electrons at locations close to the aluminum strips and tracks them on their way down through the chamber until they reach the amplification region and the charge amplification process near the readout wires starts. Garfield calculates and applies the probabilities for any interaction of the drifting particles with the molecules of the surrounding gas such as ionization, elastic and inelastic scattering, excitation and attachment. During ionization, produced secondary charges are treated like the primary charge and are tracked from their point of creation on towards the anode wire. A picture of such an avalanche process is shown in figure 3.12.

The created charge in an avalanche is averaged over 100 started primary electrons for each of the geometry configurations (about 300 configurations in total). Also field line plots including equipotential lines are created and stored for each configuration.

Results of the Simulation

The simulations showed an exponential increase of the gain as a function of both of the varied voltages, see figure 3.13. Only the closest possible distance d gave satisfying gain results in general. For geometry A the most linear increase of the gain (on logscale) can be found for $U_d = -1000\,\text{V}$ (U_+ varying) and for $U_+ = 2000\,\text{V}$ (U_d varying).

Both of the simulated geometries, A and B showed satisfying results. It was also possible to find a good working point regarding the gain for both geometries, while still achieving a uniformly shaped and symmetric field configuration around the wires.

In figure 3.14(a) a field plot with a good overall configuration ist shown. The equipotential lines around the wires have the typical shape of the field lines of a MWPC. Detection efficiency and gain of this configuration are acceptable, since all drift lines end on wires. A high efficiency at this point is essential to allow for best control of the monitoring of the primary ionization by the laser in the final measurements. Choosing the right gain factor is depending on two mechanisms. The gain must be below the Raether limit, which is set at about 10^7 to 10^8, but first discharges start much earlier, see also section 2.1.4. It should also be high enough to achieve signals strong enough for the preamplifier to process.

In contrast, in figure 3.14(b) results of the simulation with a suboptimal field configuration are shown. The electron drift lines, which are equivalent to the electric field lines, do not all end on the wires, but a large percentage reaches the test candidate surface. The same would happen to the drifting electrons that just follow these drift lines, pass the wire plane and could not be detected by the reference readout. The reason for this behavior is that the potential difference between the test candidate and the wires is too low to decelerate the drifting electrons, while the electric field strength between the wires and the last drift field board is clearly sufficient for amplification. The result would be an extremely low gain with small signals barely measurable.

Interpretation of the Simulation Results

Due to the easier technical realization of geometry A, this solution was chosen and another HV supply was installed to be able to set the reference readout plane to the calculated voltage. The optimal working point for this setup foresees a reference readout voltage of $U_d = +2500\,\text{V}$ with the last regular drift field board at around $U_1 = 1000\,\text{V}$ to $1500\,\text{V}$, with a minimal distance d of the test candidate to the readout plane of about $0.7\,\text{cm}$. This is the compromise which is needed between a homogeneous field configuration and the achieved gain while still having a large enough range around the working point where the output values are all stable and do not increase or drop dramatically in dependence of the input parameters.

3.7. Data Acquisition and Triggering

The chamber pulses from the wires as well as those from the test candidate are too small to be processed by the data acquisition without previous amplification. An amplifier of the type
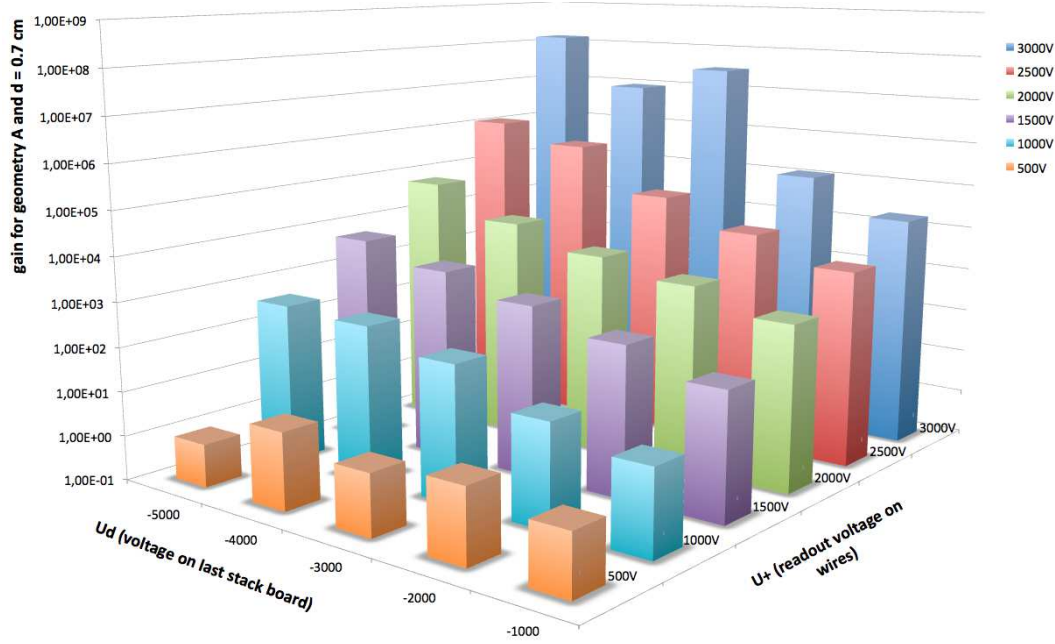
d	Ud\U+	3000	2500	2000	1500	1000	500	0	3000	2500	2000	1500	1000	500	0	ideal
8.7 cm	-5000	9,1E+04	3,1E+04	7228	2604	1278	372	72	2,67	-3,00	-3,50	-4,33	-6,00	-11,00	n.A.	
	-4000	1,2E+04	5439	1468	724	311	43	7	-2,33	-2,60	-3,00	-3,67	-5,00	-9,00	n.A.	
	-3000	2321	853	412	119	56	14	3	-2,00	-2,20	-2,50	-3,00	-4,00	-7,00	n.A.	-0,15
	-2000	664	149	93	25	11	5	1	-1,67	-1,80	-2,00	-2,33	-3,00	-5,00	n.A.	
	-1000	132	39	14	7	3	1	1	-1,33	-1,40	-1,50	-1,67	-2,00	-3,00	n.A.	
6.7 cm	-5000	1,4E+05	3,4E+04	6689	2691	760	230	51	-2,67	-3,00	-3,50	-4,33	-6,00	-11,00	n.A.	
	-4000	1,6E+04	3896	1421	730	306	45	8	-2,33	-2,60	-3,00	-3,67	-5,00	-9,00	n.A.	
	-3000	3268	1264	444	180	46	13	3	-2,00	-2,20	-2,50	-3,00	-4,00	-7,00	n.A.	-0,19
	-2000	665	240	73	30	11	4	1	-1,67	-1,80	-2,00	-2,33	-3,00	-5,00	n.A.	
	-1000	119	50	14	7	3	2	1	-1,33	-1,40	-1,50	-1,67	-2,00	-3,00	n.A.	
4.7 cm	-5000	1,6E+05	3,3E+04	1,1E+04	2973	1150	180	15	-2,67	-3,00	-3,50	-4,33	-6,00	-11,00	n.A.	
	-4000	1,5E+04	5609	2018	709	279	73	7	-2,33	-2,60	-3,00	-3,67	-5,00	-9,00	n.A.	
	-3000	3438	1546	552	188	56	16	1	-2,00	-2,20	-2,50	-3,00	-4,00	-7,00	n.A.	-0,27
	-2000	865	304	81	33	9	5	1	-1,67	-1,80	-2,00	-2,33	-3,00	-5,00	n.A.	
	-1000	182	63	20	7	3	2	1	-1,33	-1,40	-1,50	-1,67	-2,00	-3,00	n.A.	
2.7 cm	-5000	4,0E+05	4,0E+04	1,4E+04	3143	947	34	1	-2,67	-3,00	-3,50	-4,33	-6,00	-11,00	n.A.	
	-4000	3,5E+04	1,5E+04	2697	802	331	20	3	-2,33	-2,60	-3,00	-3,67	-5,00	-9,00	n.A.	
	-3000	5639	2134	662	212	64	11	2	-2,00	-2,20	-2,50	-3,00	-4,00	-7,00	n.A.	-0,48
	-2000	1525	564	190	38	13	5	1	-1,67	-1,80	-2,00	-2,33	-3,00	-5,00	n.A.	
	-1000	445	122	32	11	4	2	1	-1,33	-1,40	-1,50	-1,67	-2,00	-3,00	n.A.	
0.7 cm	-5000	1,4E+08	1,2E+06	6,2E+04	5481	396	1	1	-2,67	-3,00	-3,50	-4,33	-6,00	-11,00	n.A.	
	-4000	9,0E+06	4,7E+05	1,2E+04	2055	322	5	1	-2,33	-2,60	-3,00	-3,67	-5,00	-9,00	n.A.	
	-3000	3,2E+07	4,5E+04	3830	747	119	2	1	-2,00	-2,20	-2,50	-3,00	-4,00	-7,00	n.A.	-1,84
	-2000	1,2E+05	1,1E+04	1712	249	21	4	1	-1,67	-1,80	-2,00	-2,33	-3,00	-5,00	n.A.	
	-1000	1,9E+04	2913	549	73	8	2	1	-1,33	-1,40	-1,50	-1,67	-2,00	-3,00	n.A.	

Figure 3.13.: Top figure: The effective gain for geometry A at the distance d = 0.7 cm, as a function of the readout voltage U_+ and U_d. Bottom figure: Achieved gain values for the given combination of parameters and the corresponding relation of the field strength above and below the wires. A value of 1 would be the perfectly symmetrical configuration of a MWPC. Green values of the gain (left part of table) are within a range of 50 % to 1000 and field relations (right) within 50 % to a gain value of about 1000 (see chapter 4.3). The best field configuration region is marked in blue.

(a) Acceptable field configuration
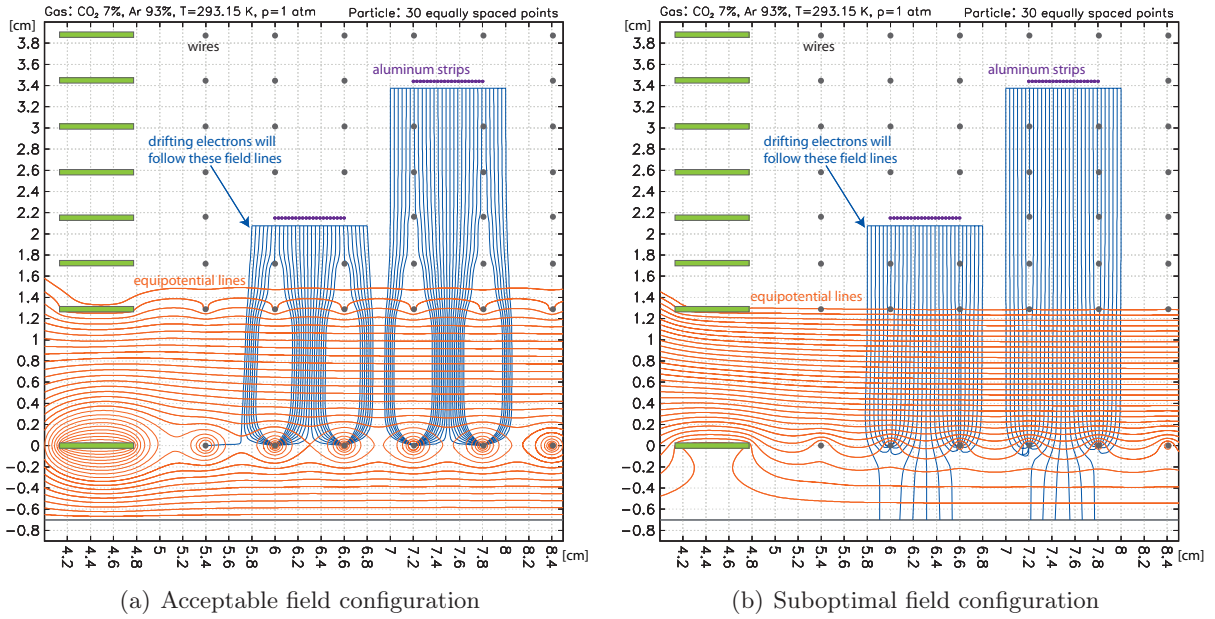

(b) Suboptimal field configuration

Figure 3.14.: Two field configurations are shown for geometry A. Left picture is an example for a correct potential configuration with typical MWPC electric field around wires and acceptable gain. On the right picture the suboptimal field configuration causes electrons to pass the readout plane, the gain is too low.

VV30 [2], which was already used successfully in a previous experiment for gas tubes, is installed and calibrated (see appendix B.1) for each of the 18 wire readout channel and also the 16 test candidate channels.

The data acquisition is done by two 8-channel flash analog to digital converters (FADC) [3] that convert the analog input signal (-0.5 V to +0.5 V with a possible offset of ± 0.5 V) and record the data from all 16 channels into a file. The recorded length of time of an event can be set by software. Also the triggering of the FADC can be done by external trigger signal or via internal trigger conditions. Data files are written by the OS9-controlled acquisition system using the EPIO package [33] from CERN and need to be converted to a root [34] format before further processing and analysis.

Triggering for Laser Induced Events

To record events created by the laser each of the FADCs can be triggered simultaneously by an external pulse. This pulse is created by the laser controller itself. It is a short 5V TTL

---

[2] VV30 amplifiers are manufactured by Uni Heidelberg, the datasheet can be found at http://www.physi.uni-heidelberg.de/Einrichtungen/EW/Geraete/VV030_Vorverstaerker/VV30_Man.PDF and the schematics are in the appendix B.2.

[3] two units of Caen digitizer V1751 with 8 channels each, 10 bit, 1 GS/s FADC

Figure 3.15.: The triggering of the FADC has two different trigger sources: The laser trigger pulse and the FADC internal trigger (TrigOut_1). The latter only activates the triggering process, if there is no signal (TrigOut_0) from the second FADC, which vetoes unavoidable noise pulses from the environment.

standard positive pulse with a steep rise each time a laser pulse is emitted by the laser optics. This pulse is further modified to fit the following NIM-logic. After one event has been recorded, it is necessary to actively block the trigger input from new trigger pulses until it is released by the FADC with a reset signal when the internal dead time is over and the FADC can process a new event. Figure 3.15 shows the corresponding logical scheme.

Triggering for Self Triggered Events

For calibration purposes it is necessary to trigger signals that are not induced by the laser but by a source. Detailed measurement descriptions follow in section 4.1. Therefore, the FADCs have a internal self-triggering option like an oscilloscope. The thresholds need to be set via software for each channel individually. The trigger can be set to a certain level and be activated or deactivated. The final trigger decision is a logical 'or' of all the trigger levels on all channels.

Background

If the FADCs are triggered by the laser trigger signal, there is no need to compensate electronically for background. The white noise background, induced into the system by noise on the supply voltage of the VV30 amplifiers or entering the cables where they cannot be shielded, has been suppressed by a very good grounding of all parts of the chamber and of every electronic part that processes the signals. Other rare signals are not likely to coincide with the laser-induced pulse and can be easily filtered out during analysis. If the triggering of the FADCs is induced by the signals themselves (passing a certain intern threshold), every rarely occurring noise signal triggers the FADCs. For some recording modes of very long samples, the recording rate is only about 2 to 3 events per second. This is why a good suppression of the noise signals is absolutely essential.

There are two unavoidable sources for noise on the signal inputs of the FADCs. The origin

Table 3.1.: The chosen settings for all measurements that are not triggered by the laser pulse, but by the signal itself (internal trigger mechanism FADC).

setting	value
FADC_0 / channel 1	300
FADC_0 / channel 3	300
FADC_1 / channel 4	310
FADC_1 / channel 5	313
offset	C400 (hex)
post trigger	D0 (hex)

for the first kind of noise signal is the FADC itself. Probably due to a manufacturing error or a bad routing of the FADC busses on the boards, the ethernet communication with the computer induces high frequency noise to the inputs of the FADCs. This effects occurs constantly while the FADCs are sending their recorded data to the computer. On the oscilloscope, short bunches of signals with a frequency of about 50 MHz inside the bunch are visible, but the rate of the bunches themselves is low with about 10 Hz. The voltage of these bunches is too high to be suppressed effectively by raising the trigger levels without cutting into the full spectrum of the source used for the calibration measurements. Since nothing could be done to prevent this noise from entering into the setup, the data recording needs to be avoided while data transmission is happening. Therefore the DAQ trigger gets blocked for 2 ms for new event recording and the DAQ system is then released to wait for the next event trigger.

The second source of noise is some unknown signal that occurs with about 3-10 Hz and is transmitted via the power supply in the building and also via air as electromagnetic radiation. It couples back to any non shielded signal cable or connector and looks like a short high frequency trail on the oscilloscope. Its amplitude differs depending on the positioning and shielding of the cables of the setup. There are periods of several hours or even days, when it vanishes completely, but usually it disturbes the measurement severely. Its amplitude is more than 30 mV behind the VV30 amplifiers.

This noise could not be prevented reliably by any modification made to the setup like double shielded cables or excellent grounding on every electrical relevant part that has any contact with air. The biggest part of the noise seems to enter the system through the power supply of the VV30 preamplifiers. A low pass filter was designed and built to minimize the unwanted noise frequencies in the power supply line. For a schematic of the filter with calculations and a simulation see A.2. It reduces the amplitude for the frequencies above the calculated cut frequency noticeably in the Fourier spectrum of the signal. But the cut frequency cannot be put to a suitable low value, since inductances and capacities of the needed sizes (>100 mH and $>600\,\mu$F) are not easily available, especially such that could withstand the needed current rate of more than one Ampere.

(a) Regions for triggering (illustration)   (b) Trigger thresholds measurement
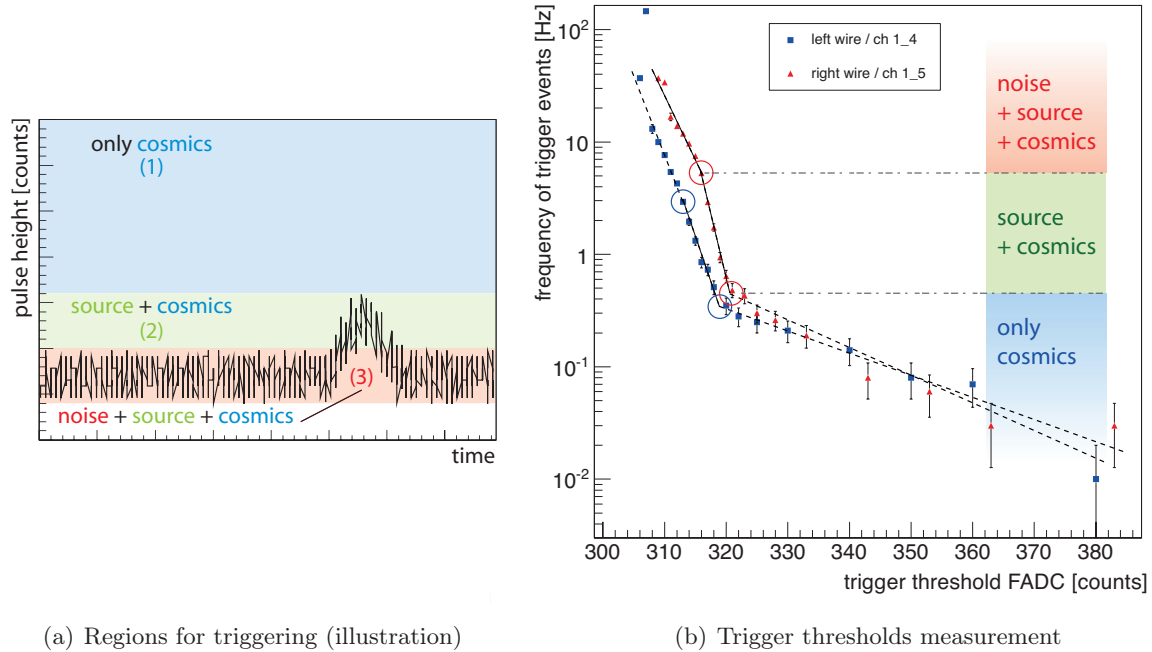
Figure 3.16.: Left: Regions for the trigger threshold measurement. If the trigger level is in region (1), only cosmics can trigger the FADC. For a trigger in region (3), also the unavoidable noise on the input raises a trigger signal. The best noise suppression is obtained by a trigger level in region (2), just one or two FADC counts above the noise level. Right: The measurement of the trigger counts per time shows clearly, where the regions start and end.

One possible solution to this noise issue is to make the setup insensitive to incoming trigger signals induced by the noise. Therefore a veto-triggering mechanism was established, which once activated, blocks the DAQ for a certain time longer than the duration of the noise pulse, which has been set to about 1 ms for safety reasons. The veto-trigger pulse is created by an 'or' combination of two of the channels of FADC_0, which should have no source signal and therefore should be free from signals during noise-free periods. The trigger level for this decision is only a few FADC counts higher than the white noise on the channel, but much lower than the average noise burst on the system. The efficiency of the veto-trigger needs to be the highest achievable, since the already low data recording rate should not be further reduced by any noise events. See Table 3.1 for the values.

Trigger Levels

The trigger levels for the source calibration need to be set to a level just above the white noise in each channel. Therefore the event rates for different trigger levels with the source in the drift

volume have been measured. During this measurement, all background suppression mechanisms were installed and activated. The result of these measurements is shown in figure 3.16(a). Both channels have been measured independently. The curve on a logarithmic scale in figure 3.16(b) shows three parts that can be identified and interpreted the following:

- (1): In this region, neither noise nor source signals pass the trigger threshold. Only the occasional cosmic particle entering the chamber triggers the data acquisition. This relates to a threshold in region (1) in figure 3.16(b).

- (2): Cosmics are still included in this region, but the dominant effect causing counts is the source signal. This is corresponding to a threshold in region (2).

- (3): The noise in region (3) is dominating the count rate, even though all 3 effects are present. On logarithmic scale there is a steep linear rise of the count rate towards the lower end of the threshold spectrum.

For the source measurement, a trigger level that is still in region (2) but very close to region (3) is needed, because the source energy peak is not separated from the noise peak in the spectrum. The noise needs to be suppressed without cutting away most of the signal. The thresholds in Table 3.1 show the final decisions on the trigger levels of channels 4 and 5 of FADC_1 that are used for triggering the source signals. All measurements using these settings show only minimal noise rates and therefore no significant reduction of event recording rate. The data transfer rate from the internal memory of the FADC to the computer via the 10 k ethernet link is still the limiting factor for the event recording rate.

4. Calibration of the Chamber and the Reference Readout System

It is essential to calibrate the test chamber in order to be able to measure the response of the Micromegas to the test electrons quantitatively. The drawing in figure 4.1 shows the whole setup with the important components. There are three processes that need to be measured and calibrated to ensure a good understanding of the setup and to guarantee results that can be quantitatively compared to those obtained with real beams or cosmic rays.

- 1: The UV laser creates photoelectrons on the aluminum strips in the drift volume. The energy of the laser light is sufficient to extract electrons, but the efficiency is not known precisely. It depends on the surface quality, the exact wavelength and strongly on the angle of the incoming laser light. Studies have shown that different surface treatments can increase or decrease the electron creation efficiency [29]. A possibility to determine the efficiency is to measure the reaction of the system to the laser pulses and compare it with the reaction to a radioactive source producing a well known number of primary ionization. This will be described in this chapter with a ^{55}Fe source that emits x-ray radiation of $5.9\,\mathrm{keV}$.

- 2: The gain of the reference readout needs to be determined. This is the most challenging part, since the wire signals are too small to be measured without amplification and the VV30 in use amplifiers are not strictly charge amplifiers, but voltage amplifiers. Since the overall reaction of the system is already calibrated with the source, it is possible to calculate a factor that gives the voltage output of the amplifiers for a certain amount of primary charge. Additionally, the gain itself can be simulated with Garfield, which has been done in chapter 3.6. This will be discussed and compared to the measurements.

- 3: The VV30 amplifier factor is known from the datasheet to be 48 for nominal supply voltages. This is a very vague value, since the amplifier gain is dependent on the exact supply voltages, the temperature and the individual tolerances on the used resistors, capacitors and transistors. Since the used amplifier model is not a charge amplifier, it is necessary to understand the pulse shape and time constants of the pulses on the redundant wire readout. After calculation of the correct shape and constants, a calibration pulse unit has been developed and built that imitates the wire pulses. It has been used to calibrate the VV30 amplifiers. Also the influence of temperature changes on the output voltage of the amplifiers has been studied.
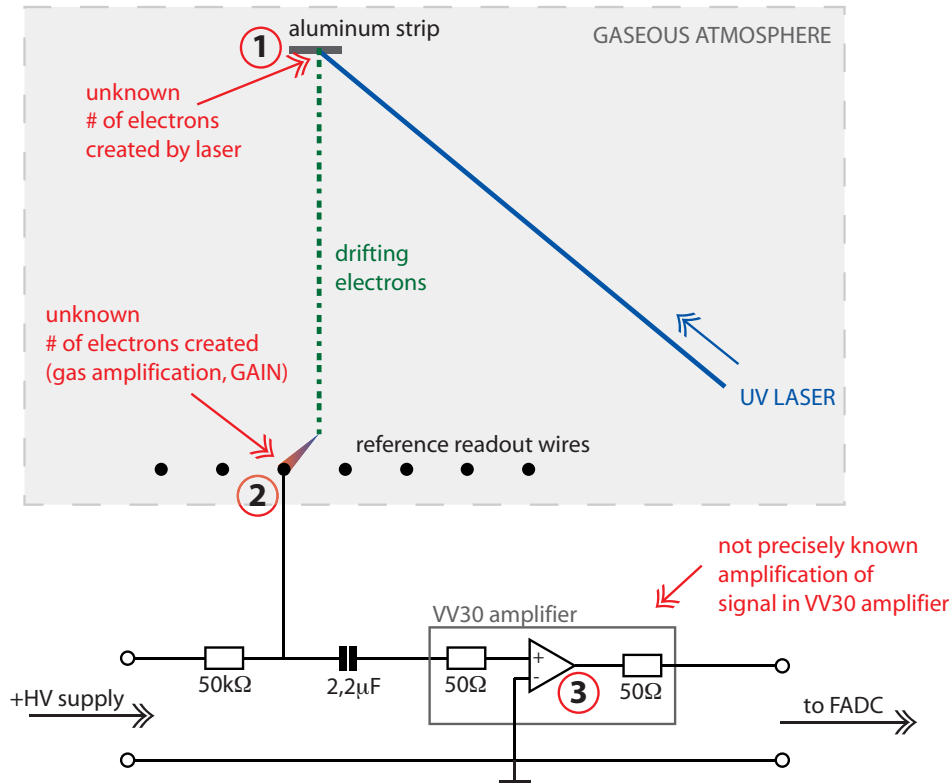
Figure 4.1.: The signal creation for the reference readout inside the chamber with the different conversion processes that need to be fully understood and calibrated.

Since the amplifiers of the type VV30 are no charge amplifiers but voltage amplifiers, a different and more complicated order of calibration measurements must be followed. To obtain a full calibration of the setup, a source measurement is performed first, which delivers a context between the voltage output of the VV30 amplifiers and the primary charge inside the drift volume. Theoretical calculations for the MWPC reference readout give the signal form and the time constant of the wire pulses. A calibration pulse unit that imitates these pulses with a constant and defined amplitude is the basic measurement tool to determine the amplification factor (3) and the charge conversion factor for this specific pulse shape. The gas gain of the reference readout system (2) can be calculated with this information. Finally, the number of created photoelectrons in process (1) is obtained by comparison of the laser signals with the previous measurements.

The wires of the reference readout system have a spacing of only 0.6 cm and the laser electron signals induce signals on the neighboring wires that interfere with the other signals. This needs to be taken into account during analysis to receive valuable results for the measurements. An analysis method that compensates theses effects will be presented.

4.1. ^{55}Fe Source Calibration of the Redundant Readout System

Knowing the number of electrons created by the laser is important for any measurement with this test chamber. Also energy and postion of the electrons have to be known very precisely, because they are the measuring tool in this type of test setup. A reference measurement with a precisely known number of initial electrons from a source can help to understand the laser photoelectron creation processes.

During the calibration measurement a ^{55}Fe source is placed inside the topmost board of the drift field stack, emitting radiation into the drift volume. The created primary charges drift towards the reference readout wires where they are detected. The trigger setup for this measurement is different from the laser measurements and the internal self-triggering option of the FADc is used, see also section 3.7.

The activity of the source is rather low. It has been bought in 1997 with an activity of 1,85 MBq and the current activity can be calculated being 33 kBeq. The diameter of the active source spot has been optically estimated to be about 0.3 mm to 0.5 mm.

^{55}Fe decays by electron capture into ^{55}Mn with a half lifetime of 2.737 years [35]. The X-ray energy spectrum of ^{55}Fe shows one line at 5.9 keV (28 % relative occurrence). Immediately after the electron capture, the missing electron in the K-shell is filled up by an electron from a higher shell. The resulting free energy is released from the atom by either the emission of an Auger-electron or x-rays. The atomic substructure of the ^{55}Fe-atom causes these X-rays to show up as three different lines in the spectrum that are too close together to be resolved by the wire chamber. Most of the remaining decays are directly via Auger electron emission with 5.1 keV (60 % relative occurrence), which are stopped immediately in the source window.

The X-rays of 5.9 keV react to a larger part via photoelectric effect (photon absorption, electron emission) with Ar_2 and CO_2. Figure 4.2(a) shows the relative and total cross sections of photons with carbon (atomic number 6), which is not too far from Argon (atomic number 18). The dominant effect is photon absorption, being about 100 times stronger than Compton scattering, and becomes even stronger for higher atomic numbers of the target material. So even for $ArCO_2$ as chamber gas it can be assumed that most of the initial X-rays convert to electrons.

Before they are absorbed by photoelectric effect, the x-ray photons of 5.9 keV travel a certain distance through the medium. Gamma ray absorption is a statistical process and the photons have an average attenuation length, μ:

$$I \; = \; I_0 \cdot \mathrm{e}^{-\mu t} \; = \; I_0 \cdot \mathrm{e}^{\frac{-t\rho}{\lambda}} \qquad \text{with} \qquad \lambda = \frac{1}{\mu/\rho}, \tag{4.1}$$

where t is the thickness the radiation travels through the medium of density ρ and λ is the photon mass absorption length, also known as the mean free path. In figure 4.2(b) λ as a function of the photon energy is shown for different materials. The gas mixture used in the test chamber contains 93 % argon. For an estimation of the attenuation process it is sufficient to calculate the attenuation length for pure argon. From the graph in figure 4.2(a) the value of λ for a photon

(a) Cross sections [3].

(b) Photon mass absorption length [36].
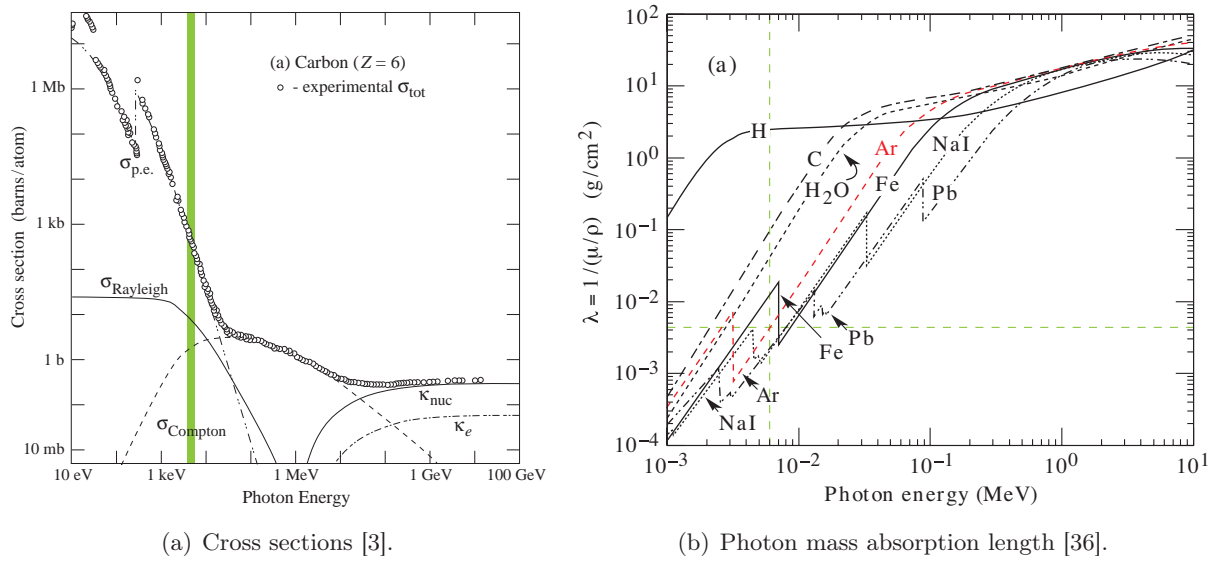
Figure 4.2.: Photon interaction with matter: Cross sections for the photon interaction with light matter (Z=6) (left) and Photon mass absorption length of photons for different target materials (right).

energy of $E_\gamma = 6\,\text{keV}$ can be obtained:

$$\lambda = 4.3 \times 10^{-3} \frac{\text{g}}{\text{cm}^2} \qquad \rightarrow \qquad \mu = \frac{\rho}{\lambda} = 4.2\,\text{cm}^{-1}. \qquad (4.2)$$

To gain knowledge about the position of the electron creation it is possible to calculate the distance where the probability is 95 %, for example, that the photon has already been absorbed. Also, for a certain distance one can give a percentage of the absorbed photons. This is interesting for the distribution of the locations of the electron creation. The radial distance around the source where, statistically, 95 % of the photons have converted to electrons via photoelectric effect, is 0.71 cm, while after 2 mm already more than 50 % have been absorbed and converted into electrons.

To get an overview about the setup and the distances inside the chamber, figure 4.3 shows a scaled drawing. The source is embedded in the topmost board and emits x-rays into the chamber volume. The two wires directly vertical under the source both register the drifting electrons, because the source is positioned exactly between them in horizontal direction. The wire strips cannot be removed easily and have been kept inside the volume. Their positions are partially in the path of drifting electrons emitted by the source. Due to the different heights of the strips, the resulting opening angle for the left and the right wire are not identical (8 degrees to 20 degrees) and also a part of the photons sent in the grey areas scan reach the wires, because a part of these photons converts to electrons already close to the source and is not or only partially hindered by the strips. The electrons that are created in the photoelectric processes will interact with the
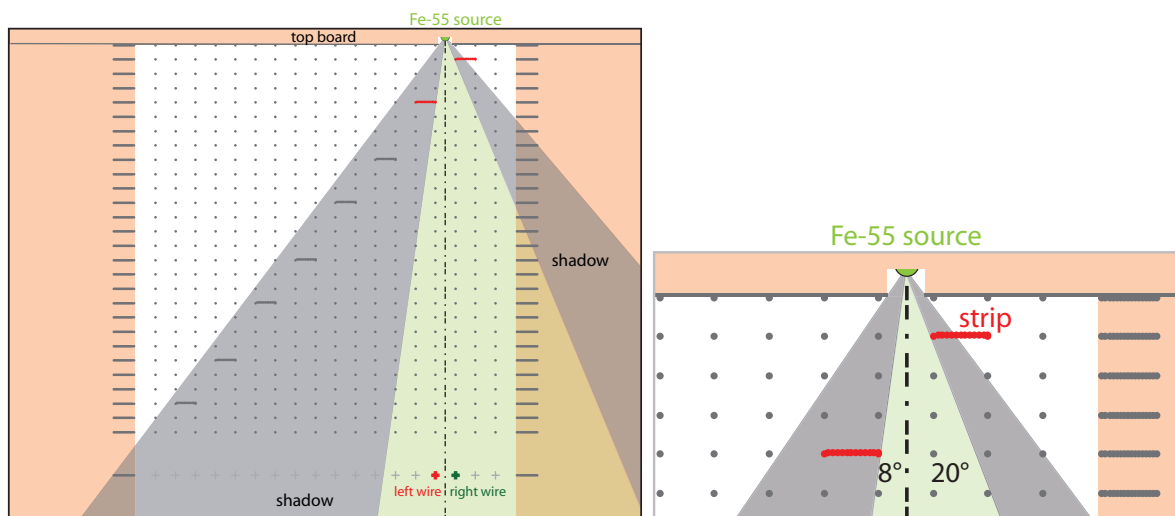
Figure 4.3.: The setup for the ^{55}Fe source calibration of the reference readout. The darker areas are the angles, where an emitted photon could produce an electron that might not be detected by the wires due to the geometry of the chamber and the aluminum strips inside the drift volume.

$ArCO_2$ according to the Bethe-Bloch formula, like presented in chapter 2.1.2. The range of the electrons is very small, they get stopped shortly after creation. The average range is given by

$$\bar{R}(E_0) = \int\limits_{E_O}^{0} -\frac{\mathrm{d}x}{\mathrm{d}E}\,\mathrm{d}E, \tag{4.3}$$

with $\frac{\mathrm{d}x}{\mathrm{d}E}$ being the inverse of the stopping power $S(E) = \frac{\mathrm{d}E}{\mathrm{d}x}$. The stopping power of electrons in gas is strongly dependent on the energy E and usually increases with decreasing photon energy. For $ArCO_2$ at 298 K (25°C) and 1.1 bar, the stopping power for 5.9 keV electrons is 0.38 MeV cm^{-1} [37], and for 1 keV electrons this has already increased to 1.1 MeV cm^{-1} [37]. Instead of integrating, one can also do a rough upper limit estimation for the range of the source by just using the smaller stopping power for the 5.9 keV electrons. This gives a upper limit of $\bar{R}(5.9\,\mathrm{keV}) \leq 0.016$ cm for the electron ionization track, which can be assumed to be a point-like electron cluster. Since the electrons are fully stopped, all of their energy is used up and converted into ionization. The average energy to ionize an argon atom is 26 eV [19], which corresponds to an average number of about 227 primary electrons for the 5.9 keV line. This cluster of electrons drifts towards the wires and will create secondary ionization in the gas amplification processes near the positive wires.

Results
The source has been measured with different wire voltages to determine the gain of the reference readout between 2600 V and 2875 V wire potential. Results for a voltage of 2800 V are shown
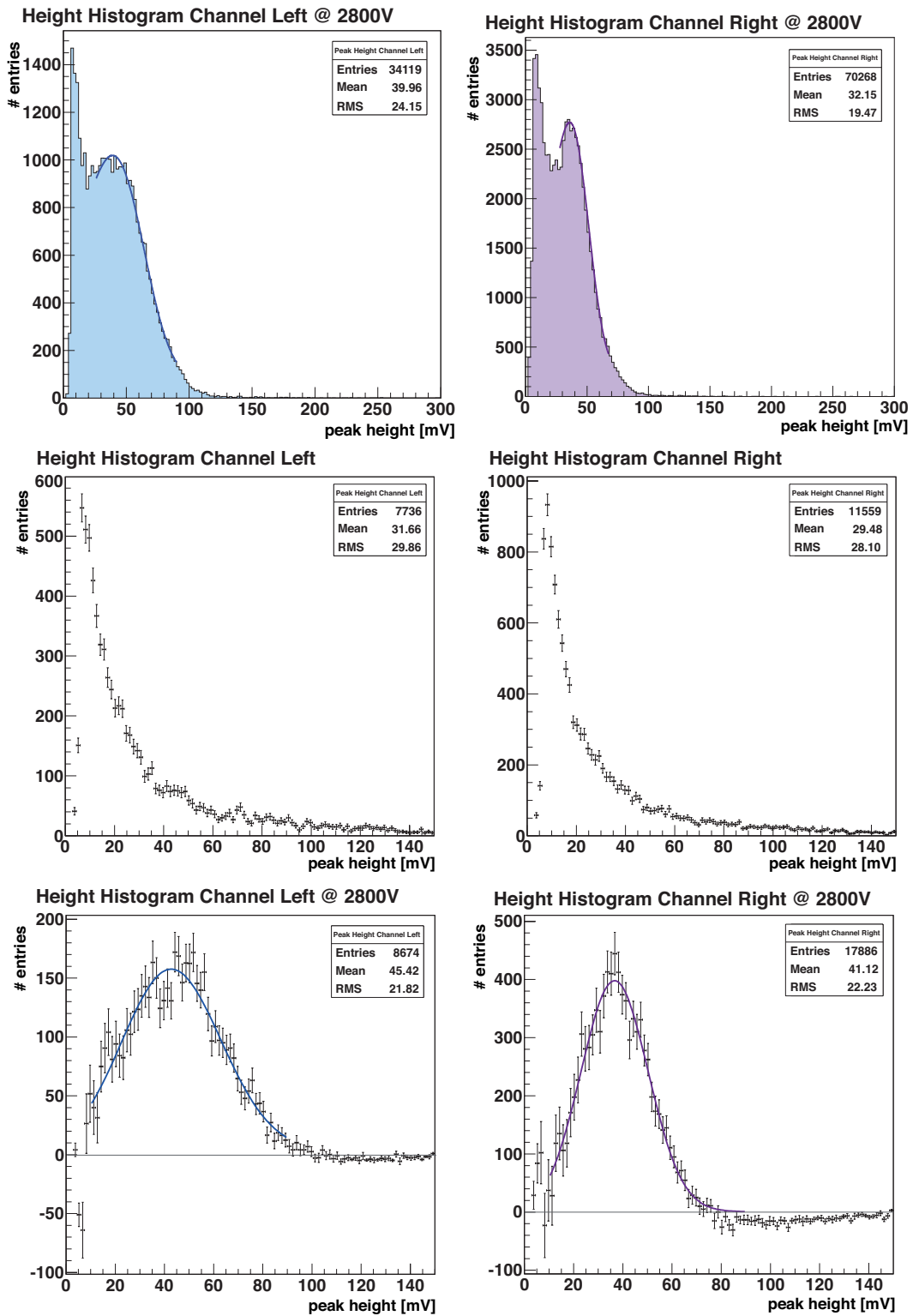
Figure 4.4.: Results of the ^{55}Fe source calibration: Full measured spectrum, background and spectrum with subtracted background and fit for both wires of the source measurement.
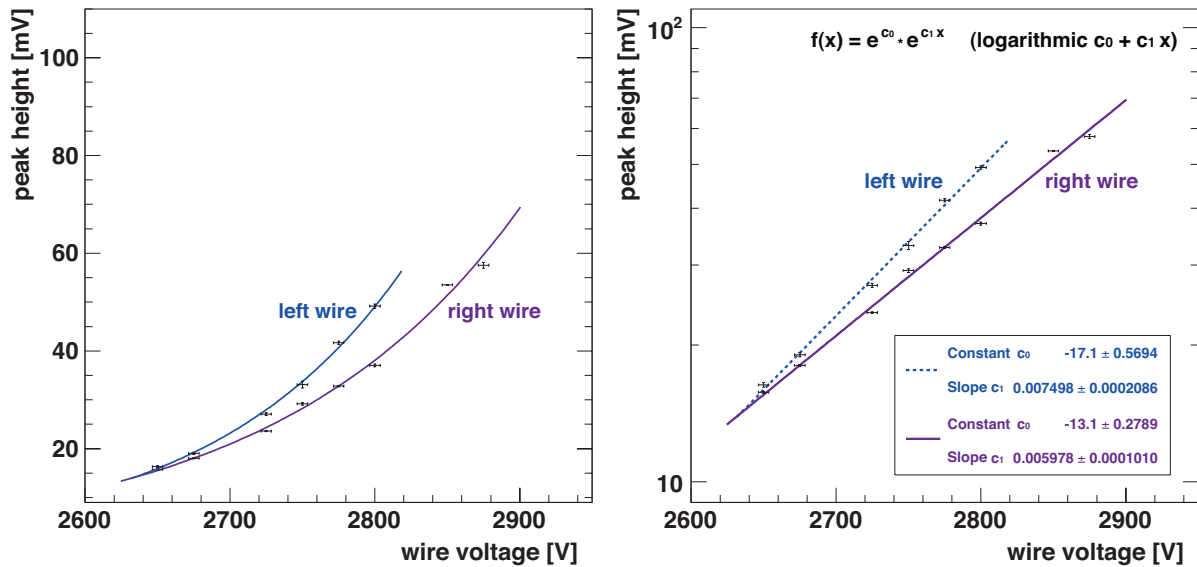
Figure 4.5.: Results of the source calibration measurement in a linear (left) and a logarithmic diagram (right). The behavior of the gain with the amplification voltage on the anodes is exponential. The differences between both wires are explainable by multiple effects, most of which are caused by the asymmetric strip positions inside the drift volume.

in figure 4.4. The peak height of the amplified signal is shown versus the number of events. Because of the necessary very loose trigger filter, a background noise peak is visible in the low signal height areas. It is explainable by the usual white noise. Background and signal peak are clearly distinguishable in this spectrum, that was taken in the upper mid of the amplification voltage range. It is possible to do a fit for this spectrum without background subtraction, but for the lower amplifications both peaks are overlapping even more. To remove the background, a separate background measurement under the same circumstances but without source for each wire voltage has been carried out. The shape of the background spectra has been determined and used to remove the background from the source spectra.

The background spectra for the 2800 V measurement and the source spectra after background subtraction are also shown in figure 4.4. The source peaks have been fit with a convolution of a Landau and a Gauss peak. The shape of the peaks is determined by several factors. The natural energy width of the source with its three close lines at 5.9 keV is unavoidable. Additionally the created charge from the avalanche processes fluctuates with a Polya distribution (see section 2.1.3).

The results of all pulse height measurements with different wire potentials are shown in figure 4.5. The exponential fit matches the data well, which is also clearly visible in the logarithmic plot. The errors in the plots arise from the errors of the fitted background subtracted spectra for

Table 4.1.: Results of the analysis of the ^{55}Fe source calibration measurement. The lower limit voltage gives the minimum wire potential that is necessary to distinguish background and signal and perform a background subtraction.

wire	c_0	error c_0	c_1	error c_1	lower limit [V]
left	17.1	0.57	0.0075	0.0002	2600
right	13.1	0.28	0.0060	0.0001	2600

each individual wire voltage.

The fit function is $f(x) = e^{c_0} \cdot e^{c_1 \cdot x}$. The fit results are shown in table 4.1. The difference in the exponential parameter c_1 is about 20 %, which is not negligible and can be explained as a coincidence of the error factors described in detail below. Since the factors are influencing the measurement for both wires, it is not reasonable to favor one of the measurements without complete and detailed knowledge of the impact of all error sources. A mean of both wire measurements gives the best approximation for the source measurement gain:

$$U_{amp}^{out} = \exp\left(15.1 \pm 2.0\right)\,\mathrm{mV} \cdot \exp\left\{(0.0067 \pm 0.0008)\,\mathrm{V}^{-1} \cdot U_{wire}\right\} \tag{4.4}$$

The fluctuations of the created charge inside the avalanche processes only increase the width, but do not change the mean peak position of the distribution. However, the structures inside the chamber may hinder some of the charge clusters completely or even only partially to reach the wires, which can shift the mean of the distribution. This effect may occur, if an electron cluster partially hits a strip on its way down or if the cluster is created in the short tunnel (about 1 mm) leading into the chamber volume, where no electric field is and attach to surfaces or get partially delayed. Because of the different heights of the strips inside the drift room, the symmetry between both wire results is broken too. The most obvious difference are the absolute count numbers. Both sets of measurements have been measured for the same total time, but after removal of the background, about a factor of 2.1 more events have been registered on the right wire than on the left one. This is explainable by the different opening angles, which have a relation of 20 degrees to 8 degrees, which results in a factor 2.5, which is comparable taking into account the additional electron clusters from the shadow areas that reach the wires. The positions of the peak maxima are slightly different (left wire: $(45.4 \pm 0.9)\,\mathrm{mV}$, right wire: $(41 \pm 0.5)\,\mathrm{mV}$), which can partially be explained by the amplifier calibration (about 1 % difference), but to a larger extent is the result of the different strip positions. Also the width of the peak of the wire, where the strip interferes more with the electron clusters, is larger.

Another factor that can have an influence on the spectrum are the different gains at different income angles around the wires. Since the field around the wires in this MWPC setup is not perfectly concentric, but more of an oval shape (see figure 3.14(a)), the gain is not exactly the same for different income angles of the clusters. The setup is the same as in figure 2.6 with a

coordinate system (x, y, z)[1]. The electric field for the region $x, y \ll s$, with s being the distance between two wires of the MWPC, is given by [38]

$$E = \frac{2C^*V_a}{r} \left\{ 1 - \frac{1}{3} \frac{\pi r^2}{s} \cos(2\alpha) \right\},\tag{4.5}$$

with $\tan(\alpha) = y/x$, C^* the capacity per unit length of the wire and V_a the wire potential.

The gas gain has also a strong dependency on the charge per unit length $Q = C^*V_a$, if the anode voltage V_a exceeds the threshold voltage V_T, where charge amplification starts [14]:

$$M = K \cdot \exp\left\{ C^* V_a \right\}, \qquad K = \text{const.}\tag{4.6}$$

The capacity of the single wires in this setup has been measured and the results show differences between the single wires of up to $5\,\%$ in capacity, which can result in large differences in the gain M.

At last, the source position could only be determined with an error of about $0.5\,\text{mm}$. Also a just slightly asymmetric source position could cause different count rates.

Together all these factors make it difficult to account for a single one of them and try to remove it. To fully exclude any large influence from the amplifiers, a laser pulse spectrum has been recorded directly after the source measurement and it showed a good performance of both of the amplifiers. The differences in the wire spectra clearly are caused by the chamber geometry, because switching the amplifiers (and with them the FADC channels) results in nearly identical spectra. Since the difference in the peak positions is about $10\,\%$ or less, and the effects are consistent for different readout voltages, it is still possible to get an exponential relation for the wire gain.

The large errors in this measurement and the multiple sources of errors show that the technical limits of this experiment setup related to the reference wire gain determination have been reached.

4.1.1. Calculating the Theroretical Response of the Redundant Readout System

It is possible to calculate the potentials, electric fields and time constants and with those the signal wave form of a wire tube and also of MWPC with induced charge distributions as E. Mathieson published in 1990 in *Induced Charge Distributions in Proportional Counters* [38]. The basic formulas that are needed to describe the reference readout of the MPGD test chamber as a MWPC are summarized and explained in appendix A.1, closely following Mathiesons work and terminology.

Applying the formulas to the geometry of the MWPC of the reference readout (figure 2.6), one finds a rather complicated formula for the electric field that has two simple limit cases: the very close anode area, where the electric field shape is mostly radial and the chamber body near the

---

[1]x in wire plane perpendicular to the wires, y perpendicular to the wire plane
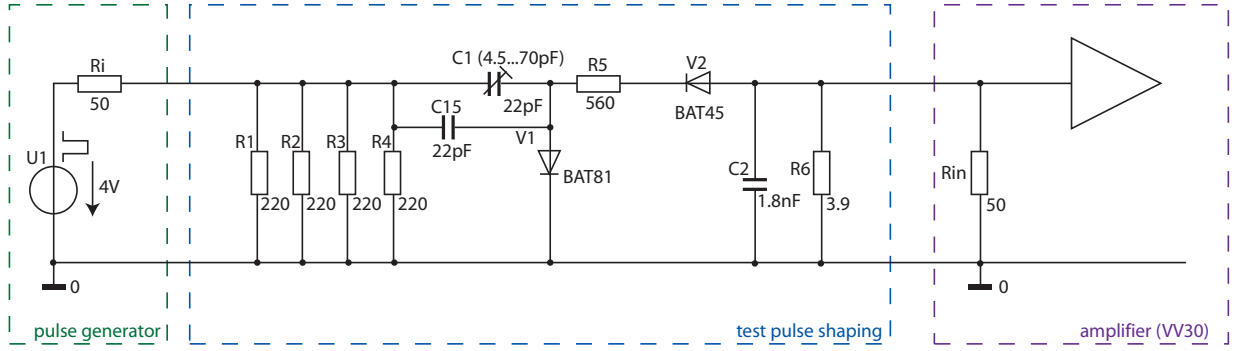
Figure 4.6.: Electrical scheme of the calibration pulse unit that imitates the wire pulses of the reference readout, courtesy of the Electronical Workshop, University of Freiburg.

cathodes, where it is mostly parallel:

$$
\begin{aligned}
\text{near anode}: \quad & x, y \ll s \quad & E = 2C^* V_a \frac{1}{r} \quad & \text{coaxial field} \\
\text{near cathode}: \quad & \cosh(2\pi h/s) \gg 1 \quad & E_x = 0, E_y = \pm 2\pi C^* V_a \frac{1}{s} \quad & \text{uniform field}
\end{aligned}
\tag{4.7}
$$

The dimensionless capacity C^* per unit length for this geometry is in numbers

$$
C^* = 1/\ln \left(\frac{r_c}{r_a} \right)^2 = (0.048 \pm 0.003),
\tag{4.8}
$$

with $r_c = \left(\frac{s}{2\pi} \right) e^{\pi h/s}$. This results in a value for the signal shape time constant t_0:

$$
t_0 = \frac{r_a^2}{4\mu C^* V_a} = (5.0 \pm 0.5)\,\text{ns}
\tag{4.9}
$$

The anode waveform caused by the ions, which are produced in the avalanche processes moving radially away from the wire, can be written as

$$
q_a(t) = -q_0\, C^* \ln \left(1 + \frac{t}{t_0} \right) = -q_0 \cdot (0.048 \pm 0.003) \cdot \ln \left(1 + \frac{t}{(5.0 \pm 0.5)\,\text{ns}} \right),
\tag{4.10}
$$

and the anode current is given by

$$
i_a = \frac{\mathrm{d}q_a(t)}{\mathrm{d}t} = -q_0 \cdot (0.048 \pm 0.003) \cdot \frac{1}{(5.0 \pm 0.5)\,\text{ns} + t}.
\tag{4.11}
$$

4.1.2. Calibration Pulse Unit

With the knowledge about the form and the time constant of the anode waveform of the reference readout, it is possible to determine the gain of the VV30 amplifiers. A calibration pulse unit
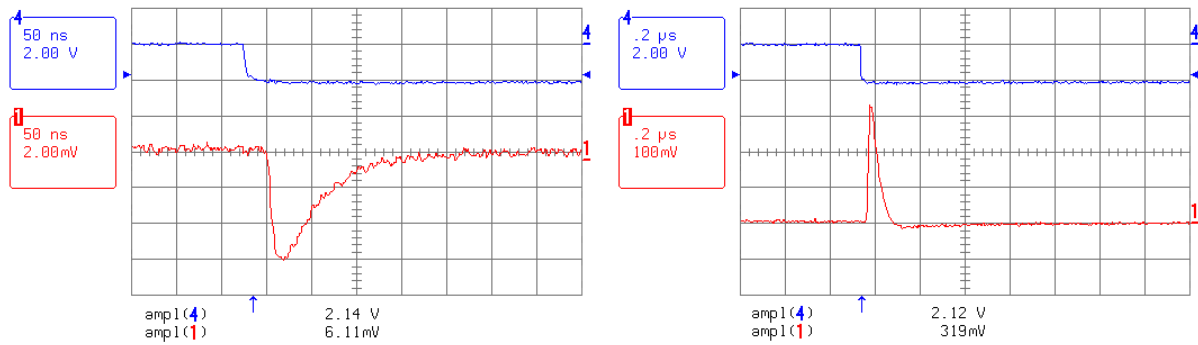
Figure 4.7.: The pulse shapes and typical heights of the calibration tool in and output: Left (4): The rectangular input pulse driving the calibration pulse unit, (1): output of the calibration pulse unit. The right picture shows the reaction of the VV30 amplifier to this calibration pulse (1).

has been designed and build that imitates the readout pulse. It was technically not possible to reconstruct the exact same shape as calculated in the previous section without the use of a function generator, but the result is sufficiently close to it and especially the time constants are correctly reproduced. The reaction of the VV30 is stable and the shape is as expected. The scheme of the test pulse unit can be seen in figure 4.6.

Because of the very small MWPC signals and the nominal amplification of a factor 48, it was necessary to use a voltage near the limit of the linear range of the amplifier which is given in the datasheet with $U_{max} = 350$ mV [39]. The input and output pulses of the calibration unit are shown in figure 4.7, as well as the typical response of the VV30 amplifier. Driven by a 2 V rectangular signal from a pulse generator unit, the output signal of the calibration pulse unit is a negative signal of about (6.1 ± 0.1) mV height. This is formed into a positive signal of about (318.6 ± 0.2) mV by the VV30 amplifier, which results in a mean amplification of $A = (51.5 \pm 0.8)$. The difference to the nominal amplification of 48 can be explained by a slightly different supply voltage of the amplifiers during the tests, since the amplification was shown to be very dependent on the supply voltage. Therefore the power supply in the experiment has been stabilized externally and is the same for all 34 amplifiers in the setup to avoid gain changes caused by voltage drifts.

4.2. Calibration of the VV30 Amplifiers

The amplifiers are electronic components that are well understood but their correct operation is very sensitive to measuring and calibration errors. The absolute signal height and the gain are dependent on different external factors, such as temperature effects or fluctuations in the power supply. It is important to use the amplifiers for the foreseen signal shapes and in their specific limits and to know about their statistical behavior. These aspects will be discussed in this section.
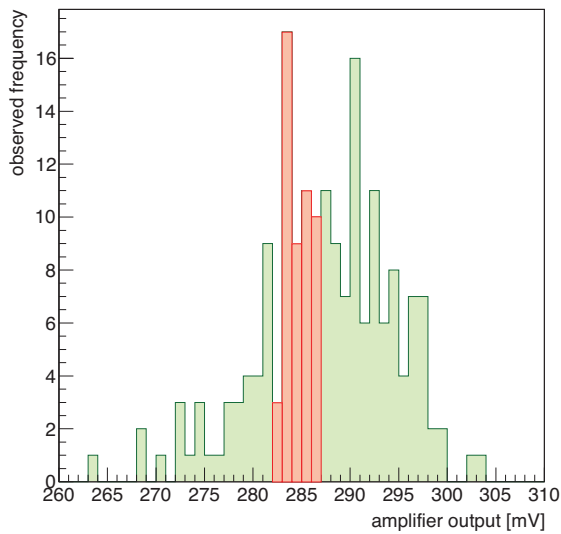
Figure 4.8.: The distribution of the amplification factors of the VV30 amplifiers concentrates around a value of $284.4\,\mathrm{mV}$, which is equivalent to a amplification factor of $A = 46.6 \pm 0.3$ for the amplifier setup.

4.2.1. Signal Height Calibration

The output signal height error of the VV30 amplifier is an important factor for the precision of the Micromegas measurements. Differences in the gain for the 34 used amplifiers severely influence the precision of the MPGD measurements and therefore need to be compensated during analysis for each channel individually. The chosen analog VV30 amplifiers have been used in a different experiment before and are already about 20 years old, but the functionality has been tested and is still without defects. They are also available in large numbers and easily replaceable if necessary.

A pole-zero cancellation network that improves the output pulse shape is part of the VV30 amplifiers. The possibilities to adjust the absolute amplifier gain without affecting the previously calibrated pole-zero cancellation network are very limited. Therefore 186 amplifiers have been tested to find a set of 34 amplifiers with characteristics as similar as possible and choose these for the installation into the MPGD test chamber.

The calibration pulse unit described in section 4.1.2 is used to determine these differences in the amplification factors of the amplifiers. Due to the special experiment setup and the limited options to change the cabling, connectors and mechanics of the chamber without large efforts for such a high number of units, the amplifier calibration is performed with a separate setup. The exact supply voltage, as well as temperature effects, are different for this setup and will inevitably lead to different absolute gain results. These effects are linear and compensable by a comparative measurement with the chosen amplifiers under both conditions. The relative gain results are still precise and useful for the choice of 34 similar calibrated amplifiers with good performance.

The measurement setup for this test consists of a stable power supply for the amplifiers, the test pulse unit driven by a pulse generator and a digital oscilloscope as a readout. It records the pulse heights and immediately calculates the average values. The average values stabilize already
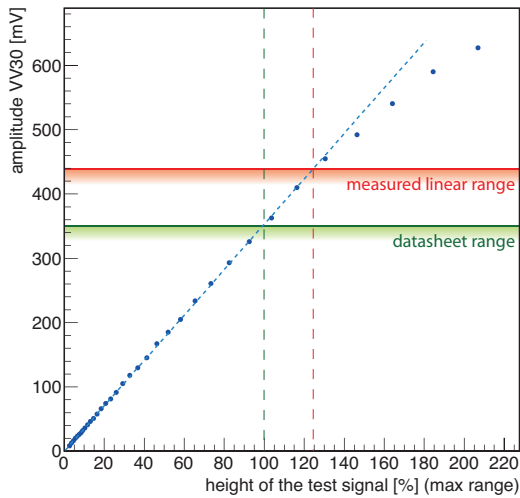
Figure 4.9.: Linearity measurement of the analog amplifiers of the type VV30. The linear range in the measurement exceeds the range given in the datasheet by about 100 mV, which gives extra safety margin and allows to use the whole range up to the nominal linearity limit. The errors are small and the error bars are hidden by the data points.

after about 300 to 500 sweeps, but the measurements are all taken at about 1000 to 2000 sweeps to get better statistics and to keep the errors smaller. Due to warm-up effects for the amplifiers, the time for the acquisition of the sweeps must be limited to about 30 to 60 seconds.

The results of the measurements are shown in figure 4.8. The distribution of the measured gain factors for the 186 different VV30 amplifiers shows a larger number of amplifiers with a gain around the mean value of 284.4 mV, which is equivalent to an amplification factor of $A = 46.6 \pm 0.3$. The units with amplification factors between 46.3 and 46.9 have been selected, which are 41 units. 34 of these have been chosen randomly for installation into the experiment, the remaining units are stored as replacements in the case of a damaged amplifier. The chosen units with their measured values and the relative correction factors that are used to compensate for the slightly different gains in the analysis are given in the appendix in table B.1 and table B.2. To get the absolute amplification value in the experimental setup, the gain values must be multiplied by the calibration factor obtained by a comparative measurement for three random samples of the used set of units. In the setup, conditions as temperature and supply voltages are different and the gain has been measured to be 46.9 ± 0.3. The additional calibration factor is therefore (1.006 ± 0.001).

4.2.2. Linear Range of the Amplifiers

The datasheet of the VV30 guarantees a linear range of the amplifiers with 0 to 350 mV, although the actual linear range of the devices extends above these values. To measure the full curve, the calibration pulse unit cannot be used, since the output pulse is fixed at about 80 % of the linearity range. A function generator with 1 ns sampling in combination with an analog attenuator is used to measure the set of data in figure 4.9 for a random VV30 sample. A digital oscilloscope records the data and automatically finds the mean peak height. The measured amplification is very constant up to 440 mV, which is better than predicted by the datasheet. Above this threshold,
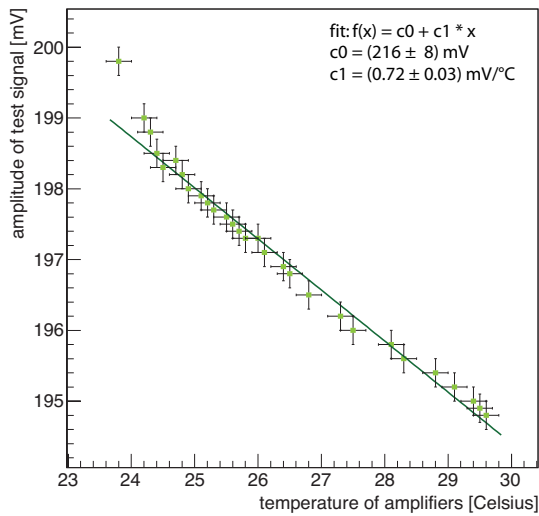
Figure 4.10.: The temperature dependence of the VV30 amplifiers shows a reasonably linear behavior for the range between room temperature and the temperature where the system stabilizes after about 20 minutes, which is around 27.5°C.

the measured voltage underestimates the theoretical value by only about 10 % up to an output voltage of 600 mV. To verify the results, 4 more random samples have been tested and all show similar behavior. Therefore the full linear range will be used in the experiment setup for standard mean signals and rare overshoots up to 440 mV will be accepted, too.

4.2.3. Temperature Dependence

The VV30 amplification factor is temperature dependent. The pulse height decreases with increasing temperature, which is especially visible shortly after activation of the amplifier power supply, since the heat development of the amplifiers is not negligible. The amplifiers are located in two boxes made of aluminum, 18 amplifiers for the reference readout in the first and 16 for the MPGD readout in the other box. Their purpose is mainly to provide shielding against any electromagnetic induced noise for the wire and chamber signals as well as to house the voltage stabilization of the power supply of the amplifiers. A warm up curve was measured with the help of a PT100 temperature sensor that has been installed in one of the boxes. This sensor is calibrated to have a resistivity of $100\,\Omega$ at $273.15\,K$ and to change it linearly with temperature. The absolute measuring errors of these devices are in the range of $0.2\,K$, while the relative statistical errors of a single device are usually smaller. After reaching stable conditions, the amplifiers were heated externally with a hot air fan.

The measured curve covers the temperature range from 24°C up to 30°C. The laser pulses have been used as calibration pulses and the measured VV30 output pulse heights are an average of about 1000 events, taken with the averaging function of an oscilloscope. The curve is shown in figure 4.10. A linear context can be found for most of the covered range, the fit delivers a temperature slope of about $(0.72 \pm 0.03)\,\mathrm{mV\,K^{-1}}$ for a mean pulse height of 196 mV, which is about 0.36 % per degree Celsius. This change is negligible for stable temperature conditions, but the warm up period needs to be skipped for any quantitative measurement. The air conditioning
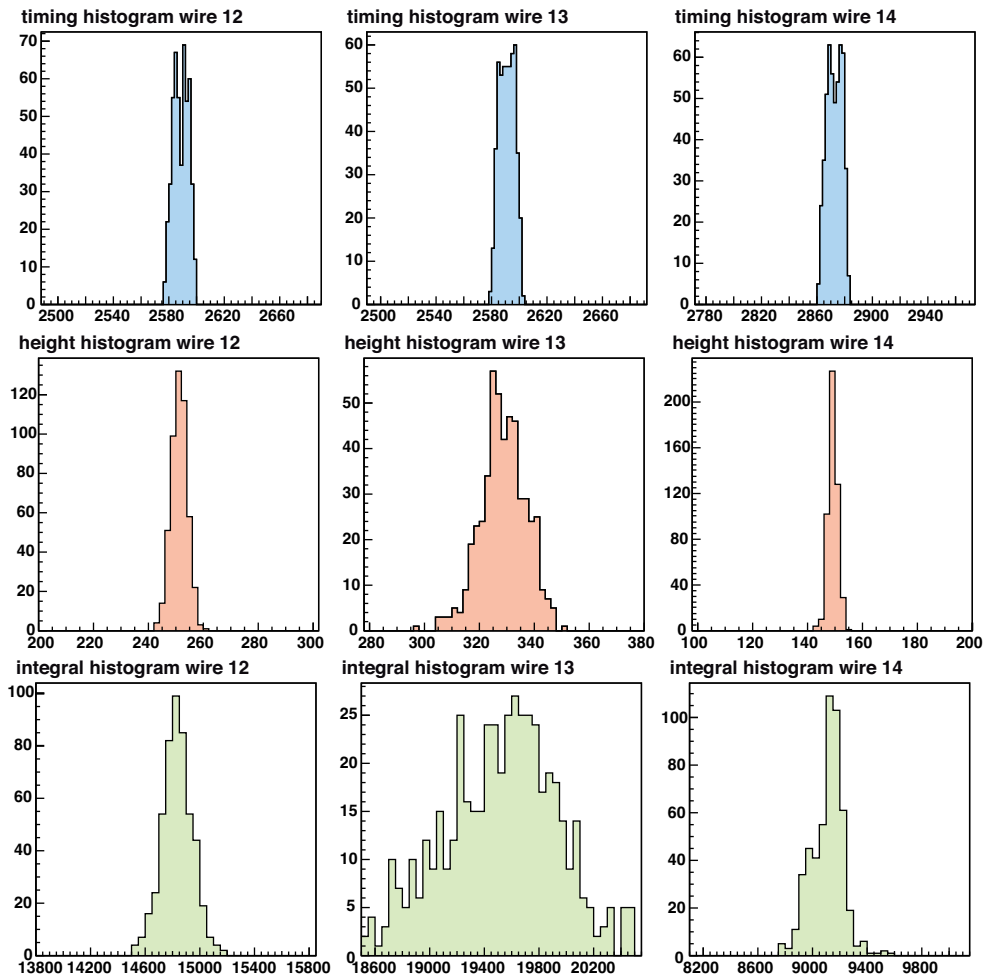
Figure 4.11.: The wire distributions in timing, pulse height and pulse integral for different wire channels are a indicator to find partially defect amplifiers, which do not fulfill the requirements for energy and timing resolution of the pulses.

of the room must be stable at any point in time and the amplifier boxes must kept close at all times.

4.2.4. Signal and Laser Pulse Fluctuations

Small changes in the power supply of any electrical component of the readout chain, the heat up cycle of the laser and heat up times of the amplifiers cause measurable shifts of the signal pulse heights. These influences can be avoided or reduced by stabilizing the system with voltage regulators and temperature control systems or simply by avoiding heat up cycles during measurements. Other gain variations are more of a statistical origin like for example laser intensity
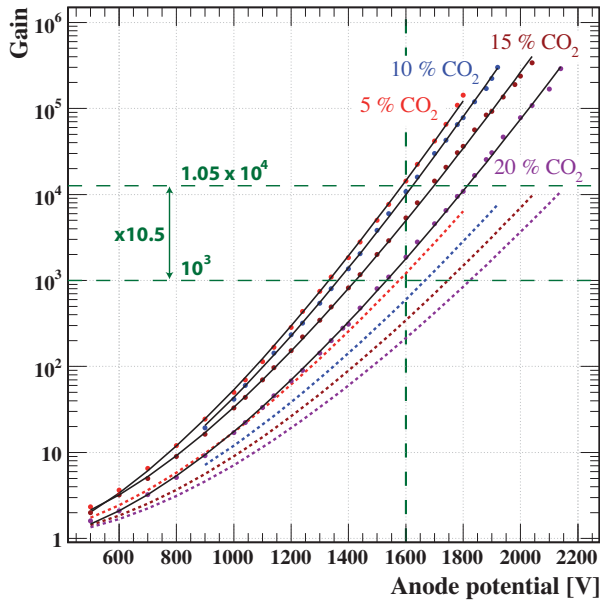
Figure 4.12.: The Penning effect in $ArCO_2$ has been measured and computed for different CO_2 contents. Differences between the calculated gains without considering of transfer mechanisms (dashed curves) and the measured data can be more than one order of magnitude (Picture from [40] with data from [41]).

fluctuations, the usual variance of the statistical processes for the electron creation on the strips and the statistical gain fluctuations caused by different avalanche sizes at the wire anodes. They cannot be avoided and play a role in the measurement errors.

Also the gains of the amplifiers show a statistical behavior and variations from device to device, due to the analog characteristics of the amplifier electronics. The chosen amplifiers have been in use in a former experiment where they have all been tested and calibrated, but since then aging effects may have appeared for single units.

The use of the laser with its high repetition rates and its good reproducibility of the pulses allows for high statistics in each measurement with the reference readout system. During the analysis, histograms concerning pulse height, pulse integral and timing are generated for each wire. Figure 5.5 presents as an example these histograms for three wires. The center wire (wire and amplifier 13) shows unusually high gain fluctuations, visible in the broad height distribution and also in the abnormal signal shapes which are reflected as high variances in the integral histogram. The timing histogram instead is comparable to the others and acceptable. All amplifiers with deviations in the spectra were replaced. The diagrams are saved for every reference readout analysis for further inspection on analysis.

To account for the normal and unavoidable gain fluctuations in the analysis, the distributions are fit to get the mean values. Their widths are reflected in the error analysis of the measurements.

4.3. Simulation of the Gain and Comparison to ATLAS MDTs Gas Gains

To get a quantitative crosscheck for the achieved gains in the simulation done in chapter 3.6 and to be able to compare the results with known and already working setups, the geometry of the ATLAS MDTs has been simulated using the same program version and settings as for the chamber simulation. Setup, working principle and description of the ATLAS MDTs can be found in section 2.1.1. The MDTs are using the same gas composition ($ArCO_2$ in parts of $93\,\%/7\,\%$), but a higher pressure of about 3 bar absolute pressure, while the MPGD chamber pressure is only around 1.1 bar.

During simulation, electrons are created at random locations in the drift tube and tracked to the wire in the center of the tube, where the amplification process takes place. In this simulation with the correct gas composition, the achieved gain was simulated to be around 2000, but the real gain for the ATLAS MDTs has been measured to be around 20000 [18]. This difference of a factor 10 is explainable by the Penning Effect (see also section 2.3.4), which is not accounted for in the basic Garfield (version 9) simulation, but must be included explicitly by the user. This basic implementation of the Penning Effect can simply be added to the simulation, but it does not provide all necessary parameters. Some of these do not exist in literature for this specific gas composition. Additionally, the inclusion of this effect slows the simulation down dramatically. Therefore to get an estimation of the impact of the Penning Effect, only the ATLAS MDT simulation, which is simpler compared to the MWPC simulation and takes less computing time, was repeated with the basic version of the Penning Effect simulation. The gain increased by a factor of about 4 to a value of around 8000, which is still about a factor of 2.5 away from the measured value of 20000, because the full effect cannot be included.

An estimation for the impact of the Penning Effect can be made using a study by Şahin et al. [40], where measured gas gains for $ArCO_2$ are compared with calculated gains not including any transfer processes that are responsible for the gain increase. Their results can be found in figure 4.12.

The drift tube used for the measurements is a square tube with cathode dimensions of $1.1 \times 1.6\,cm^2$ and a wire diameter of $50\,\mu m$, with a pressure of $1070\,hPa$ and $20°$ Celsius. In the region close to the wire the field is the same as for a round tube with radius $r = 0.67\,cm$. Now the dimensionless capacity C^* can be calculated to be $C^* = 0.089$ (details in appendix A.1.2).

The electric fields are not equal to those in the reference readout MWPC, but via the expression $E/r = 2C^*V_a$ (explanation in appendix A.1.3 and [38]), which is valid in the close wire proximity where the gas amplification processes take place, both geometries can be compared. The potential V_a that needed to be applied to the square tube in the paper of Şahin et al., resulting in a comparable electric field in the wire region as for the test chamber simulation, can be calculated:

$$C^*V_a = C^*(\text{sim})V_a(\text{sim}) \qquad \rightarrow \qquad V_a \approx 1600\,\text{V}, \tag{4.12}$$

with $C^*(\text{sim}) = 0.048 \pm 0.003$ and $V_a(sim) \approx 3000\,\text{V}$. The curves in figure 4.12 reflect measure-

ments for 5% and 10% CO_2, but the simulation was done for the used gas composition of 93% Ar and 7% CO_2. The other conditions like pressure and temperature are directly comparable. Annotations as green dashed lines in the figure show the gain values for a potential of about $1600\,V$ and a very rough interpolation between the two curves for 5% and 10% CO_2 content. The increase in gain is about a factor of 10.5, which is consistent with the estimation achieved from the comparison between the simulation and the ATLAS MDTs.

Therefore the simulated gains from chapter 3.6 underestimate the gains of the chamber by a factor of about 10. The corrected gain of the chosen working point for the reference readout is around 10^4, which is comparable to the gain of the ATLAS MDTs.

4.4. Reference Readout Analysis

The correct analysis of the reference readout wire signals is important for the further analysis and for any quantitative reference measurement that can be done with this setup. After all correction steps and calibrations have been applied, the signals that were recorded by the FADC still need to be corrected for the unavoidable induction effects that reduce the real peak height by up to 25%, which cannot be ignored. This effect arises from the close wire distances of only $6\,mm$ between two neighboring wires and can be detected up to two wires apart from the main signal wire.

Figure 4.13 illustrates the details of the signal reduction effect due to overlapping induced signals. The electron cloud created at one of the aluminum strips above the reference readout drifts towards the wires. Near the wires each electron cloud splits up between two neighboring ('assigned') wires. The main positive peaks are caused by the charge inside the amplification
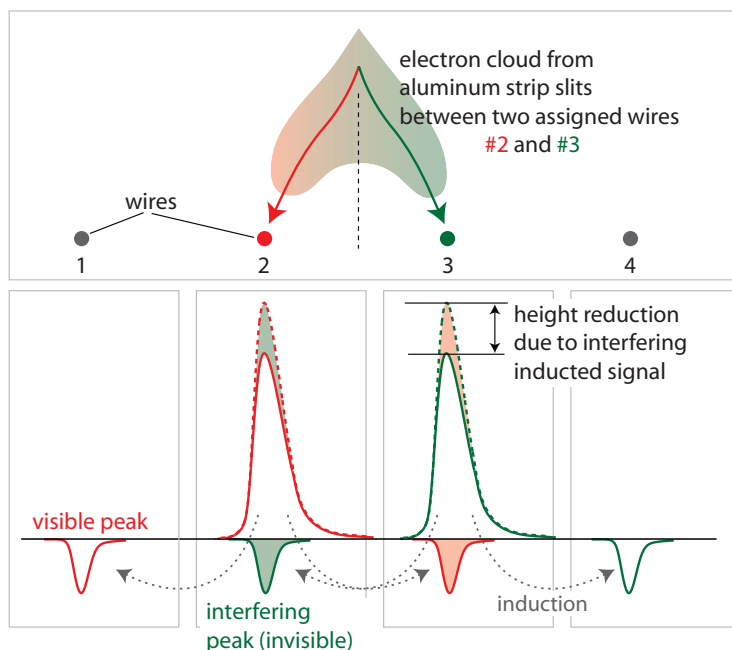
Figure 4.13.: Induction processes between the wires of the reference readout system with the height reduction due to the interference of the main peaks and the inducted signals. Only the induction on the next wire is shown for better clearness of picture, but inducted signals also appear on next-to-next wires.
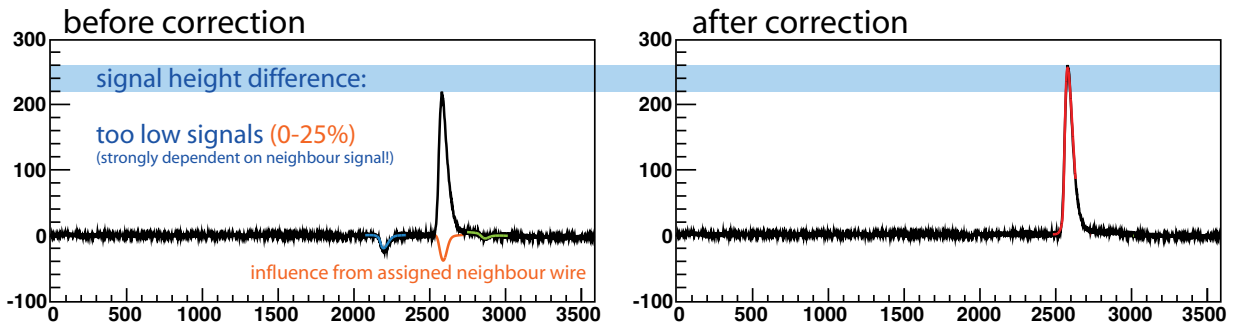
Figure 4.14.: Pulse height correction during reference readout analysis removes the negative induced peaks from the neighboring wires and restores correct pulse height of the main signal pulses.

avalanche near the respective wire. These positive pulses induce negative pulses on the wires near them. Most of the induced signals do not overlap with one of the main peaks, since they arrive on different times than the peaks caused by other electron clouds. Only signals from the same electron cloud interfere, and therefore the induced signal from wire 2 on wire 3 reduces the height of main peak 3 and vice versa in figure 4.13. The processes in the illustration are simplified, because in effect the induction processes affect also the next-to-next wires and the induced signals overlap among each other.

Figure 4.14 shows a typical record for one FADC channel for a wire measurement. Around the positive center pulse are two smaller negative pulses visible, which are induced pulses belonging to neighboring wires. The left negative pulse is higher than the right one and arrives earlier than the main pulse on the wire. It is therefore caused by an electron cluster arriving on the wire directly left of the observed wire, because the drift times are increasing from the left to the right side of the chamber with the used strip positioning. The pulse on the right is caused by a wire signal on the right of the observed wire and in a larger distance due to its comparatively low height. A third induced pulse can be reconstructed in this picture. It is not visible, since the main pulse and the induced pulse are overlapping. From the position of the induced pulse it can be concluded that it is simultaneous with the main pulse, therefore it is caused by the same electron cluster.

This invisible induced pulse from the associated wire reduces the pulse height of the main pulse by a large factor that is dependent on the pulse height on the associated wire and can reach up to 25 %. It is not possible to correct this pulse height reduction with a constant factor. Although the target strips are centered above the wires, the laser alignment is not perfectly centered on the strips in most cases and the amount of electrons arriving on both wires is often not symmetric. Overlapping peaks that are not absolutely coincident in time cause changes of the peak shape. Since the information on the charge of the electron cloud is in the height of the peaks, this needs to be strictly avoided.

Partial laser beams that might be blocked for some measurements will influence the appearance
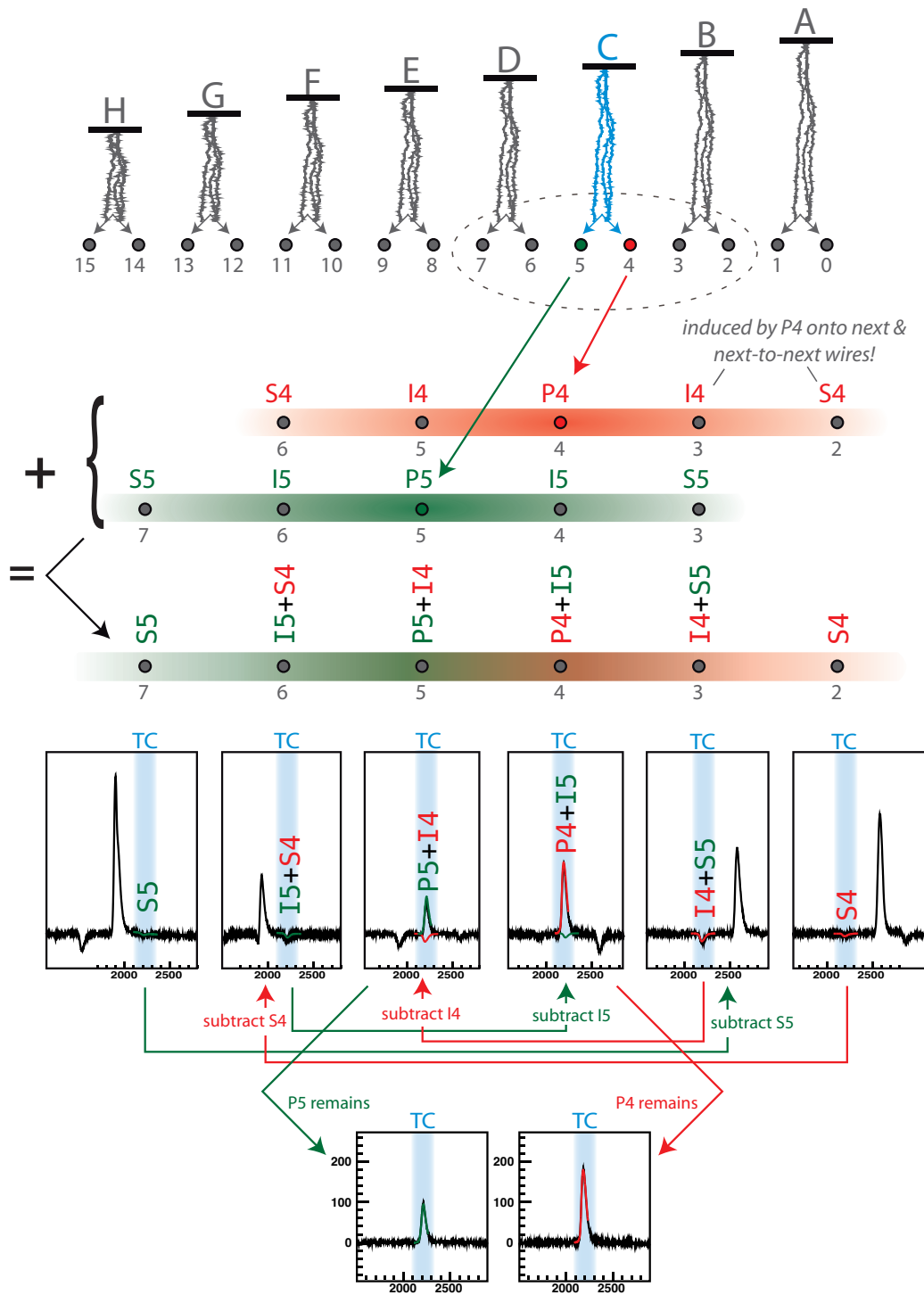
Figure 4.15.: The wire pulses analysis scheme: The main positive pulses induce negative pulses on the surrounding wires that interfere with the main peaks and need to be extracted by fitting and subtracting them from the spectra.

of the influenced peaks or remove them completely for different measurement setups.

It is possible with some analysis effort to remove these unwanted overlapping induced peaks, even if they are not directly visible in the spectrum. It is necessary to look at all FADC records simultaneously. Figure reffig:anascheme shows the basic principle of the analysis. The laser spot C is examined in detail as an example. The electron cloud drifts down towards the reference readout wires and the charge splits up in the electric fields around wires 5 (green) and 4 (red) and charge amplification sets in. The resulting pulses P_4 and P_5 on the respective wires are recorded by the FACD at the same time T_C, which is in this example around 2200 ns after the laser trigger.

The pulses P_4 and P_5, independently from each other, induce negative signals on the neighboring wires. For P_4 the effect reaches from wire 6 to wire 2, and for P_5 from wire 7 to wire 3. The pulses induced on the next wire are called I followed the number of the inducing signal, the induced signals on the next-to-next wire are labeled with S and a number. Since all of these signals have the same timing T_C, induced signals caused by both main signals P_4 and P_5 are superposed, added regardless if they are negative or positive.

This is the case for all 8 laser spots, but signals from different electron clouds and therefore different arrival times will not interfere with each other, since the width of the signals is less than the drift time difference between the electron clouds for all laser spots. Therefore, the small induced peaks S_5 on wire 7 and S_4 on wire 2 remain without any interferences.

To get the real height for the main peak P_4, it is necessary to know the signal I_5 that is invisibly superposed. The procedure is to go backwards: First S_4 on wire 2 is fit, the peak time is extracted, height and integral are determined. Then S_4 can be subtracted from the spectrum of wire 6 ($I_5 + S_4$), only the pulse I_5 will remain. This pulse can be fit and finally subtracted from the spectrum of wire 4 ($P_4 + I_5$), where the result is the main peak P_4.

This principle works for each wire, except the wires 0 and 15, because the the required peaks S_0 and S_{15} are missing, since the respective wires are on the side of the readout and only the middle 16 of the 18 wires are monitored by an FADC channel. For these two missing heights, the heights of the corresponding main peaks in relation to their first induced peaks are taken as a basis for an estimation. A larger error is added on these heights.

To visualize the overall procedure, one single event with all laser beams and records of all 16 wires (15 to 0) is shown in figure 4.17. An individual baseline correction for each FADC channel has already been performed in this picture. The timings of the eight electron clusters from the eight aluminum strips are marked and illustrate the relations between the different groups of signals. For each signal the contributions of the different neighboring signals are given.

To do the complete analysis automatically, a ROOT [34] program has been written. This rather complicated analysis of each event is possible, whenever the peaks reach heights above about 100 mV. Below this threshold, the induced signals cannot be separated from the white noise background since they are too small. The program also accounts automatically for missing signals and decides, based on the quality of the fits, whether an event can be used or rather is to be discarded. This might be necessary due to unexpected background arising from discharges or even cosmic rays.
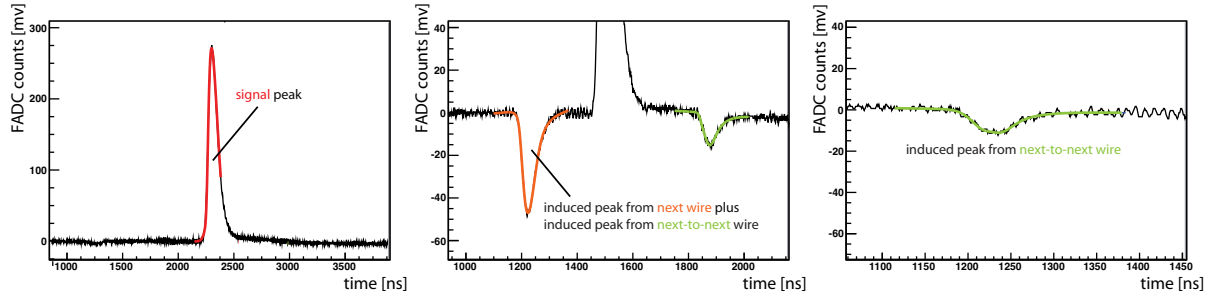
Figure 4.16.: Typical wire pulses with fits: Positive signal peaks and induced peaks of first and second order.

The shape of the signal peaks is mainly determined by the output pulse shaping logic of the VV30 amplifiers and does not reflect any physical effect of the particle detection. Therefore the fit function can be chosen freely. A Landau peak superposed with a Gaussian and a linear term suits best the shape of the peaks, also of the negative induced signals. Typical peak shapes and their fits can be found in figure 4.16.

The errors of the pulse analysis consist initially only of the errors of the FADC records but add up due to the fits and the removal procedure of the induced signals. They are reflected in the errors on time, height and integral of the analyzed peaks.

Due to the height correction of the main peaks the accurate charge of the signals can be determined by fitting the clean shape of the signals as visible in figure 4.14.

4.5. Conclusion

The characteristics of the VV30 amplifiers have been measured and are well understood. The linear range of the amplifier units is $(0 \text{ to } 350)\,\text{mV}$ for the mean of the pulse distributions, but up to $450\,\text{mV}$ for single pulses has been found to not lead to any loss of precision.

The voltage gain of the amplifiers under the special experiment conditions has been measured to be 46.9 ± 0.3 and is in good agreement with the specifications given in the datasheet.

The amplifiers are voltage amplifiers, but for a known signal waveform $U = U_0 \cdot 1/(t_0 + t)$ of the calibration unit, a charge conversion relation can be found. Therefore the charge deposit on the wire needs to be estimated. With $U_0 = (6.1 \pm 0.1)\,\text{mV}$ peak height and R the source resistance of the calibration unit, the charge of the calibration pulse unit can be estimated from the oscilloscope to be

$$Q = (8.0 \pm 0.5) \times 10^{-12}\,\text{C} = (5.0 \pm 0.3) \times 10^{7}\,\text{electrons}. \tag{4.13}$$

Because the gain of the amplifiers is measured to be $A = 46.9 \pm 0.3$, a conversion factor of $c_b = (0.82 \pm 0.05) \times 10^{7}\,\text{electrons/mV}$ peak height before the amplifier or $c_a = (1.7 \pm 0.1) \times 10^{5}$
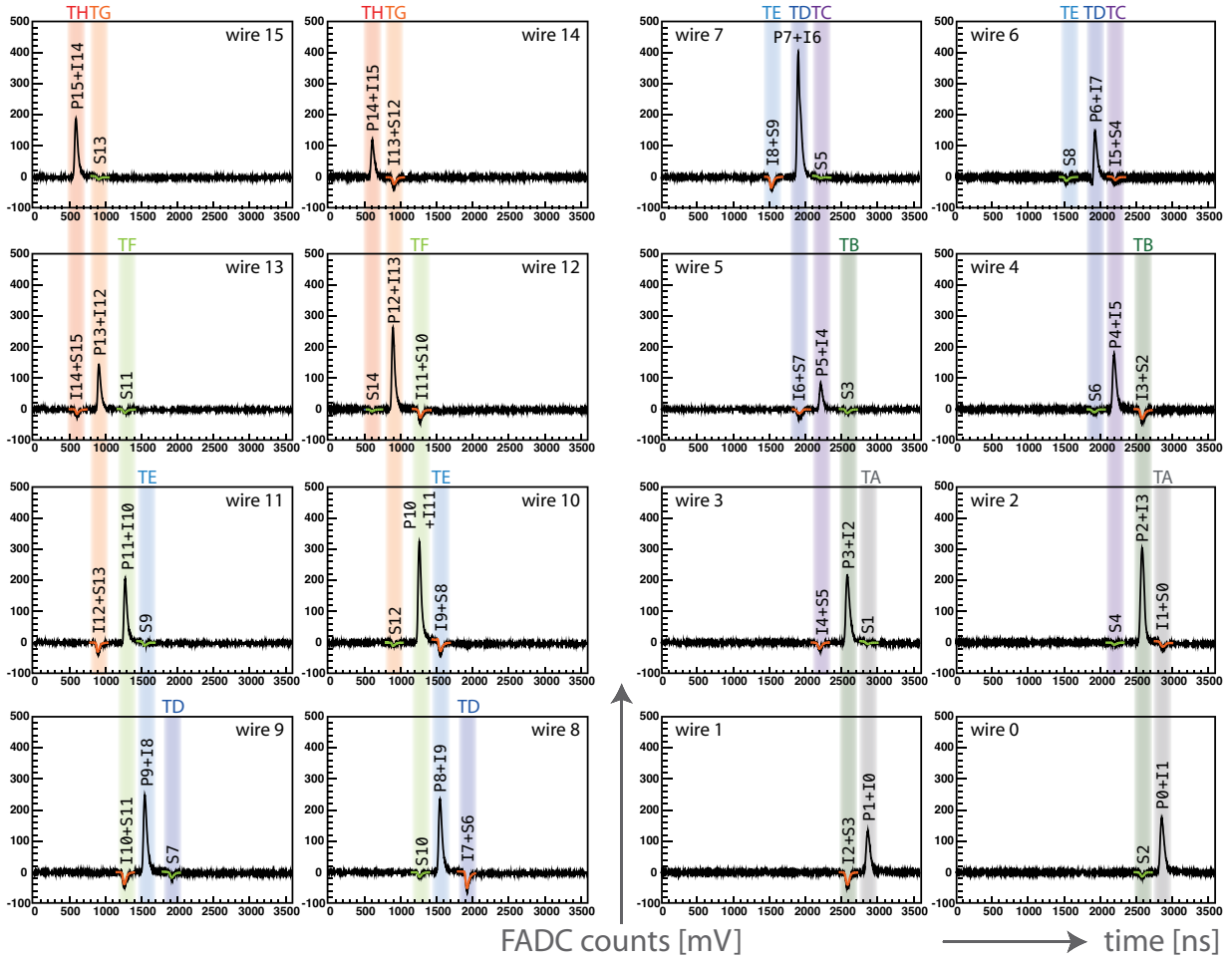
Figure 4.17.: An overview over a single laser photoelectron event recorded with the reference readout system. The different electron cluster timings (TH to TA) are marked and the influences of the surrounding wires are given. The induced peaks overlap partially with the main peaks, but they can be removed during analysis.

electrons/mV peak height after amplification can be defined. These are useful for the following calculations.

The measured source peaks of $U_a = (43.2 \pm 1.0)\,\mathrm{mV}$ average height at around 2800 V wire voltage are equivalent to a number of about

$$Q_b = \frac{U_a}{A} \cdot c_b = (7.5 \pm 0.5) \times 10^6 \tag{4.14}$$

electrons on the wire. This average number of electrons is produced in the avalanche, which has been started by a mean number of $Q_s \approx 227$ primary electrons. This leads to an estimation for

the wire gain at $2800\,\mathrm{V}$ wire potential at a temperature of $23°\mathrm{C}$ with standard power supply of

$$M = \frac{Q_b}{Q_s} \approx 33200 \pm 2300. \tag{4.15}$$

The output voltage of the VV30 amplifier per primary electron is therefore about $(0.190 \pm 0.004)\,\mathrm{mV}/e^-$, which can be understood as an average charge conversion factor (at $2800\,\mathrm{V}$ wire potential and standard conditions).

With this number it is possible to compare the laser intensity with the source measurement. To get photoelectron peaks of about $U_a^l = (300 \pm 20)\,\mathrm{mV}$ on both assigned wires at a comparably low wire voltage of $2560\,\mathrm{V}$, the attenuator in the laser beam is set to an angle of 341 ± 0.2 degrees, which translates into an attenuation factor of 0.535 ± 0.006. At this wire voltage, the source creates signals of $U_a^s = (10 \pm 1)\,\mathrm{mV}$. With this beam intensity, one partial laser (one eighths of the full beam intensity) therefore releases about

$$Q_l = \frac{Q_s}{U_a^s} \cdot 2\,U_a^l = 13600 \pm 1600 \tag{4.16}$$

electrons from one of the aluminum strips in the drift volume. The gain under these more normal conditions around a wire voltage of $2560\,\mathrm{mV}$ is about

$$M = 7700 \pm 1200 \tag{4.17}$$

The detection threshold for laser peaks is around $2\,\mathrm{mV}$. Even though this is still below the noise threshold, it is possible to measure these small peaks because their timing is precisely known and large statistics are available. This detection threshold corresponds to about 11 primary electrons at $2800\,\mathrm{V}$ wire voltage.

The drift space for the planned New Small Wheel Micromegas is $0.5\,\mathrm{cm}$ filled with $\mathrm{ArCO_2}$ at atmospheric pressure. For a minimal ionizing cosmic muon with an energy of about $350\,\mathrm{MeV}$ the average energy loss according to Bethe-Bloch in pure argon is approximately $1.05\,\mathrm{keV}$. This is equivalent to about 60 primary electrons, which is $\approx 26\,\%$ of the source signal.

5. Measurements and Results

This chapter presents the measurements that have been taken with the MPGD test chamber and their results. In general, the chamber is a multi-purpose test chamber and can be easily adapted to the study of a lot of different types of detectors like GEM or Micromegas.

To be able to do a first set of measurements with the MPGD test chamber, a test candidate detector has been designed and realized. With regard to the developments in the ATLAS high luminosity upgrade, the Micromegas technology has been chosen for the first test candidate detector.

The MPGD test chamber has been built to investigate the characteristics of gaseous detectors. Gain measurements with different readout geometries of the Micromegas test candidate are shown in section 5.2.

The large drift volume of the MPGD test chamber can also be used to carry out related measurements like drift velocity measurements and diffusion studies of electrons in gases that are independent from the Micromegas characteristics; those are shown in section 5.3.

Moreover, studies regarding the field geometry inside the amplification area of the Micromegas using an additional cathode layer are presented in section 5.4.

5.1. Micromegas Test Candidate

The Micromegas test candidate has been designed to fit the dimensions of the test chamber. The height-adjustable table of the chamber matches the standard-size GEMs of the CERN workshop, which is $(124 \times 124)\,\text{mm}^2$. The CERN workshop has also helped with the design and manufactured the test candidate.

Figure 5.1 shows a photo and a schematic view of the Micromegas test candidate design. The Micromegas consists of a PCB of 1.6 mm thickness and a thin metal mesh. In the outer regions, a ringlike area is used to hold the mesh under tension; the mesh covers the whole detector surface. It has a $65\,\mu\text{m}$ wire pitch and $20\,\mu\text{m}$ thick wires, woven and pressed flat. The inner part of the mesh has a distance of $128\,\mu\text{m}$ (P_H) to the board surface below it. Every $2\,\text{mm}$ (P_P) in both directions (x,y) a ceramic pillar supports the mesh mechanically without providing electrical contact to the board surface. Underneath the mesh, $35\,\mu\text{m}$ thick (S_H) copper strips on the PCB surface build the anode for the electron multiplication, that starts in the gap between mesh and board if the potential difference between anode (strips) and cathode (mesh) is above a certain threshold, which is about 400 V for this detector. The best operation voltage with good amplification, but only few discharges, is around 480 V to 500 V.
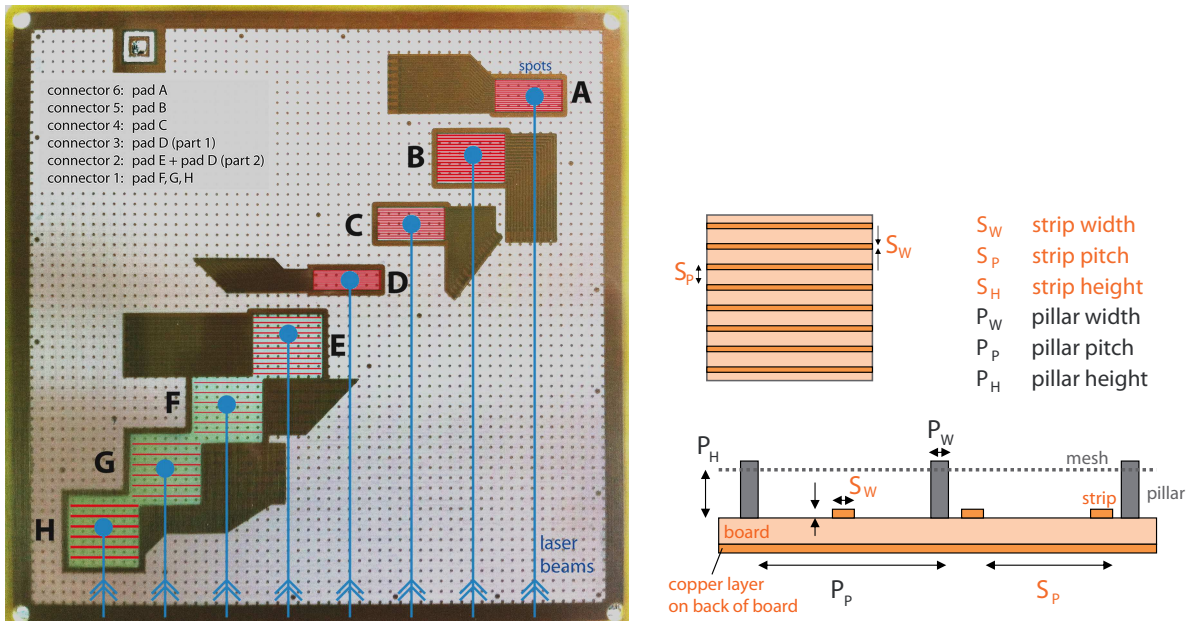
Figure 5.1.: The Micromegas test candidate has eight different sensitive hit zones, with different strip pitches S_P and strip widths S_W, see also table 5.1.

Although the whole detector surface is covered with the mesh, there are only a few sensitive areas on the board, where also anodes are located. The chamber can be modified to change places and heights of the aluminium strips and therefore also the electron creation points in the drift volume. For this test candidate, a diagonal setup in the 3D volume has been chosen, that simulates a passage of an ionizing particle through the drift volume, leaving charge clusters at different heights along its track. The arrival areas of the electron clusters on the test Micromegas have been calculated and are marked in the photo in figure 5.1 as the areas A to H. The laser hits all aluminum strips simultaneously, but the electrons created at the lowest strip (H) in the drift space will arrive first, the electrons from the highest strip (A) the latest, due to the comparably long drift times inside the gas filled drift volume.

The eight sensitive areas have a size of $(12 \times 12)\,\mathrm{mm}^2$. The areas differ in strip width (S_W) from $0.1\,\mathrm{mm}$ to $0.3\,\mathrm{mm}$ and strip pitch (S_P) from $0.2\,\mathrm{mm}$ up to $2\,\mathrm{mm}$, to be able to compare different combinations of readout designs. Table 5.1 gives an overview about all measurements related to the Micromegas setup.

The choice of these combinations of different strip widths and strip pitches should cover the possible range for the New Small Wheel Micromegas design, that had not been chosen at the time of the manufacturing of the test candidate. The limiting factor for the strip and gap width is the photolithographic manufacturing technique that is used to create the copper strips on the PCB.

Examined though a microscope, the mesh structure and the strips underneath it are clearly

Table 5.1.: Configuration of the sensitive areas of the Micromegas test candidate and the assignment to the different connectors.

area	strip width S_W [mm]	strip pitch S_P [mm]	number of strips	connector assignment
A	0.2	0.4	16	all on con6
B	0.3	0.6	16	all on con5
C	0.1	0.4	16	all on con4
D	0.1	0.2	20	16 on con3, 4 on con2
E	0.2	1.0	12	all on con2
F	0.1	2.0	6	all on con1
G	0.2	2.0	5	all on con1
H	0.3	2.0	5	all on con1

(a) focused on strips   (b) focused on mesh   (c) focused on pillar
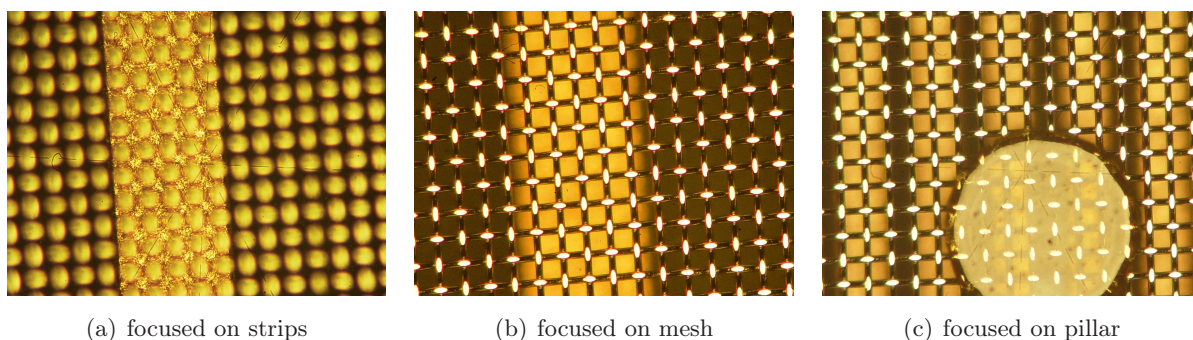
Figure 5.2.: Microscopic images of the Micromegas test candidate. The strip width on pictures (a) and (b) is 0.3 mm and the mesh pitch is 0.065 mm.

visible. The copper surfaces of the strips are reflecting the yellow microscope light in a golden color in figure 5.2(a). The mesh has been rolled flat and the flattened parts are also reflecting the microscope light in figure 5.2(b). A 2 mm diameter ceramic pillar is visible in picture 5.2(c). The mesh is embedded in the topmost part of the pillar to fix it mechanically and to keep the exact distance to the anode strips on the board surface.

Signals that are created on the strips by the gas amplification processes are guided to the back side of the board, where 40-pin connectors are located. To ensure minimal crosstalk and noise influences to the small unamplified strip signals, every second pin on the connectors is grounded. Also on the board itself, ground areas are put between the signal routes wherever possible. Electronic preamplification inside the chamber is not possible because of space and outgassing issues of the electronic parts. Therefore the signals are lead on the shortest possible path through the bottom of the chamber to the VV30 amplifiers. Since there are more strips
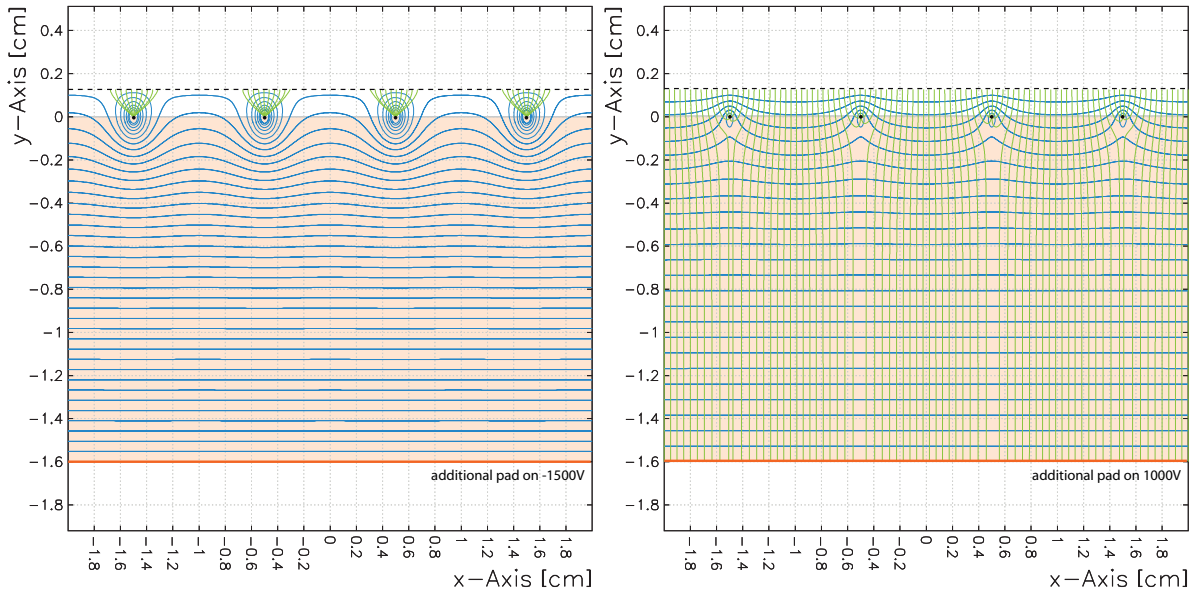
Figure 5.3.: An additional copper layer on the bottom of the Micromegas test candidate influences the field shape between mesh and anode strips on the board. Left: A negative voltage forms field lines similar to those in a MWPC, while a positive pad voltage parallelizes the field in the amplification area even more (right). Simulation done with Garfield (version 9).

on the Micromegas than FADC channels (2×8 available) the signals are routed in groups of 16 to the connectors. All connectors and signals leave the chamber through the bottom feed-through board and are available on different connectors outside the gas volume. Therefore the decision, which part of the Micromegas will be connected to the FADC at a time, can easily be made by changing the cabling without opening the chamber and possibly causing a change of the measurement conditions.

On the bottom side of the Micromegas, in addition to the six signal connectors, a copper area is placed directly underneath the sensitive areas on the top. A detailed technical view of the test candidate with the schematics of top and bottom layer can be found in figure B.1. This copper layer can be set to an independent potential and therefore can deform the field lines in the amplification area near the strips. Figure 5.3 shows a Garfield simulation of the influence of a negative and a positive potential. A positive potential can cause the field lines to get a form comparable to the field lines of a MWPC, which could affect sparking affinity at high gains.

The power supply for the strips is a high voltage supply with an extremely sensitive current meter (resolution $0.05\,\mathrm{nA}$) that can detect and monitor also small discharges and changes of gain. This opens possibilities for sparking studies using this additional potential layer.

5.2. Gain Studies

The Micromegas test candidate presented in chapter 5.1 has been studied using photoelectrons created by the UV laser to study the relative gains of the eight different pad configurations (see table 5.1) with different strip widths and different strip pitch. For these measurements a different laser has been used, with a lower pulse power. The intensity of the laser used in this measurement is comparable to 2/3 of the reduced laser intensity (factor 0.53) of the newer one.

The UV laser with the eight focused partial beams hits the eight aluminum strips at different heights inside the drift volume and creates eight electron clusters of each about 11000 electrons that drift towards the Micromegas test candidate surface. The electron creation points on the aluminum strips A to H are aligned above the respective sensitive areas of the Micromegas A to H. The laser spots on the aluminum strips have a diameter of about 0.3 mm to 0.7 mm. The created electron clouds initially have about the same size, but their diameter increases on their way down towards the detector due to lateral diffusion caused by interaction with the gas molecules. The electron distribution of the cloud can be measured with the strips of the Micromegas for each pad.

Since the FR4 material of the Micromegas board is hygroscopic, the test candidate must be flushed at least 48 hours before the measurement with the dry $ArCO_2$ gas to remove any trace of water. This is necessary to reduce the probability of discharges and to guarantee the best and most stable conditions during the measurements. A power supply with a precise current meter controlling a trip mechanism is also important to prevent the Micromegas taking damage from localized stable plasma discharges that can cause severe damage to the mesh.

While the drift voltage is kept constant at 10 kV, the mesh voltage that determines the amplification of the Micromegas is varied during this measurement. It starts from the value where the first small signals can be observed, which is around 380 V to 400 V, and increases until the stable operation of the Micromegas is no longer guaranteed. This condition arises if too many discharges between mesh and anode strips occur in a short time. A sign for this is an unusually high mesh current or an unstable, fluctuating mesh current, which can start between 515 V and 535 V for the different pads.

An FADC event is displayed in figure 5.4 and examples of electron distributions of this measurement are shown in figure 5.5. All electron clusters have a diameter of about 2 mm to 5 mm when they are detected by the Micromegas. The electrons are distributed over different numbers of strips since some of the eight pads have different strip pitches. Also the influence of the diffusion is different, since the clusters are released in different heights over the Micromegas. For all pad configurations except the 2 mm pitches a clear gaussian shape of the electron clouds on the pads is registered. The two-dimensional lateral gaussian shape of the electron cloud is integrated over one-dimensional strips. Due to the gaussian character of the electron cloud distributions, the characteristics like width and RMS do not change during this integration, only the amplitude changes for a symmetric electron cloud in both lateral directions. One of the fits is shown in a three-dimensional drawing, with the strip peak intensity as the third coordinate. The timing
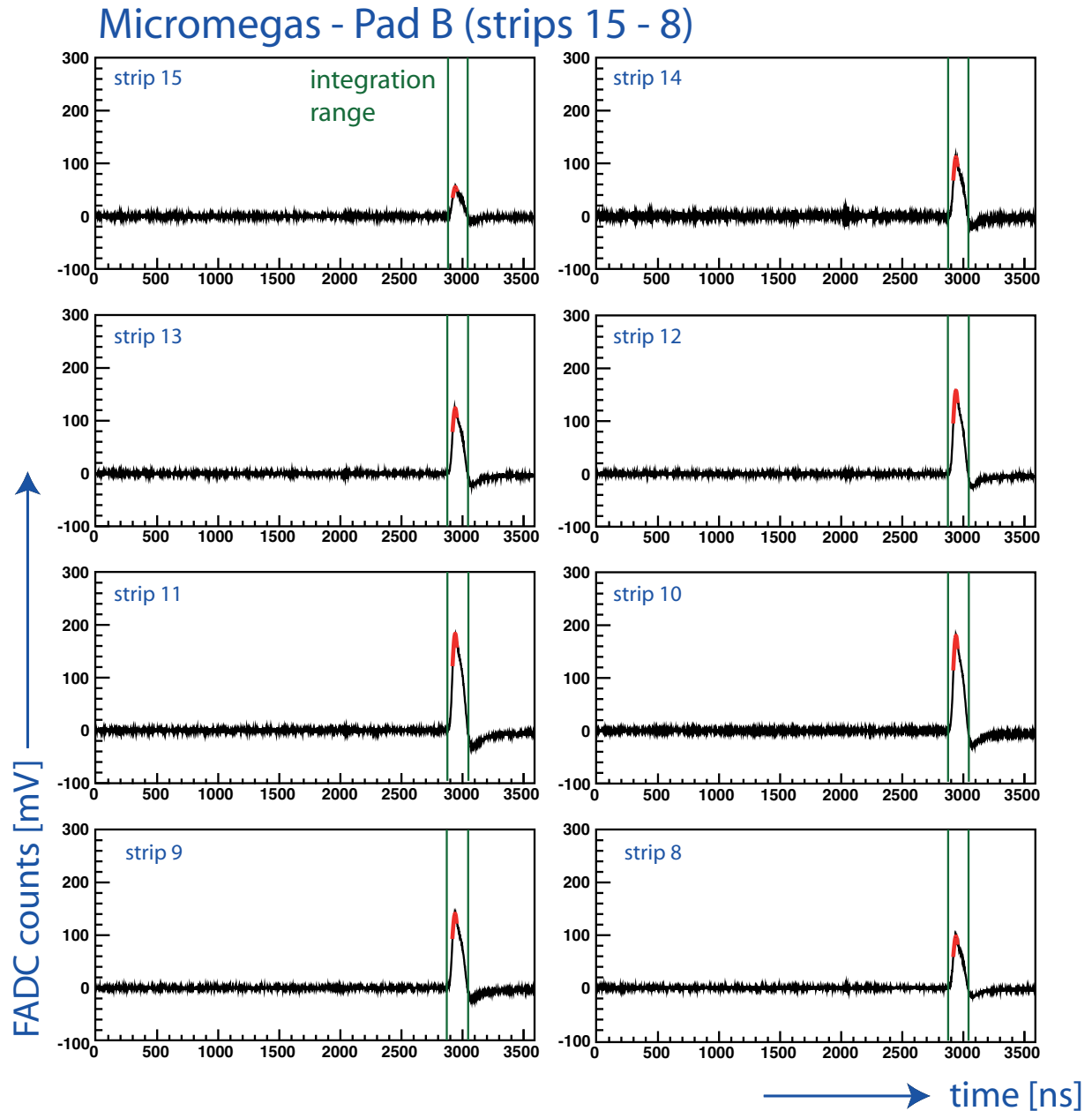
Figure 5.4.: Signals for 8 of the 16 channels of a Micromegas for a laser pulse with one laser spot distributed over all wires (pulse continues on wires 7 to 0). The peak tops are fit and the results are averaged over at least 100 events to minimize statistical errors on the pulse heights.
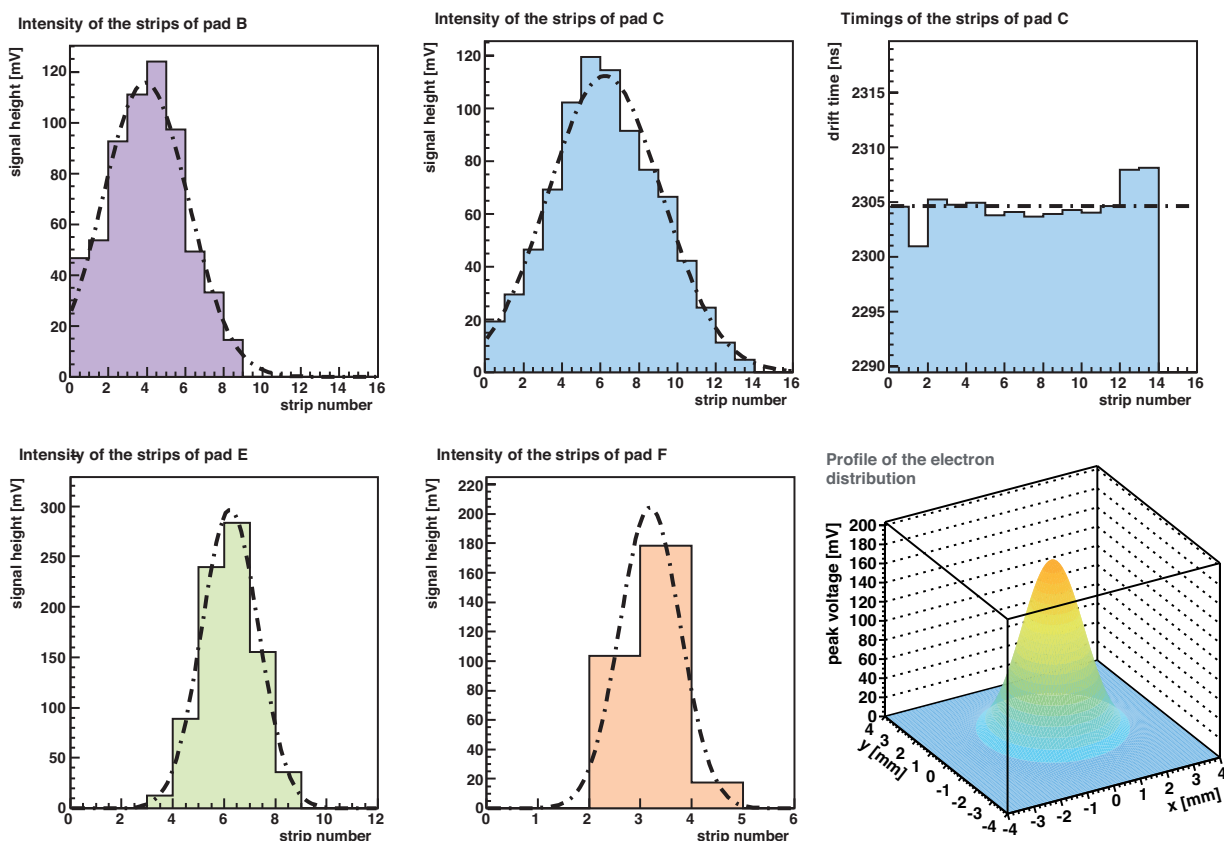
Figure 5.5.: The beam profiles of the Micromegas pads show a Gaussian shape with an average width of 4-5 mm. The timing resolution is not good enough to display the electron cloud distribution along the vertical direction, as visible in the top right graph. The bottom right picture shows a 3D image of such an electron cloud.

resolution for the electron distributions is not good enough to show the structure of the electron clouds along the vertical direction. As a visual example, the measured signal height distribution of pad E for all mesh voltages of this series are shown, stacked, in the graph in figure 5.6.

At 400 V the peaks on the central strips of the pad are barely distinguishable from the background. The signal height of the single strips increases exponentially with increasing mesh voltage until at 515 V the discharges set in.

The complete results of the variation of the mesh voltage are shown in figure 5.7. All electron distributions on the different pads for all measured mesh voltages are fit with a Gaussian function. The sum of the distribution has been inserted as y-coordinate into the graphs. It is a good approximation for the overall produced charge in the amplification processes for each pad.

The resulting curves are fit with an exponential function $f(x) = e^{c_0} \cdot e^{c_1 \cdot x}$. The fit results are
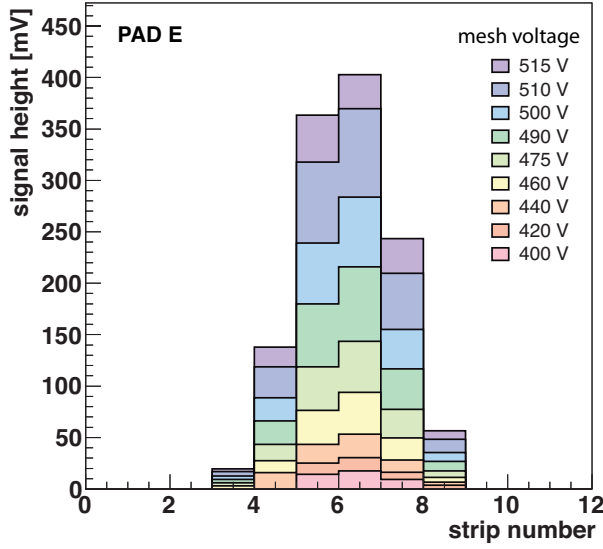
Figure 5.6.: The absolute signal heights on pad E for the different mesh voltages controlling the gain. The peak starts to appear around 390 to 400 mV and grows until the mesh voltage gets instable and the measurement is terminated.

given in table 5.2.

Especially in the logarithmic plot, it can be seen that the parameter c_1 is about the same for all pads: the curves are parallel and some are even identical within their errors. If the curves are compared with the pad configurations, it is clear that the strip pitch is the most important factor for the gain. The pads with 2 mm strip pitch have the lowest gain while pad D with the 0.2 mm strip pitch shows the highest gain. The gains of the three pads with pitches between 0.4 and 1.0 are also close together. This can be explained by effects due to the different strip widths that have an influence on the electric field in close strip proximity where the amplification takes place. There might also be small deviations in laser beam intensity. The beams are only equal in intensity, if the laser light hits the beam splitters with the polarization plane in the correct orientation. Angular deviations will cause differences in the relations of the split intensities, which may add up during the 3-level splitting process.

The used laser (older unit) produces about

$$Q_l = 9100 \pm 1100 \qquad (5.1)$$

electrons on the aluminum strips for each pad. The integrated voltage U_I over all strips for pad E for example is

$$U_I = (1200 \pm 10)\,\mathrm{mV} \qquad (5.2)$$

at a reasonable mesh voltage of $U_{mesh} = 500\,\mathrm{V}$. Adding the single pulses of the distribution with equal weight, the sum U_b reflects the charge of the whole electron cloud:

$$U_b = U_I/A = (25.6 \pm 0.3)\,\mathrm{mV} \qquad (5.3)$$

height before the amplification in the VV30 amplifier takes place, with A being the amplification of 46.9 ± 0.3 calculated in section 4.2.1. To further proceed in the calculation of the gain of
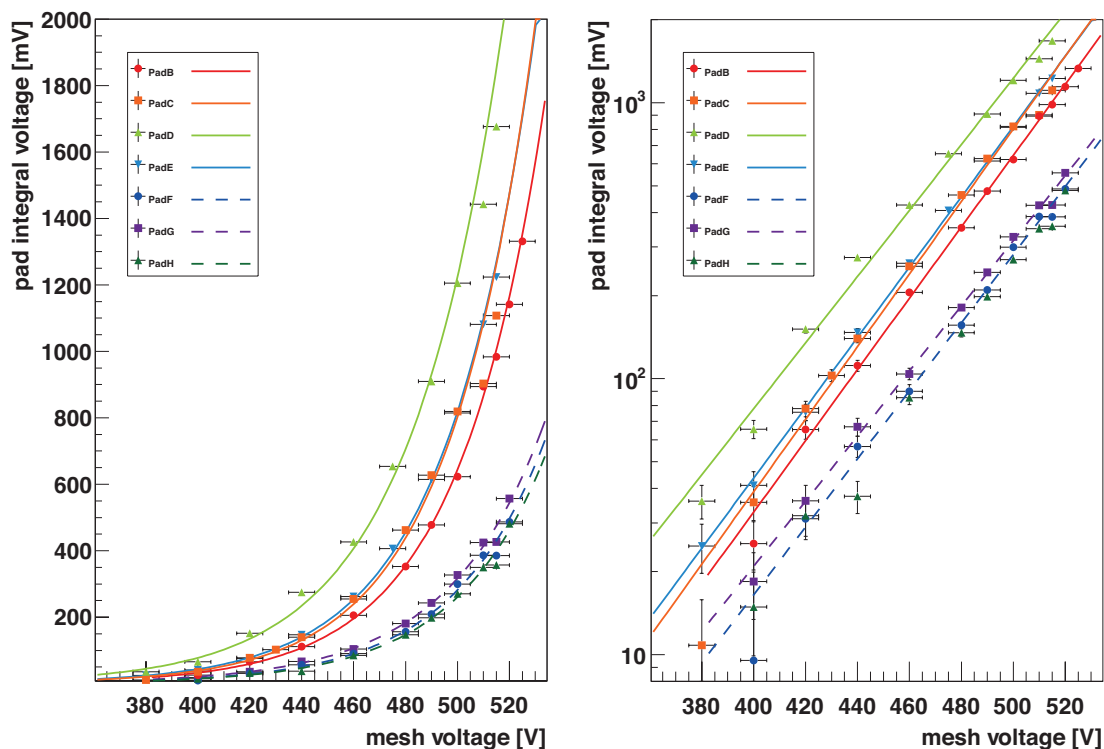
Figure 5.7.: The integrated signals for each pad that are proportional to the collected charge on linear and logarithmic scale for different wire voltages. Strip configurations with similar pitches show similar behavior, independent from the strip width.

Table 5.2.: Results of the gain studies with the Micromegas test candidate. The optical line A was not available due to a technical defect in the optics.

pad	strip width [mm]	strip pitch [mm]	c_0	error c_0	c_1	error c_1
A	0.2	0.4	not meas.	-/-	not meas.	-/-
B	0.3	0.6	-8.40	0.61	0.0297	0.0013
C	0.1	0.4	-8.44	0.62	0.0303	0.0013
D	0.1	0.2	-6.67	0.54	0.0276	0.0012
E	0.2	1.0	-7.95	0.60	0.0293	0.0013
F	0.1	2.0	-8.55	0.76	0.0284	0.0016
G	0.2	2.0	-7.82	0.69	0.0272	0.0014
H	0.3	2.0	-8.74	0.79	0.0286	0.0016
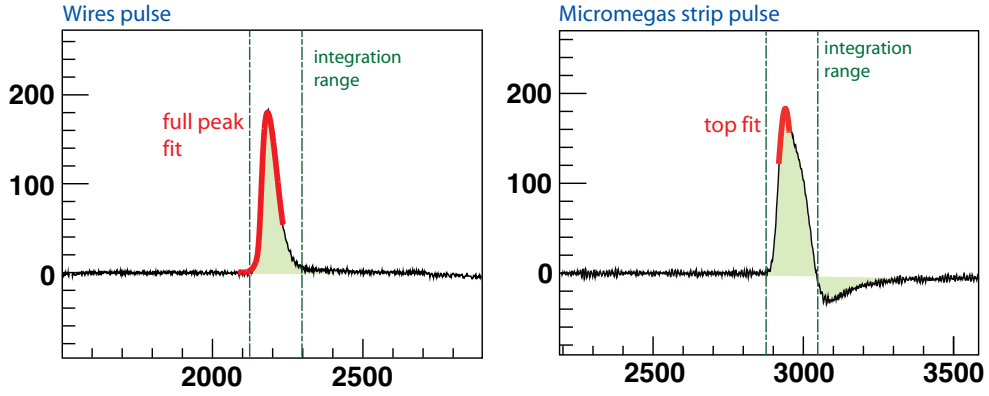
Figure 5.8.: While the wire pulses have the optimal form and result in clean VV30 output pulses, the Micromegas pulses are longer and exceed the integration time of the VV30 amplifier. This results in an undershoot and a characteristic shoulder that makes the integral of the pulse very non linear.

the Micromegas, one needs to assume that the Micromegas pulses have about the same shape as the wire pulses and the calibration pulse unit. Then a total pulse of $U_b = (25.6 \pm 0.3)\,\text{mV}$ would be equivalent to a number Q_s electrons on the strips, using the conversion factor $c_b = (0.82 \pm 0.05) \times 10^7$ electrons/mV peak height before the amplifier:

$$Q_s = U_b \cdot c_b = (20.9 \pm 1.4) \times 10^7, \tag{5.4}$$

resulting in a gain M of

$$M = \frac{Q_s}{Q_l} = 23100 \pm 2800. \tag{5.5}$$

Therefore an integrated pulse height on the Pads of $(1200 \pm 10)\,\text{mV}$ translates under the aforementioned assumptions into a gain of $\approx 23100 \pm 2800$, which is equivalent to a gain factor increase of about $(19.2 \pm 2.3)\,\text{mV}^{-1}$ for each measured mV of pad sum voltage.

But there is an objection to this very rough approximation. The assumption that the signal form of the Micromegas is about the same as the calibration unit, is not very precise. The signal itself cannot be measured, but the reaction of the VV30 amplifier to the Micromegas pulse in comparison to the wire pulse is shown in figure 5.8. The VV30 reaction to the wire pulse is a well defined short pulse without undershoots, which shows that the input pulse is compatible with the specifications of the amplifier. The Micromegas pulse instead shows a shoulder and an undershoot. This behavior is a hint for a longer pulse length and different timing constants.

A measurement with the wire pulse form generated by a pulse generator with time constants between 1 ns and 30 ns is done. Starting from a value of about $t_0 = 15\,\text{ns}$ and higher, the amplifier output developed the previously mentioned structures in its shape. Therefore the Micromegas pulses can be assumed to have a different shape and different time constants than the wire pulses.

The quantitative reaction of the system to these pulses is unknown, but qualitatively it can be estimated that the amplifier loses strip charge because of the limited integration time of the electric input circuit, which is probably considerably shorter than the pulse time. This would lead to an underestimation of the gains.

Comparing the input pulse charge and the output signal height for the pulse generator measurement above shows that there is no linear context between output discrepancy and the time constants t_0, the relation is not even uniformly continuous. At least the overall differences between the output pulses for different time constants (and the same charge) are not more than about 50 % of the larger pulse. This means that the estimated gains under the aforementioned assumptions might be underestimated up to a factor of about 50 % to 100 %.

The different Micromegas pulse shape also leads to the circumstance that the peaks cannot be fit anymore with a reasonable fit function over the whole width. The best procedure was found to be a fit mechanism that first detects the peak position and height and then fits a gaussian only to the top of the peak. Peak integrals or bin sums, which are even more precise than the peak height if used with the wire pulse shape, were found to be incorrect for the Micromegas pulse shape and are therefore not used for any Micromegas analysis.

5.3. Drift Studies

Drift and diffusion processes of charged particles inside a Micromegas affect its characteristics and the achievable resolution. With the Micromegas test chamber, it is possible to carry out drift velocity measurements and diffusion studies of photoelectrons in the drift volume. The relatively long drift space of up to 13 cm allows to see the electron clusters disperse on their way down to the Micromegas. The creation points of the electron clusters on the aluminum strips in different heights provide enough variation on the drift length to see the diameter of the electron clusters on the Micromegas pads changing with the applied drift voltage. The simultaneous electron creation at eight different heights also allows to determine electron drift velocities over the full range of the drift field.

5.3.1. Electron Drift Velocity Measurement

After creation on the surface of the aluminum strips, the electrons are drawn towards the Micromegas by the applied electric drift field. It is created by the PCB stack that also holds the aluminum strips in position and is very homogeneous (see chapter 3.4 for details). The top board voltage creating the drift field can be varied in a range from about 2200 V to 12500 V. The lower limit is given by the need for a minimum drift field to avoid instant reabsorption of the electrons on the metal surface of the strips, while the upper voltage is limited by the spark gaps inside the drift field stack.

The electrons start their travel through the gaseous atmosphere at different heights but all at the same time. Therefore it is not necessary to know the exact creation time of the electrons.
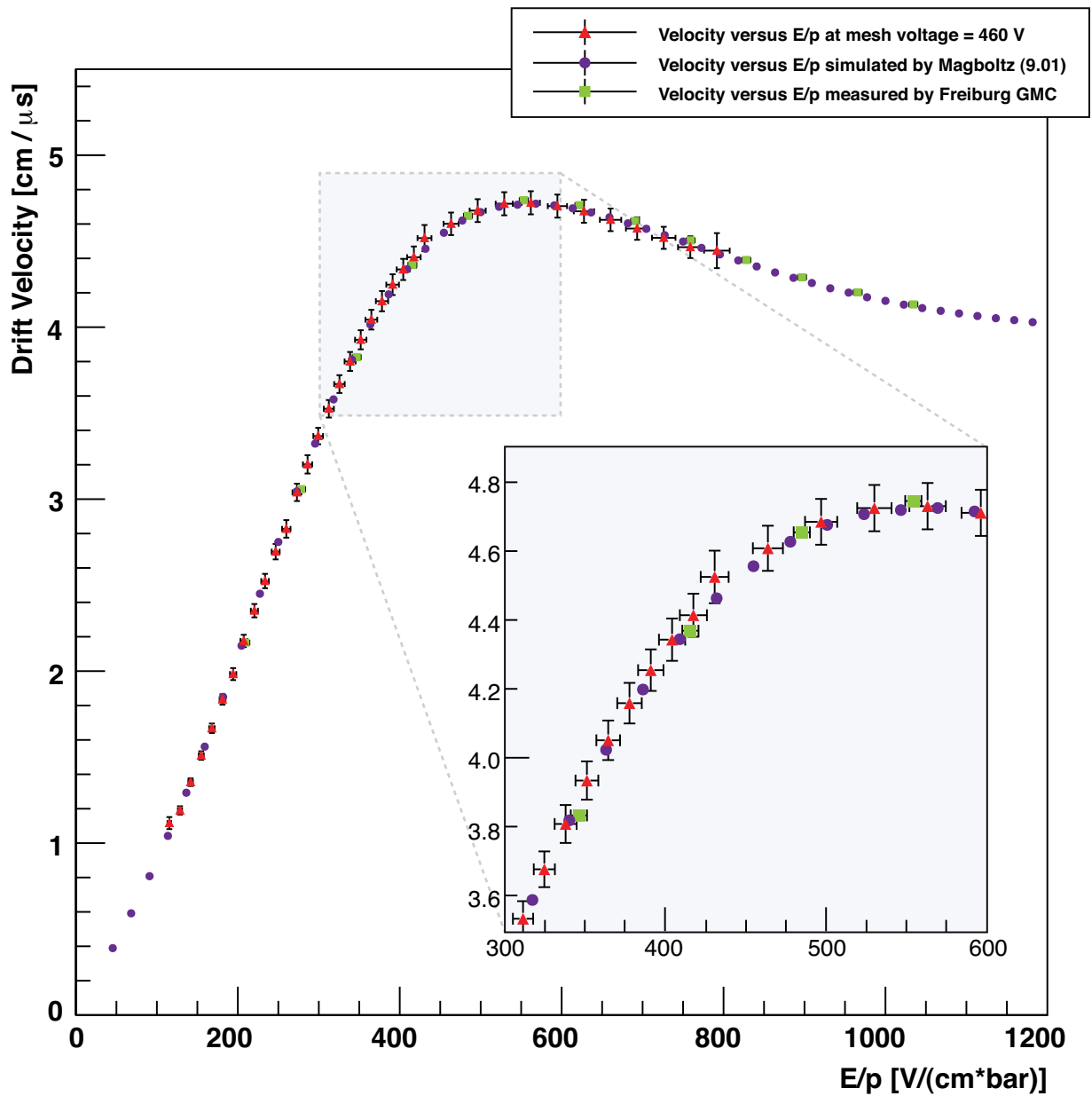
Figure 5.9.: The electron drift velocity as a function of the reduced electric field E/p measured with the Micromegas and the test chamber. The curve is compared to two different studies: the measurement by the Freiburg GMC [29] and the statistical Magboltz simulation.

The drift velocity can be calculated from the drift time differences, if the creation heights over the Micromegas are known precisely. Also the timing of the amplification processes in the Micromegas do not influence the drift time measurements.

The drift voltage is varied between 2200 V and 12500 V. The electron cloud distributions are measured for each pad and each drift voltage individually with 100 events. The arrival times are averaged over all strips and all events of the pads. For each drift voltage, the averaged arrival times of all pads are plotted against the respective drift distances. Linear fits of these plots give the drift velocity for the assigned drift voltage and represent one entry in the drift velocity plot in figure 5.11.

The drift plot also includes a Magboltz simulation of the electron drift velocity in the energy range covered by the Micromegas test chamber. A third curve is added and represents a measurement of the Freiburg Gas Monitoring Chamber (GMC) using a similar measurement principle and exactly the same gas composition of $ArCO_2$ (93 %/7 %).

Control Measurements for Precise Absolute Drift Velocities

The exact knowledge of the absolute values of pressure in the chamber and the drift field strength is essential to obtain correct absolute values for the electron drift velocity measurement.

All used power supplies have been checked for systematic deviations and especially the potential on the bottom of the drift field stack has to be adapted for each drift voltage to ensure a homogeneous and constant electric field in the drift volume as well as in the region between Micromegas and field stack. Since the Micromegas mesh voltage influences the latter field, it cannot be set by a voltage divider chain but must be determined individually.

To measure the pressure inside the chamber, a pressure regulator sets its value to a certain pressure p_{set} and also reads back a value for the current pressure p_{back}. For most applications of the chamber the pressure does not need to be known precisely on an absolute scale and the built-in measurement function is sufficient. The regulation mechanism of the pressure sensors itself is operating well, but after setting a pressure value, p_{back} stabilizes at a reproducible value, which is about 18 mV higher than p_{set}.

There is no uncertainty or error given in the manual of these instruments. A second instrument is tested and the two values for p_{back} differ by more than 50 mbar. The assumption can be made that just averaging the results for the different sensors does not make sense since this is no statistical deviation.

A measurement of the absolute chamber pressure needs to be done independently from these instruments to find out the exact absolute value needed for the drift velocity. Since the available pressure sensors only provide relative measurements or are of the same type of model than the used pressure regulators, a very simple method has been chosen. It is explained in appendix A.3 and uses the hydrostatic pressure of water to compare the chamber pressure with the current outside pressure, which was obtained by a local weather station. The achieved value for the absolute chamber pressure is $p_{ch} = (1085.84 \pm 0.2)$ mbar, which is close to p_{set}. It can be assumed that the internal conversion factors of the pressure regulator instruments, possibly realized via resistor

networks, drifted away over the years and need a recalibration to guarantee correct absolute values. The regulation mechanism itself does not seem to be influenced by this.

The chamber pressure for all analysis was corrected with this factor and the results are in good agreement with the expectations.

Results of the Electron Drift Velocity Studies

Comparing the three curves, they are all identical within their error bars, although the drift velocity is very sensitive to the used gas composition and small deviations in the pressure and the electric drift field. The zoom in figure 5.11 shows the peak region of the curves, which is characteristic for the used gas composition. The small deviations between the test chamber measurement and the Magboltz simulation can be explained by a slightly different gas composition. The GMC that is measuring the same gas with a similar measuring principle uses only the minimal necessary number of sampling points to determine the drift velocity, since it is measuring and analyzing in real time.

This measurement of the absolute drift velocity proves the accurate operation of the optical part of the chamber and the good quality of the homogeneous drift field. The overall setup, data acquisition and analysis are well understood and can be adapted to many possible measurements regarding Micromegas and MPGD in general.

5.3.2. Electron Diffusion Studies

The drift of the electrons inside the drift volume of the test chamber above the Micromegas can also be used for electron diffusion studies. When they are created near the aluminum strip surface, the electron clouds are small and about the size of the focused laser spots. On the Micromegas pads, the electron clouds show a gaussian shape (see section 5.2) that varies with the applied drift voltage. This allows for absolute measurements of the transverse diffusion coefficients dependent on the reduced electric field.

Only transverse diffusion can be studied with the setup, since the output height and pulse shape of the VV30 amplifiers do not depend on the temporal distribution of the electron arrivals on the Micromegas strips. Some of the pad timing histograms (like shown in figure 5.5) show a rudimentary parabolic shape, but the resolution is not high enough to do a precise fit and see the alterations with the electric drift field. Additionally, the expected variation on the longitudinal diffusion is small.

Figure 5.10(a) and 5.10(b) show the transverse and longitudinal diffusion of electrons simulated by D.M. Binnie [42]. The shown concentrations in the simulation in figure 5.10 do not cover the mixture $ArCO_2$ (93 %/7 %) used for the studies in this work, but the concentrations 90 %/10 % and 95 %/5 % (all for for $p = 1$ bar absolute pressure) are given. Due to the similar shape of the two curves for transverse diffusion a simple interpolation is possible, but only gives a rough estimation on the shape of the curve.

The sensitivity on the electron cloud diameter of the eight pad configurations of strip widths and strip pitches is different. Since the diameter of the electron clouds on the pads is about

(a) Transverse diffusion σ_T for $p = 1\,\mathrm{bar}$

(b) Longitudinal diffusion σ_L for $p = 1\,\mathrm{bar}$
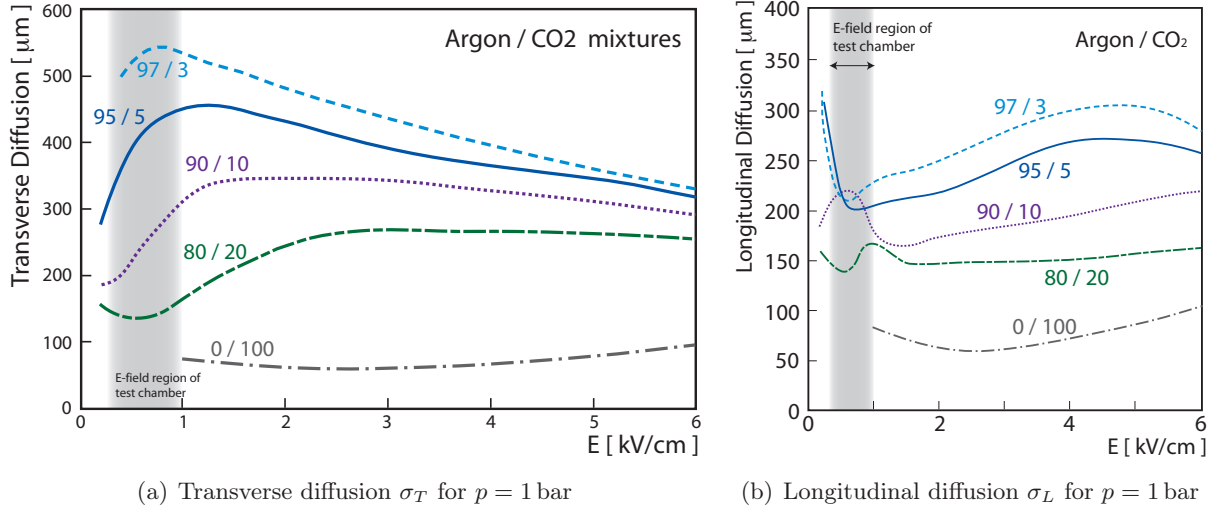
Figure 5.10.: Diffusion simulated by D. M. Binnie [42]. The shape of the curves is in agreement with the measured data available at publication date of the paper. Diffusion is defined in the paper as the increase of the root mean square of a distribution over one centimeter drift length in units of μm.

2 mm to 5 mm, only the pads with a pitch less than 1 mm are able to resolve the lateral electron distribution with sufficient accuracy.

The same measurement that provides the data for the electron drift velocity analysis is also suitable for the diffusion studies. Instead of using the cluster arrival time on the different pads, the root mean squared (RMS) of the electron distribution on the strips is calculated and averaged for the 100 events for each pad. Some of the fits that were automatically done by the root analysis program are not describing the data well due to boundary effects. A cut on the fit quality is done using constraints on the maximum acceptable chi-square of the fit and the mean peak position.

The transverse diffusion coefficient D can be calculated from the increase of the RMS of the distribution σ_x with the relation defined in section 2.3.3:

$$\sigma_x \;=\; \sqrt{2\,D\,t_d} = \sqrt{2\,D\,\frac{s_d}{v_d}} \tag{5.6}$$

with D being the diffusion coefficient in units of $\mathrm{cm^2\,s^{-1}}$, t_d the drift time of the electrons, s_d and v_d the drift distance and the drift velocity respectively. From the electron distribution the difference of the RMS $\sigma_x = \sigma_x^{strip} - \sigma_x^{creation}$ can be obtained. The drift velocity v_d is known from the measurement and can be interpolated from the drift velocity curve, where the exact values of E/p are missing.

The data sets from pads B, C and D are suitable for this measurement. The strip pitch of pads E to H is too large and the electron cloud of pad A is too close to the egde of the sensitive area.
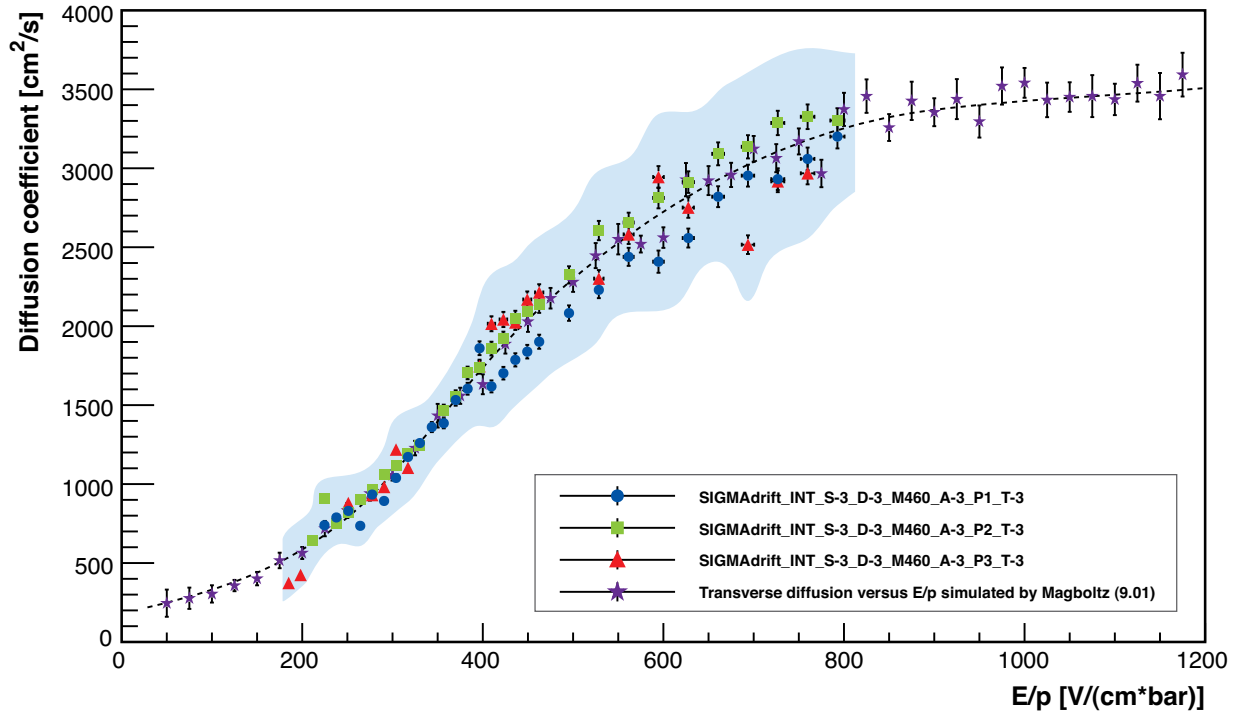
Figure 5.11.: Measured transverse diffusion coefficients dependent on the reduced electric field E/p calculated from the results of pads B, C and D. The blue area marks the systematical errors arising from the large uncertainties on the initial electron spot size. The measurements are compared to the diffusion coefficient calculated by Magboltz for the same conditions. The dashed curve follows the Magboltz simulation and is added only to guide the eye.

The measured results for the transverse diffusion coefficient are shown in figure 5.11. A simulation done with Magboltz (see section 2.3.3) for the mixture of $ArCO_2$ $(93\% / 7\%)$ provides more precise results than the simulation by Binnie and is shown in comparison with the measured transverse diffusion.

The measurement results follow the Magboltz simulation within their larger error bands due to systematic errors. The error bands arise from the fact that the RMS of the initial electron cloud $\sigma_x^{creation}$ can only be estimated by comparing it to the laser spot size and its RMS. This is evaluated optically to be around $(0.25 \pm 0.15)\,\mathrm{mm}$. The smaller error bars are mainly caused by statistical errors.

Despite the unavoidable large error bands, the measurement is in good agreement with the simulations and shows a reliable performance of the Micromegas test candidate as well as of the overall Micromegas test setup.

5.4. Studies of the Micromegas Amplification Field Geometry

The test candidate Micromegas has been designed to provide the possibility of investigating the gain and the sparking behavior under the influence of a second cathode potential underneath the strip layer. In order to provide this additional potential, a copper surface has been placed on the bottom side of the PCB that carries the strips and the mesh on the upper side, see section 5.1. The copper surface is isolated from every other structure and potential and can be set to positive and negative voltages.

To measure the reaction of the Micromegas during normal operation, the copper layer potential is varied while the Micromegas measures the UV photoelectrons. The mesh current is monitored during the measurement with the very precise integrated current meter of the HV power supply [1]. Since the linear range of the VV30 amplifier is limited and the measurements exceed this region, only the amplifier output of one of the strips of pad E is monitored in real time with an oscilloscope. Because all laser beams except the partial beam that arrives on pad E are blocked to focus only on one pad, the mesh current between anode and cathode is a very accurate measure to monitor already small changes of the gain in the Micromegas with a high precision. Figure 5.12(a) shows the exponential increase of the mesh current as a function of the mesh voltage.

At mesh voltages of $U_{mesh} = 460$ V and $U_{mesh} = 525$ V the voltage of the additional copper layer U_L is raised from $U_L = 0$ V to positive HV until discharges between mesh and anode strips trigger the trip function of the HV. It is set to a current limit of 200 nA for a minimum overcurrent time of 3 s. The same procedure is repeated with negative voltages on the copper layer. The results can be found in figure 5.13. The mesh current is shown as a function of U_L for both mesh voltages.

Although the current clearly reacts on changes of the U_L during the ramp up process, it shows no dependence on the absolute value of U_L and therefore also the gain is independent from U_L in the covered potential ranges.

In another measurement, the mesh voltage is raised for different values of U_L under normal operation with the UV laser until discharges set in. The measured values for U_L are -1000 V, -500 V, 0 V, 500 V, 1000 V, and 1500 V. The range between $U_{mesh} = 460$ V and $U_{mesh} = 530$ mV is measured in steps of 5 V to 10 V. The measured currents, as well as the measured amplifier outputs for the whole curve, are nearly identical within their respective measurement errors for all six different U_L. Also the value for U_{mesh} where discharges set in is stable and independent from U_L. For each U_L the breakdown U_{mesh} is around (531.5 ± 0.5) V.

Comparison of the Discharge Gain with the Raether Limit

The mesh current is proportional to the gain of the Micromegas on the only pad used for the measurement, which is pad E. Even though the amplifier output saturates at about 440 mV (see section 4.2.2 and figure 5.12(b)), the mesh current still accurately monitors the amplification processes. Because of the linear relation between the mesh current and the amplifier output,

---

[1]CAEN N1471HA (2 Channel 5.5 kV NIM HV Power Supply High Accuracy Module) provides HV with current measurements with a precision of 0.05 nA

(a) Mesh current versus mesh voltage

(b) Amplifier output versus mesh current
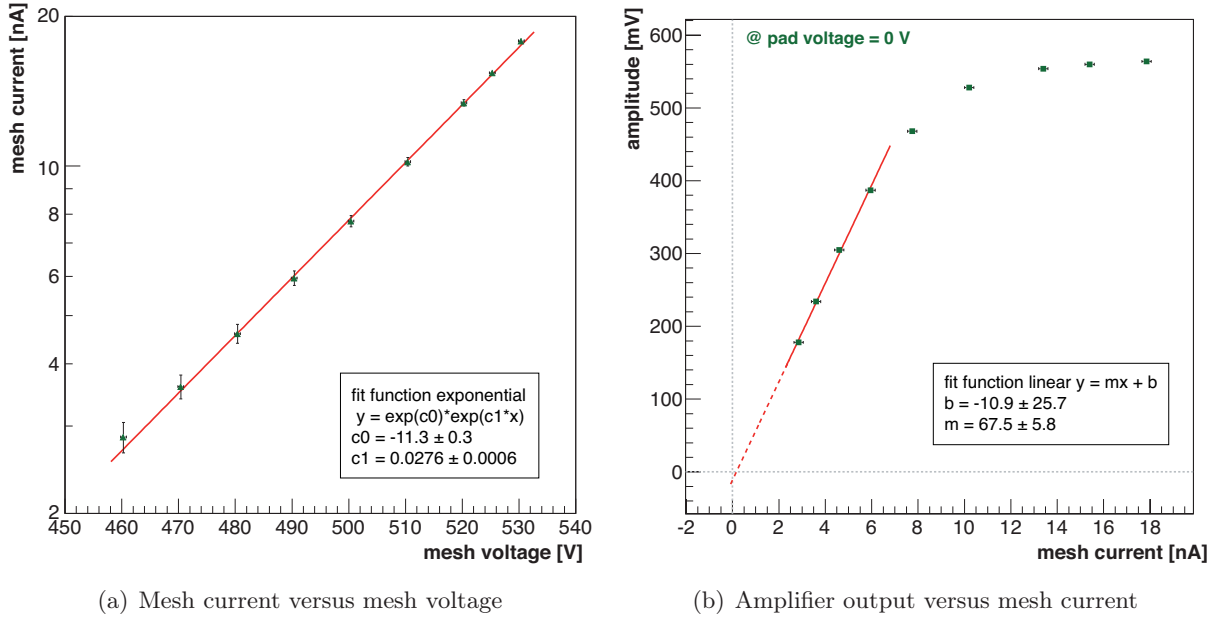
Figure 5.12.: The mesh current is caused solely by the avalanches between mesh and anode strips and is therefore directly proportional to the gain of the pad. The exponential behavior proves a stable operation of the Micromegas test candidate on pad E (left). The right figure shows the linear relation between the mesh current and the amplifier output until the end of the linear range of the amplifiers is reached at 440 V.

calculating the gain for a moderate U_{mesh} allows conclusions for the higher gains, even though only the mesh current is available.

The laser spot electron number for the laser used for this measurement is $Q_l = (13600 \pm 1600)$. The integrated peak voltage at $U_{mesh} = 490\,\text{mV}$ can be calculated adding the strip voltages for the used pad E. The pad sum voltage is

$$U_I = (1000 \pm 10)\,\text{mV}. \tag{5.7}$$

This is equivalent to a total strip voltage of pad E of

$$U_b = \frac{U_I}{A} = (21.3 \pm 0.3)\,\text{mV} \tag{5.8}$$

before amplification in the VV30. With the conversion factor of $c_b = (0.82 \pm 0.05) \times 10^7\,e^-/\text{mV}$ peak height before the amplifier, the calculated charge on the strips is

$$Q_b = U_b \cdot c_b = (17.5 \pm 1.1) \times 10^7 \tag{5.9}$$

electrons, resulting in a gain of

$$M = (12800 \pm 1800), \tag{5.10}$$
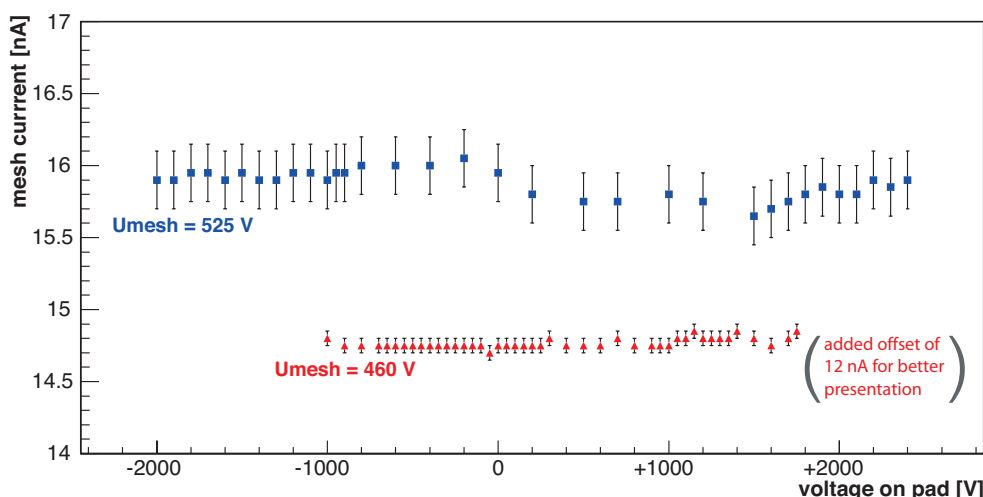
Figure 5.13.: The behavior of the mesh current as a function of the applied voltage on the additional bottom electrode for two different U_{mesh}. No increase of the currents or current instabilities show the proximity to possible discharges. Small deviations in the mesh current around $0\,\mathrm{V}$ pad voltage are caused by the measurement order and a slow charging effects after the previous discharge.

with an additional systematic uncertainty of $(50\text{-}100)\,\%$ (see section 5.2).

The same calculation can be done at the typical breakdown voltage $U_{mesh} = 531.5\,\mathrm{mV}$. Using the linear context between mesh current and amplifier output shown in figure 5.12(b), this gives a theoretical number of $U_I = (3530 \pm 50)\,\mathrm{mV}$ integrated pad signal, which leads to a number of $Q_b = (6.2 \pm 0.4) \times 10^8$ electrons and ions in the avalanche distributed over an area of about $0.3\,\mathrm{cm}^2$ with a higher charge concentration in the center of the distribution. The calculated gain under the assumptions for the peak shapes made in section 5.2 is

$$M = (4.5 \pm 0.6) \times 10^4, \tag{5.11}$$

with an additional systematic uncertainty of $(50\text{-}100)\,\%$, which causes unavoidably discharges. The Raether limit is around $M = 1 \times 10^7$ to $M = 1 \times 10^8$, but most Micromegas do not reach these values due to cosmic radiation and other events caused by rare high energy radiation that occasionally create larger avalanches and result in discharges. The Micromegas also shows a training effect and has been in operation with mesh voltages around $560\,\mathrm{V}$ to $570\,\mathrm{V}$ without discharges, which adds another factor 3 to the maximum achievable gain. Before the measurement during which the high gains were achieved, the Micromegas was in a clean and dry gaseous atmosphere for weeks and also the mesh voltage had been set for severals days before using the UV laser photoelectrons with it. This has not been the case for the studies concerning U_L.

(a) pad voltage $U_L = 1000\,\mathrm{V}$

(b) pad voltage $U_L = 500\,\mathrm{V}$

(c) pad voltage $U_L = 0\,\mathrm{V}$

(d) pad voltage $U_L = -500\,\mathrm{V}$

(e) pad voltage $U_L = -1000\,\mathrm{V}$

(f) pad voltage $U_L = -1500\,\mathrm{V}$

(g) pad voltage $U_L = -2000\,\mathrm{V}$
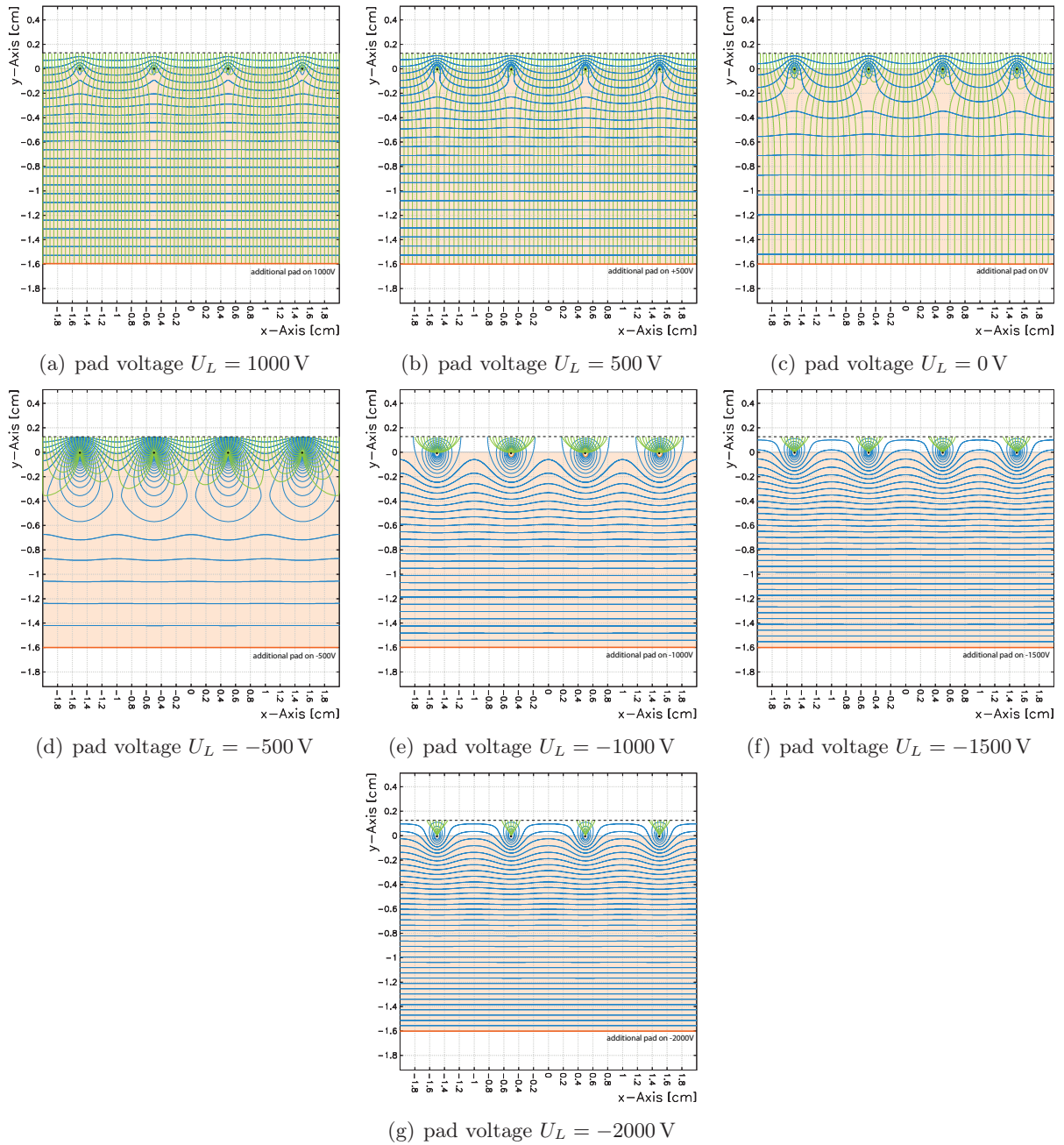
Figure 5.14.: A Garfield simulation of the electric field inside the Micromegas test candidate shows the influence of the additional potential U_L on the bottom side of the Micromegas PCB. The field lines are drawn in light green and equipotential lines in blue.

Garfield Field Simulations for Basic Micromegas Geometry

The Micromegas test candidate geometry with the copper surface on the bottom of the PCB and the additional potential U_L has been simulated with Garfield (version 9). The results are shown in figure 5.14. U_L has been varied between +1000 V and -2000 V, which are the applied voltages in the previous measurement. The strips are simplified as wires of the respective thickness and the dielectricity of the PCB material has been neglected in the simulation, but this should not influence the general behavior of the Micromegas and its reaction to the bottom potential in a significant way.

The additional potential U_L clearly has an influence on the field lines (green) inside the amplification area between mesh and strips. Positive voltages add field strength and a parallel component to the electric field shape, while negative voltages build up a retardation potential and force more of the field line ends onto the strips. The field geometry gets more comparable to the one of a MWPC and develops a radial component, which is especially visible for $U_L = -1500$ V (figure 5.14(f)).

Conclusion for the Micromegas Test Candidate Measurements

As seen in the gain measurements, the additional potential U_L does not change the gain of the Micromegas test candidate. The discharges happening for the measurement with 460 V mesh voltage are an indicator that U_L has an influence on the field form inside the Micromegas. At this voltage, no discharges occurred so far over a very long timespan of operation of the Micromegas without U_L on high voltage. The Garfield simulations show the general behavior of the field in reaction to U_L. Negative values for U_L around -1500 V result in a field geometry more comparable to a MWPC.

The gain measurements also show that the threshold for unavoidable discharges at gain values around $M = (4.5 \pm 0.6) \times 10^4 \, (\pm 100\,\%)$ cannot be raised by U_L. To further investigate the discharge affinity of the Micromegas test candidate under the influence of U_L, long-term measurements would be necessary. The low frequencies of the occurrence of discharges under conditions with and without U_L need to be measured in very long cycles for different mesh voltages close to the discharge limit. These measurements are necessary to determine how much the discharge frequency changes under the influence of U_L. These long-term measurements were not possible in the limited time available for the studies in this thesis.

6. Summary

After the discovery of the Higgs boson at the Large Hadron Collider (LHC) more data is needed to determine the properties and couplings of the newly found particle. Therefore the LHC will increase the luminosity in an upgrade program having several phases over the next 10 years, which poses new challenges to the experiments like the ATLAS detector. New detector technologies are needed that can withstand the higher demands in terms of the capability to preserve their performance despite the increased particle flux. New types of gaseous detectors like Micro-Pattern Gaseous Detectors (MPGD) are attractive alternatives to the current detector technologies. Among the MPGDs are the Micromegas, that are foreseen for the ATLAS Muon New Small Wheel Upgrade and show very good rate capabilities so far.

In this work, a test setup to investigate the properties of Micromegas has been designed and built. The setup uses laser UV photoelectrons as the primary charge to probe the detector. Therefore it is independent of test beams and cosmic rays. The charge is produced by the laser on aluminum strips inside a drift volume with precisely known places and timings. An additional reference readout system based on the principle and the geometry of a multiwire proportional chamber (MWPC) can be activated alternatively and controls the amount of electrons produced by the UV laser.

The setup has been commissioned and the technical system, including analog amplifiers and the performance and gain of the reference readout wires, has been calibrated. Garfield field and amplification process simulations confirm the achieved results. An independent ^{55}Fe source measurement was used to determine the absolute numbers of the created laser photoelectrons in the drift volume.

A Micromegas test candidate unit has been designed and manufactured. It provides eight different readout geometries using strips as anodes with varying strip widths and pitches. An additional cathode layer an the bottom side of the Micromegas readout board opens possibilities for discharge studies regarding the influence of external fields on the sparking affinity.

Several studies with the Micromegas test candidate have been carried out, including gain studies on the different readout configurations as well as drift and diffusion studies. The achieved gains with the Micromegas are in compliance with the expected numbers and depend on the strip pitch. They are also comparable to the gains measured on the MWPC reference readout system.

Drift velocity studies of the electron clusters created by the UV-laser were feasible due to the different but precisely known creation heights over the Micromegas surface. The absolute drift velocity curve measured by the Micromegas test chamber is in very good agreement with the values obtained by the simulation program Magboltz and the measurements of the Freiburg Gas

Monitoring Chamber (GMC) of the ATLAS MDTs.

Diffusion studies with the same gas composition that has already used in the drift measurements ($ArCO_2$, 93 %/7 %) have been carried out using the Micromegas as the detector resolving the electron cloud distributions on the anode strips. The measured absolute diffusion coefficients are in a good agreement with the simulated values by Magboltz. This simulation is relying on a statistical calculation based on the current numbers available in literature.

These measurements show a good overall performance of the Micromegas test candidate, the test chamber setup and the developed analysis programs.

Studies and Garfield simulations regarding the discharge behavior of the Micromegas test candidate and the supplementary cathode on the bottom of the detector unit show that the Micromegas amplification field can be influenced by the additional potential. The simulation indicates that a certain negative retardation potential can form an electric field geometry that resembles the geometry of a MWPC and might show also a lower discharge affinity. Only a long-term experiment can solve this question and it was not possible to perform this in the limited time period available for the work of this thesis.

A. Calculations and Additional Measurements

A.1. Calculated Response Signal of a MWPC

The response signal of a MWPC can be calculated looking at the charge on the wires that is induced by the ions drifting away from the wire, following the potential differences in the chamber. The following calculations are closely following the work of E. Mathieson, who published his calculations on *Induced Charge Distributions in Proportional Detectors* [38] in 1990. First, the basic terminology and equations will be explained, followed by the calculation of the response of the ATLAS MDT and finally the calculation of the integrated MWPC in the test chamber setup that was built in this work. Terminology and structure of the following is taken from [38] as well as the pictures. Sometimes it will be necessary to skip longer calculations and derivations in order to keep the context clear. The full explanation can be found in the above mentioned work of E. Mathieson.

A.1.1. Basics and Terminology

Calculation of Induced Charge: The Reciprocity Method

The first method uses the reciprocity theorem to calculate the induced charge. A system of conductors is shown in figure A.1(a). Here, q_i is the charge on conductor i and V_i is the potential caused by the charge on conductor i. There is a linear relation between the q_i and the V_i. For example, for a point charge, the potential at a certain distance r_0 is

$$V_0(r_0) = q_0 \frac{1}{4\pi\varepsilon_0 r_0}. \tag{A.1}$$

With 3 conductors and no point charges, the system is more complicated, but can be expressed in a linear combination of a set of geometrical configuration coefficients c_{ij}:

$$q_i = \sum_{j=1}^{3} c_{ij} V_j. \tag{A.2}$$

In the following situation, suppose that charge q_1 is induced on conductor 1 by charge 2 on conductor 2, while all other conductors are grounded. The set of variables and potentials reduces to

$$q_1 = c_{12} V_2 \qquad \text{and} \qquad q_2 = c_{22} V_2, \tag{A.3}$$

(a) Setup of 3 conductors   (b) Parallel plate geometry
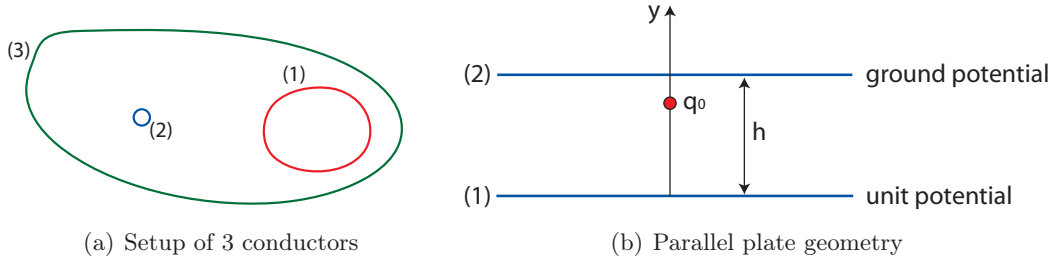
Figure A.1.: Two example setups to demonstrate the method of calculating induced charges. On the left a simple setup with three conductors and on the right an infinite parallel plate geometry with a charge q_0. Graphics after [38].

since $V_1 = V_3 = 0$. Then

$$V_2 = \frac{q_1}{c_{12}} = \frac{q_2}{c_{22}} \qquad \longrightarrow \qquad q_1 = q_2 \frac{c_{12}}{c_{22}}. \tag{A.4}$$

To get knowledge about c_{12}/c_{22}, another situation needs to be assumed: Conductor 1 is raised on unit potential, while conductor 2 is uncharged and isolated and conductor 3 ist on ground potential. Potential V_2 will raise to a value P. It follows

$$q_2 = c_{21}V_1 + c_{22}V_2 + c_{23}V_3 \qquad \longrightarrow \qquad 0 = c_{21} + c_{22}P, \tag{A.5}$$

since $V_1 = 1$, $V_2 = P$, $V_3 = 0$ and $q_2 = 0$. A property of the configuration coefficients is that because of Green's reciprocal theorem $c_{ij} = c_{ji}$. With

$$P = -\frac{c_{21}}{c_{22}} = -\frac{c_{12}}{c_{22}}, \tag{A.6}$$

we can recall equation A.4 and conclude that

$$q_1 = q_2 \frac{c_{12}}{c_{22}} = q_1 = q_2 P. \tag{A.7}$$

For drifting ions one can assume that conductor 2 is physically very small. A positive ion of charge q_2 may be regarded mathematically as conductor 2. To summarize, what has been stated so far:

A charge q_i that is induced on the surface of a conductor by a point charge q_0 at the location (x, y, z), can be expressed by

$$q_i = -q_0 P, \tag{A.8}$$

if P is the potential at the location (x, y, z), the conductor with q_i is on unit potential and all other conductors nearby are on ground potential.

Example: A conductor (1) is on unit potential. A second conductor (2) is parallel in distance h and on ground potential (figure A.1(b)). Then the potential $P(y)$ at the distance y is

$$P(y) = \frac{(h-y)}{h} = 1 - \frac{y}{h}. \tag{A.9}$$

Using A.8, the charge induced by a point charge q_0 at (x, y, z) is then

$$q_i = -q_0 P(y) = -q_0(1 - \frac{y}{h}). \tag{A.10}$$

The Surface Field Method

Although the method described above is quite simple, it cannot give the distribution of induced charges, but only their total number. A method that can calculate the induced charge distribution is the surface field method. It needs knowledge about the electric field E_N on the surface. Then the induced charge density is $\epsilon_0 E_N$.

Ion Trajectories

To know how the induced charge q_i will develop in time, it is necessary to know the trajectory of the inducing charge $q_0 = q_0(x(t), y(t))$. If $P_N(x, y)$ is the potential on electrode N, while all other electrodes are on ground potential, then the induced charge on N is

$$q_i = -q_0 P_N(x, y). \tag{A.11}$$

The trajectory $x(t)$, $y(t)$ of a charged particle is dependent on the derivative of $P(x, y)$, which is the potential at (x,y) due to all electrodes in the chamber (which is not the same as $P_N(x, y)$).

It is a good assumption that the ion mobility μ is usually constant with the velocity of the ion:

$$\mathbf{v} = \mu \mathbf{E}. \tag{A.12}$$

Here is $\mathbf{E}$ the electric field due to all voltages applied to the chamber. It can be easier to calculate the induced current i_i instead of the induced charge q_i. The induced current can be expressed as

$$i_i = -q_0 \frac{\mathrm{d}P_N}{\mathrm{d}t} = -q_0 \frac{\mathrm{d}P_N}{\mathrm{d}l} \frac{\mathrm{d}l}{\mathrm{d}t} = -q_0 \frac{\mathrm{d}P_N}{\mathrm{d}t} v. \tag{A.13}$$

Here, dl is a small increment in ion movement direction, which is the same as the direction of the surrounding field $\mathbf{E}$. Then

$$i_i = -q_0 \mu (\mathbf{E}_N \cdot \mathbf{E}), \tag{A.14}$$

with $\mathbf{E}_N = -\mathrm{grad}\, P_N$.

Induced Charge and Signal Charge

There is a difference between induced charge and signal charge, which is the observable charge in the connected electronics. The drawing in figure A.2 illustrates the following situation: The point charge q_0 induces the charge $-q_N$ on the surface of electrode N. Because of A.8, $q_i = -q_0 P_N$. The
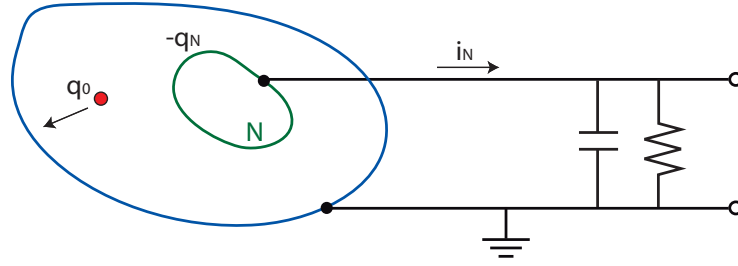
Figure A.2.: Charge q_0 induces charge $-q_N$ on conductor N resulting in a current i_N in the connected electric network [38].

signal charge outside the electrode system, but inside the electronics, is now exactly the opposite charge $-(-q_N) = q_N$. Following this terminology, the signal charge q_N and the signal current i_N are now:

$$q_N = q_0 P_N(x, y), \tag{A.15}$$

and

$$i_N = q_0 \frac{\mathrm{d}P_N}{\mathrm{d}t}. \tag{A.16}$$

The exact shape depends also on the further processing of the signal, such as capacitors and resistors in the entrance of the amplifier network. The anode in a proportional wire counter receives first a very quick bunch of negative electron charge coming out of the electron avalanche. This can be assumed to be a delta function. The drifting ions on their way away from the anode induce a second pulse with the same sign. The ion charge q_0 must be opposite sign to the electron charge, which is $-q_0$. Be A the anode of the system, then the anode signal charge is

$$q_a = -q_0 + q_A = -q_0(1 - P_A). \tag{A.17}$$

For the special geometry of a coaxial wire counter with only two electrodes, wire electrode A and enclosing electrode C, the equations are simply

$$q_a = -q_0 + q_A = -q_0(1 - P_A) \qquad \text{and} \qquad q_c = q_0 - q_A = q_0(1 - P_A) = -q_a. \tag{A.18}$$

A.1.2. Coaxial Geometry of a Wire Chamber

The coaxial geometry, as used for the MDT is a simple setup to apply these techniques and crosscheck with measurements from the MDT development.

Field, Potential and Capacitance

A coaxial wire chamber with anode radius r_a and cathode radius r_c is shown in figure A.3. The anode wire is at V_a, while the outer cylinder is on ground potential. Its lengths is large compared to its diameter, so that no boundary effects need to be taken into account. The electric field at a
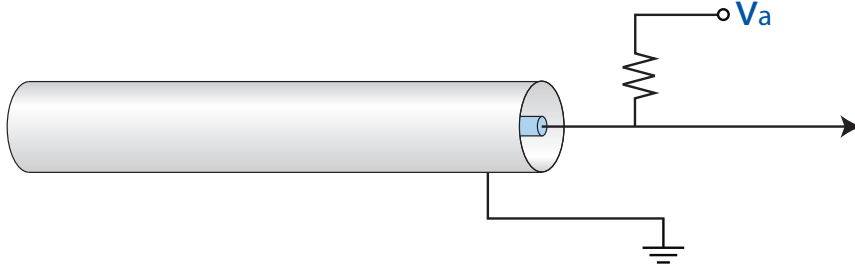
Figure A.3.: The setup of a simple wire tube [38]. The anode wire is on potential V_a while the outer cathode tube is grounded.

radius r can be calculated and expressed in terms of the capacitance, C. The electric flux ϕ can be calculated according to Gauss' law in this simple geometry as

$$\phi = \oint_A \vec{E} \, \mathrm{d}\vec{A} = \int_{surf} E(r) \, \mathrm{d}A = E(r) \int_{surf} \mathrm{d}A = E(r) \, 2\pi r \, l. \tag{A.19}$$

Since the flux is defined as $\phi = q/\varepsilon_0$, this leads to the formula for the electric field of the above geometry for $r > r_a$:

$$E(r) = \frac{q}{2\pi\varepsilon_0 l} \frac{1}{r}. \tag{A.20}$$

The potential at the outer cylinder is V_a. It is equal to the integral of the electric field between r_a and r_c:

$$V_a = \int_{r_a}^{r_c} E(r) \, \mathrm{d}r = \frac{q}{2\pi\varepsilon_0 l} \ln \frac{r_c}{r_a} = \frac{q}{4\pi\varepsilon_0 l} \ln \left(\frac{r_c}{r_a}\right)^2. \tag{A.21}$$

The potential is also $V_a = q/C$, which leads to the value for the real capacitance C of the system:

$$C = \frac{4\pi\varepsilon_0 l}{\ln (r_c/r_a)^2}. \tag{A.22}$$

Now define a special capacity per unit length C^*:

$$C^* = \frac{1}{\ln (r_c/r_a)^2} = \frac{C}{4\pi\varepsilon_0 l}. \tag{A.23}$$

The electric field in equation A.20 can also be expressed in terms of the new variable C^*, with $q = C V_a$:

$$E(r) = \frac{C V_a}{2\pi\varepsilon_0 l} \frac{1}{r} = \frac{C}{4\pi\varepsilon_0 l} 2V_a \frac{1}{r} = 2C^* V_a \frac{1}{r} \tag{A.24}$$

Now the potential $P(r)$ at a certain radius r inside the cathode can be calculated by integration of E:

$$P(r) = \int_r^{r_c} E(r) \, \mathrm{d}r = \int_r^{r_c} \frac{2C^* V_a}{r} \, \mathrm{d}r = 2C^* V_a \ln \left(\frac{r_c}{r}\right)^2. \tag{A.25}$$

Using the definition of the special capacity per unit length from equation A.23 in the last step, this can be written as follows:

$$P(r) = -C^* V_a \ln\left(\frac{r}{r_c}\right)^2 = -C^* V_a \ln\left(\frac{r}{r_a}\right)^2 + C^* V_a \ln\left(\frac{r_c}{r_a}\right)^2 = V_a \left(1 - C^* \ln\left(\frac{r}{r_a}\right)^2\right).$$

(A.26)

Anode Induced and Net Charges

Now assume that the anode is on unit potential while the cathode is grounded. Then A.26 gives the potential P_A:

$$P_A = 1 - C^* \ln\left(\frac{r}{r_a}\right)^2.$$

(A.27)

A positive point charge q_0 created in the avalanche being now at a distance r from the wire results in a potential on the wire that is given by equation A.8

$$-q_A = -q_0 \left(1 - C^* \ln\left(\frac{r}{r_a}\right)^2\right).$$

(A.28)

From equations A.18 follows for the net charges

$$q_a = -q_0 + q_A = -q_0 C^* \ln\left(\frac{r}{r_a}\right)^2 \qquad \text{and} \qquad q_c = -q_a = q_0 C^* \ln\left(\frac{r}{r_a}\right)^2.$$

(A.29)

Time Development of Anode Charge

The ions are drifting away from the wire in a radial direction with a velocity of $v = \mu E$. Using E from equation A.20 it can be written as

$$|\vec{v}| = \frac{dr}{dt} = \mu |\vec{E}| = \mu 2 C^* \frac{V_a}{r}.$$

(A.30)

Separation of the variables r on the left and t on the right side of the equation leads to

$$\int_{ra}^{r} r dr = \mu 2 C^* V_a t \qquad \longleftrightarrow \qquad \frac{r^2}{r_a^2} = 1 + \frac{4\mu C^* V_a}{r_a^2} t$$

(A.31)

which can be further simplified to

$$\frac{r^2}{r_a^2} = 1 + \frac{t}{t_0} \qquad \text{with} \qquad t_0 = \frac{r_a^2}{4\mu C^* V_a}.$$

(A.32)

For the net charge follows that

$$q_a(t) = -q_0 C^* \ln\left(1 + t/t_0\right).$$

(A.33)

For the ion collection time t_c follows that

$$\frac{t_c}{t_0} = \frac{r_c^2}{r_a^2} - 1.$$

(A.34)
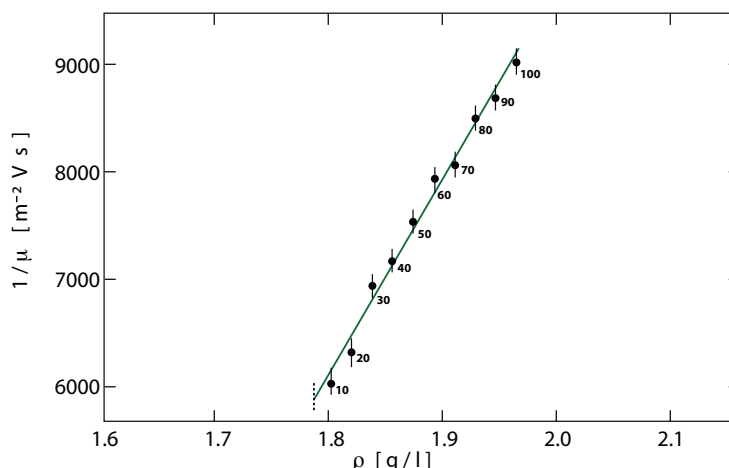
Figure A.4.: Ion mobility μ as a function of the density and the CO_2 content in $ArCO_2$, after [44].

The collection time might be very long compared to the signal rise time and strongly depends on the geometry and the size of the chamber. This is the reason, why especially at high detection rates, a remarkably high number of ions can build up a positive space charge and disturb the function of the detector.

ATLAS MDT Timing Constant Comparison to Measurement

During development and assembly, the ATLAS MDTs have been measured and tested. The characteristic counter time of the signal rise t_0 has been measured by Viola Rehmann in her diploma thesis [43] to be $t_0 = 10.8\,\text{ns} \pm 1\,\text{ns}$. With $r_c = 15\,\text{mm}$, $r_a = 0.025\,\text{mm}$ and $V_a = 3080\,\text{V}$ and the equations for t_0 and C^* follows

$$t_0 = \frac{r_a^2}{4\mu C^* V_a} \qquad \text{and} \qquad C^* = \frac{1}{\ln{(r_c/r_a)^2}} = 0.078 \pm 0.004. \tag{A.35}$$

The characteristic counter time can be calculated to be $t_0 = (11.66 \pm 1.2)\,\text{ns}$, assuming an ion mobility of about $1.67 \times 10^4\,\text{m}^2\,\text{bar}\,\text{V}^{-1}\,\text{s}^{-1}$ in a gas mixture of $ArCO_2$ 93 %/7 % [44]. This value is in a good agreement within the errors with the value measured during assembly of the MDTs.

A.1.3. Response Function of the Integrated MWPC: Reference Readout System

The calculations for a multiwire proportional chamber (MWPC) are more complicated, since the electric field is not strictly radial like for a cylindrical wire tube, but has a parallel form near the cathodes. In the anode region close to the wires the field will be radial, if the anode radius $r_a \ll s$ and the cathode spacing h fulfills the relation $\cosh{(2\pi h/s)} \gg 1$ (Weber approximation), with s being the wires pitch. The geometry of this setup is shown in figure A.5(a).

This approximation is useful to calculate potentials, fields and signal timings for a simple MWPC geometry. For more complicated geometries a more general approach is necessary, which

is described in detail in [38].

Potential Distribution for MWPC

Assuming that the anode is on unit potential and both cathodes are grounded (symmetrical setup, $r_a \ll s$ and $\cosh(2\pi h/s) \gg 1$), it is possible to find a formula for the potential distribution in the chamber.

Starting with a complex function for the potential $W(z)$, with constants K, E_0 and V_0 one gets

$$W(z) = -K \ln\{\sin(\pi z/s)\} - iE_0 z + V_0. \tag{A.36}$$

Like every complex function, this can be split into imaginary and real part of the function: $W(z) = P(x,y) + i\,Q(x,y)$. Real and imaginary parts are only mixed in the first term:

$$\ln\left\{\sin\left(\frac{\pi z}{s}\right)\right\} = \ln\left\{\sin\left(\frac{\pi x}{s} + i\frac{\pi y}{s}\right)\right\}. \tag{A.37}$$

Now substitute for the following calculations $\frac{\pi x}{s} = x'$ and $\frac{\pi y}{s} = y'$.

$$
\begin{aligned}
\ln\left\{\sin\left(x' + iy'\right)\right\} &= \frac{1}{2}\ln\left\{\sin^2\left(x' + iy'\right)\right\} \\
&= \frac{1}{2}\ln\left\{\sin\left(x' + iy'\right) \cdot \sin\left(x' - iy'\right) \cdot \frac{\sin\left(x' + iy'\right)}{\sin\left(x' - iy'\right)}\right\} \\
&= \frac{1}{2}\ln\left\{\left(\sin^2(x') - \sin^2(iy')\right) \cdot \frac{\sin(x')\cos(iy') + \sin(iy')\cos(x')}{\sin(x')\cos(iy') - \sin(iy')\cos(x')}\right\} \\
&= \frac{1}{2}\ln\left\{\frac{1}{2}\left(2\sin^2(x') - 2\sin^2(iy')\right) \cdot \frac{\frac{\sin(x')\cos(iy') + \sin(iy')\cos(x')}{\cos(x')\cos(iy')}}{\frac{\sin(x')\cos(iy') - \sin(iy')\cos(x')}{\cos(x)\cos(iy')}}\right\} \\
&= \frac{1}{2}\ln\left\{\frac{1}{2}\left(1 - 2\sin^2(iy') - \left[1 - 2\sin^2(iy')\right]\right) \cdot \frac{\frac{\sin(x')}{\cos(x')} + \frac{\sin(iy')}{\cos(iy')}}{\frac{\sin(x')}{\cos(x')} - \frac{\sin(iy')}{\cos(iy')}}\right\} \\
&= \frac{1}{2}\ln\left\{\frac{1}{2}\left(\cos(2iy') - \cos(2x')\right) \cdot \frac{\tan(x') + \tan(iy')}{\tan(x') - \tan(iy')}\right\} \\
&= \frac{1}{2}\ln\left\{\frac{1}{2}\left(\cosh(2y') - \cos(2x')\right) \cdot \frac{1 + \frac{\tan(iy')}{\tan(x')}}{1 - \frac{\tan(iy')}{\tan(x')}}\right\}
\end{aligned}
\tag{A.38}
$$

With $\tan(iy') = i\tanh(y')$ and $\tan\beta = \frac{\tanh(y')}{\tan(x')}$ this can be written as

$$
\begin{aligned}
&= \frac{1}{2}\ln\left\{\frac{1}{2}\left(\cosh(2y') - \cos(2x')\right)\right\} + \frac{1}{2}\ln\left\{\frac{1 + i\tan\beta}{1 - i\tan\beta}\right\} \\
&= \frac{1}{2}\ln\left\{\frac{1}{2}\left(\cosh(2y') - \cos(2x')\right)\right\} + i\,\frac{\ln(1 + i\tan\beta) - \ln(1 - i\tan\beta)}{2i} \\
&= \frac{1}{2}\ln\left\{\frac{1}{2}\left(\cosh(2y') - \cos(2x')\right)\right\} + i\arctan(\tan\beta)
\end{aligned}
\tag{A.39}
$$

(a) MWPC geometry

(b) Field lines in the close wire proximity and detector body zone
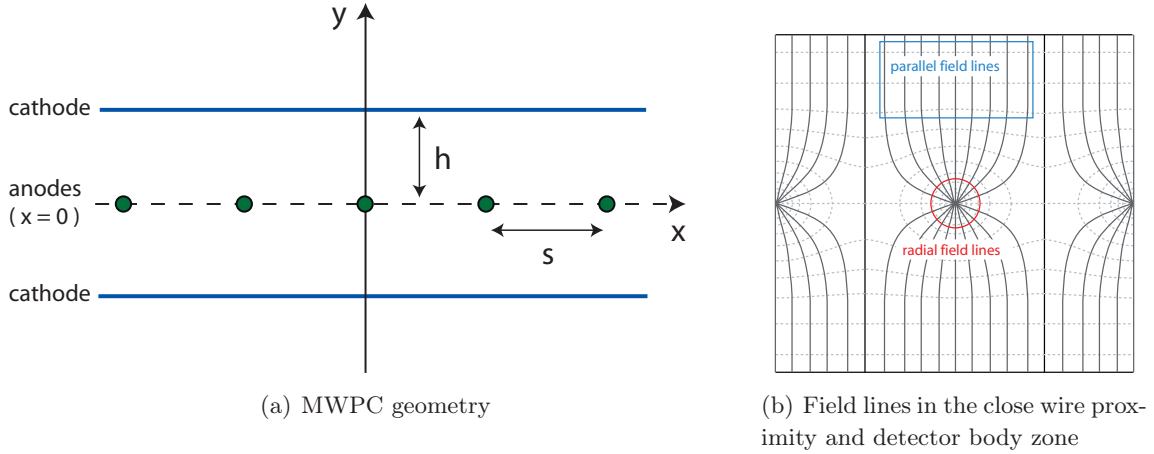
Figure A.5.: This typical geometry is used for most MWPC (left, [38]). The definition of the two zones where the approximations are valid: Near the wire the electric field is radial while in the detector middle parallel field lines can be found.

Resubstitution of $\frac{\pi x}{s} = x'$ and $\frac{\pi y}{s} = y'$ leads to

$$\ln \left\{ \sin \left(\frac{\pi z}{s} \right) \right\} = \frac{1}{2} \ln \left\{ \frac{1}{2} \left(\cosh \left(2\frac{\pi y}{s} \right) - \cos \left(2\frac{\pi x}{s} \right) \right) \right\} + i \beta \qquad (A.40)$$

Real and imaginary part of the function $W(z)$ are now separated and $P(x,y)$ and $Q(x,y)$ can be identified as

$$P(x,y) = -K \ln \left\{ \frac{1}{2} \left(\cosh \left(2\frac{\pi y}{s} \right) - \cos \left(2\frac{\pi x}{s} \right) \right) \right\}^{\frac{1}{2}} + E_0 y + V_0 \qquad (A.41)$$

$$Q(x,y) = -K\, \beta - E_0 x. \qquad (A.42)$$

The curly bracket in equation A.42 in the close wire proximity under the condition $y/s \to 0$ and $x''/s \to 0$ ($x'' = x - ns$, at every wire position n) can be simplified:

$$\left\{ \frac{1}{2} \left(\cosh \left(2\frac{\pi y}{s} \right) - \cos \left(2\frac{\pi x''}{s} \right) \right) \right\}^{\frac{1}{2}} = \left\{ \frac{1}{4} \left(e^{2\pi y/s} + e^{-2\pi y/s} - e^{i\,2\pi x''/s} - e^{-i\,2\pi x''/s} \right) \right\}^{\frac{1}{2}}. \qquad (A.43)$$

This can be simplified even further with the series expansion for e^x: $e^x = \sum_{n=0}^{\infty} = \frac{x^n}{n!} = 1 + x + \frac{1}{2!} x^2 + ...$, where only the first three summands up to the quadratic term are used:

$$\left\{ \frac{1}{4} \left(\left(\frac{2\pi y}{s} \right)^2 + \left(\frac{2\pi x''}{s} \right)^2 \right) \right\}^{\frac{1}{2}} = \frac{\pi}{s} \left(x''^2 + y^2 \right)^{\frac{1}{2}}. \qquad (A.44)$$

With $r = \left(x''^2 + y^2\right)^{\frac{1}{2}}$ and assuming $y/s \to 0$ and $x''/s \to 0$ $(x'' = x - ns)$ it follows

$$\left\{\frac{1}{2}\left(\cosh\left(2\frac{\pi y}{s}\right) - \cos\left(2\frac{\pi x''}{s}\right)\right)\right\}^{\frac{1}{2}} \to \frac{\pi r}{s}. \tag{A.45}$$

Far from the anode wire, this approximation cannot be made, but in regions where $\cosh\left(2\pi h/s\right) \gg 1$ holds, the curly bracket of A.42 can be approximated in a different way:

$$\left\{\frac{1}{2}\left(\cosh\left(2\frac{\pi y}{s}\right) - \cos\left(2\frac{\pi x}{s}\right)\right)\right\}^{\frac{1}{2}} = \frac{1}{2}\left[\ln\left\{\cosh\left(\frac{2\pi y}{s}\right) \cdot \frac{1}{2} \cdot \left(1 - \frac{\cos\left(\frac{2\pi x}{s}\right)}{\cosh\left(\frac{2\pi y}{s}\right)}\right)\right\}\right]. \tag{A.46}$$

Since $\cosh\left(2\pi h/s\right) \gg 1$, the last bracket can be considered to be close to 1.

$$\approx \frac{1}{2}\left[\ln\frac{1}{2} + \ln\left\{\frac{1}{2}\left(e^{\frac{2\pi y}{s}} + e^{\frac{-2\pi y}{s}}\right)\right\}\right] \tag{A.47}$$

The e-functions can be simplified to $e^{\frac{2\pi|y|}{s}}$, because for large positive values of y, the $e^{\frac{-2\pi y}{s}}$ is negligible and for large negative values of y the $e^{\frac{2\pi y}{s}}$ term is approximately

$$\approx \frac{1}{2}\left[-\ln 2 + \ln\left\{\frac{1}{2} e^{\frac{2\pi|y|}{s}}\right\}\right] = \frac{1}{2}\left[-2\ln 2 + \frac{2\pi|y|}{s}\right] = \frac{\pi}{s}|y| - \ln 2 \tag{A.48}$$

Finally using the definition of the effective cathode radius $r_c = \left(\frac{s}{2\pi}\right) \cdot e^{\frac{\pi h}{s}}$, this can be written as

$$\begin{aligned}
\frac{\pi}{s}|y| - \ln 2 &= -\ln 2 + \frac{\pi h}{s} - \frac{\pi h}{s} + \frac{|y|}{h}\frac{\pi h}{s} \\
&= \ln\left(\frac{\pi}{s}\frac{s}{2\pi} e^{\frac{\pi h}{s}}\right) - \left(1 - \frac{|y|}{h}\right)\frac{\pi h}{s} \\
&= \ln\left(\frac{\pi r_c}{s}\right) - \left(1 - \frac{|y|}{h}\right)\frac{\pi h}{s}.
\end{aligned} \tag{A.49}$$

It is now possible to determine the constants K, E_0 and V_0. The anode is at unit potential and the cathodes are grounded. This results in the following equations:

$$\begin{aligned}
\text{at} \quad y = h: \quad & W(z) = 0\,\forall\,x \quad &\to\quad & 0 = -K\ln\left(\frac{\pi r_c}{s}\right) + E_0 h + V_0 \\
\text{at} \quad r = r_a: \quad & W(z) = 1\,\forall\,x,y \quad &\to\quad & 1 = -K\ln\left(\frac{\pi r_a}{s}\right) + V_0 \\
\text{at} \quad y = -h: \quad & W(z) = 0\,\forall\,x \quad &\to\quad & 0 = -K\ln\left(\frac{\pi r_c}{s}\right) - E_0 h + V_0.
\end{aligned} \tag{A.50}$$

Therefore we can conclude that

$$\begin{aligned}
E_0 h &= -E_0 h \quad &\to\quad & E_0 = 0 \\
V_0 &= K\ln\left(\frac{\pi r_c}{s}\right) \\
K &= 1/\ln\left(\frac{r_c}{r_a}\right).
\end{aligned} \tag{A.51}$$

For the dimensionless quantity C^* follows:

$$C^* = 1/\ln \left(\frac{r_c}{r_a}\right)^2 \qquad \rightarrow \qquad K = 2C^*. \tag{A.52}$$

With these constants the potential $P(x, y)$ can finally be written as

$$\begin{aligned}
P(x, y) &= -K \ln \left\{\frac{1}{2}\left(\cosh\left(2\frac{\pi y}{s}\right) - \cos\left(2\frac{\pi x}{s}\right)\right)\right\}^{\frac{1}{2}} + E_0 y + V_0 \\
&= -2C^* \ln \left\{\frac{1}{2}\left(\cosh\left(2\frac{\pi y}{s}\right) - \cos\left(2\frac{\pi x}{s}\right)\right)\right\}^{\frac{1}{2}} + K \ln \left(\frac{\pi r_c}{s}\right) \\
&= -C^* \ln \left\{\frac{1}{2}\left(\cosh\left(2\frac{\pi y}{s}\right) - \cos\left(2\frac{\pi x}{s}\right)\right)\right\} + \frac{\ln\left(\frac{r_c}{r_a}\frac{\pi r_a}{s}\right)}{\ln\left(\frac{r_c}{r_a}\right)} \\
&= -C^* \ln \left\{\frac{1}{2}\left(\cosh\left(2\frac{\pi y}{s}\right) - \cos\left(2\frac{\pi x}{s}\right)\right)\right\} + \ln\left(\frac{\pi r_a}{s}\right) \cdot 2C^* + 1 \\
&= 1 - C^* \ln \left\{\frac{2\left(\cosh\left(2\frac{\pi y}{s}\right) - \cos\left(2\frac{\pi x}{s}\right)\right)}{\left(2\frac{\pi r_a}{s}\right)^2}\right\}.
\end{aligned} \tag{A.53}$$

Close to the anode wire this potential function reduces to the simple coaxial form, as expected. From equation A.45 follows

$$\frac{1}{2}\left(\cosh\left(2\frac{\pi y}{s}\right) - \cos\left(2\frac{\pi x}{s}\right)\right) \rightarrow \frac{\pi^2 r^2}{s^2}, \tag{A.54}$$

and the potential is simply

$$\begin{aligned}
P(x, y) &= 1 - C^* \cdot \ln\left(\frac{\pi^2 r^2}{s^2}\frac{s^2}{\pi^2 r_a^2}\right) \\
&= 1 - C^* \cdot \ln\left(\frac{r}{r_a}\right)^2.
\end{aligned} \tag{A.55}$$

In the body of the chamber, where $\cosh(2\pi h/s) \gg 1$, the potential gets the following form using equation A.49:

$$\begin{aligned}
P(x, y) &= 1 - 2C^* \ln\left\{\frac{1}{2}\left(\cosh\left(2\frac{\pi y}{s}\right) - \cos\left(2\frac{\pi x}{s}\right)\right)\right\}^{\frac{1}{2}} + 2C^* \ln\left(\frac{\pi r_a}{s}\right) \\
&= 1 - 2C^* \ln\left(\frac{\pi r_c}{s}\right) + 2C^* \ln\left(\frac{\pi r_a}{s}\right) + 2C^*\left(1 - \frac{|y|}{h}\right)\frac{\pi h}{s} \\
&= 2C^* \frac{\pi h}{s}\left(1 - \frac{|y|}{h}\right)
\end{aligned} \tag{A.56}$$

The flux function $Q(x, y)$ in equation A.42 gets this form:

$$Q(x, y) = -K\beta - E_0 x = -2C^* \tan^{-1}\left(\frac{\tanh\left(\frac{\pi y}{s}\right)}{\tan\left(\frac{\pi x}{s}\right)}\right), \tag{A.57}$$

using $K = 2C$ and $E_0 = 0$.

Field Lines for MWPC

The expression $Q = \text{constant}$ defines a field line in the chamber. The angle, at which they meet the anode wire surface, is called α. For very small values of y/s and $(x'' - ns)/s$ in the very close proximity of the anode wire is $\alpha = y/x''$. For the flux function this results in

$$Q(x, y) = -2C^* \tan^{-1} \left(\frac{\tanh \left(\frac{\pi y}{s} \right)}{\tan \left(\frac{\pi x}{s} \right)} \right) \approx -2C^* \alpha, \tag{A.58}$$

because $y = \alpha\, x$, $\frac{\tanh \left(\frac{\alpha \pi x}{s} \right)}{\tan \left(\frac{\pi x}{s} \right)} \approx \frac{\alpha \pi x}{s} / \frac{\pi x}{s} \approx \alpha$ and $\tan^{-1} \alpha \approx \alpha$, and therefore

$$\tan \alpha = \frac{\tanh \left(\frac{\pi y}{s} \right)}{\tan \left(\frac{\pi x}{s} \right)}. \tag{A.59}$$

The field lines are therefore described by the family of curves with the following properties:

$$\tanh \left(\frac{\pi y}{s} \right) = \tan \alpha \cdot \tan \left(\frac{\pi x}{s} \right). \tag{A.60}$$

Electric Fields for MWPC

The fields can be obtained from the potential by partial differentiation of the potential function $P(x, y)$. The anode wire is at V_a, the cathodes are grounded:

$$E_x = -V_a \frac{\partial P}{\partial x} = 2C^* V_a \frac{\pi}{s} \frac{\sinh \left(\frac{2\pi x}{s} \right)}{\cosh \left(\frac{2\pi y}{s} \right) \cos \left(\frac{2\pi x}{s} \right)} \tag{A.61}$$

$$E_y = -V_a \frac{\partial P}{\partial y} = 2C^* V_a \frac{\pi}{s} \frac{\sinh \left(\frac{2\pi y}{s} \right)}{\cosh \left(\frac{2\pi y}{s} \right) \cos \left(\frac{2\pi x}{s} \right)}. \tag{A.62}$$

Using $E = \sqrt{E_x^2 + E_y^2}$ the resulting field is:

$$E = 2C^* V_a \frac{\pi}{s} \left(\frac{\cosh \left(\frac{2\pi y}{s} \right) + \cos \left(\frac{2\pi x}{s} \right)}{\cosh \left(\frac{2\pi y}{s} \right) - \cos \left(\frac{2\pi x}{s} \right)} \right)^{\frac{1}{2}} \tag{A.63}$$

In the two cases, the very close anode area, where the field is mostly radial and the chamber body, where it is mostly parallel, the field reduces to:

$$\text{near anode}: \quad x, y \ll s \quad E = 2C^* V_a \frac{1}{r} \quad \text{coaxial field} \tag{A.64}$$

$$\text{near cathode}: \quad \cosh \left(2\pi h/s \right) \gg 1 \quad E_x = 0,\ E_y = \pm 2\pi C^* V_a \frac{1}{s} \quad \text{uniform field} \tag{A.65}$$

Ion Collection Time for MWPC

The average ion collection time can be calculated independently from the Weber approximation. The timings of the charge movements are helpful to find the signal forms of the MWPC.

The average ion collection time is dependent on the geometry of the chamber, as well as on the ion mobility μ, the dimensionless wire capacity C^* and the wire potential V_a:

$$t_{av} = \frac{hs}{2\pi\mu C V_a} = T_0 \frac{h/s}{2\pi C^*}, \tag{A.66}$$

with $T_0 = s^2/\mu V_a$. The detailed derivation can be found in [38].

Anode Charge Waveform for MWPC

In the coaxial field region of the wire anode, the ions that are produced in the avalanche processes move radially away from the wire. With equations A.33 and A.52, the anode waveform can be expressed directly:

$$q_a(t) = -q_0 \, C^* \ln\left(1 + t/t_0\right), \tag{A.67}$$

with $C^* = 1/\ln\left(\frac{r_c}{r_a}\right)^2$, $r_c = \left(\frac{s}{2\pi}\right) \mathrm{e}^{\pi h/s}$ and $t_0 = \frac{r_a^2}{4\mu C^* V_a}$. This is a suitable approximation for most symmetrical MWPC geometries and usually true below one microsecond drift time, which covers most of the chambers and wave forms, because the integration time of the amplifiers is usually less than this time span.

Application of the Formulae for MWPC to Reference System

To calculate potentials, fields and the ion collection time, the geometry, wire potential V_a and the ion mobility μ must be known. The reference system inside the MPGD test chamber is essentially a MWPC. It is not exactly symmetrical, but because of the chosen distances and potentials, the field in the close wire region is symmetric and the field strength of the upper and lower body regions are identical. The wire radius is $25\,\mu$m and therefore much less than the wire spacing s with $6\,$mm. Also the relation $\cosh\left(2\pi h/s\right) \gg 1$ is true, since $\cosh\left(2\pi h/s\right) = 3.6 \times 10^5$ for this chamber.

Therefore, the above calculation and approximation can be applied to this special problem.

The geometry of the chamber can be summarized by table A.1.

Now the theoretical cathode radius $r_c = \left(\frac{s}{2\pi}\right)\mathrm{e}^{\pi h/s}$ can be calculated:

$$r_c = \frac{0.006\,\mathrm{m}}{2\pi} \cdot \mathrm{e}^{\frac{\pi \cdot 12.9mm}{6mm}} = (0.82 \pm 0.09)\,\mathrm{m}. \tag{A.68}$$

The dimensionless capacity C^* is then

$$C^* = 1/\ln\left(\frac{r_c}{r_a}\right)^2 = 1/\ln\left(\frac{0.82\,\mathrm{m}}{2.5 \times 10^{-5}\,\mathrm{m}}\right)^2 = 0.048 \pm 0.003, \tag{A.69}$$

which results in a value t_0:

$$t_0 = \frac{r_a^2}{4\mu C^* V_a} = (5.0 \pm 0.5)\,\mathrm{ns}. \tag{A.70}$$

Table A.1.: Technical specifications for the reference readout system inside the MPGD test chamber.

wire radius / anode radius	r_a	$(25 \pm 1)\,\mu\mathrm{m}$
wire pitch	s	$(6.0 \pm 0.1)\,\mathrm{mm}$
distance anode/cathode	h	$(12.9 \pm 0.1)\,\mathrm{mm}$
wire potential	V_a	$(3900 \pm 20)\,\mathrm{V}$
gas composition	$\mathrm{ArCO_2}$	$93\,\% \ / \ 7\,\%$
gas pressure	p	$(1.10 \pm 0.02)\,\mathrm{bar}$
ion mobility	μ	$\approx (1.67 \pm 0.05) \times 10^{-4}\,\mathrm{m^2 bar\,V^{-1}s^{-1}}$

The average ion collection time t_{av} is

$$t_{av} = \frac{hs}{2\pi\mu C^* V_a} = (4.0\,s \pm 0.3) \times 10^{-4}\,\mathrm{s}. \tag{A.71}$$

The ion charge waveform for the reference system has been calculated accordingly to be

$$q_a(t) = -q_0\,C^* \ln\left(1 + t/t_0\right) = -q_0 \cdot (0.048 \pm 0.003) \cdot \ln\left(1 + t/(5.0 \pm 0.5)\,\mathrm{ns}\right), \tag{A.72}$$

The current is

$$i_a = \frac{\mathrm{d}q_a(t)}{\mathrm{d}t} = -q_0 \cdot (0.048 \pm 0.003) \cdot \frac{1}{(5.0 \pm 0.5)\,\mathrm{ns} + t}. \tag{A.73}$$

A.2. Noise Filter Calculation

To eliminate or reduce unwanted frequencies disturbing the measurements that are not triggered by the laser itself, a filter has been designed and built according to the scheme in figure A.6. It is a conventional low pass filter with a capacitance C and an inductance L, but the power supply with its input resistance R draws a non-negligible current I_i from the system, which is in the range of $1\,\mathrm{A}$, since the power supply is providing the voltages for all 34 VV30 amplifiers at a time.

The ratio that gives a measure for the attenuation of a given frequency ω in the input voltage U_i is $U_e(\omega)/U_i$. In this case it can be written as

$$\frac{U_e(\omega)}{U_i} = \frac{U_i - U_L}{U_i} = 1 - \frac{U_L}{U_i} = 1 - \frac{I_i \cdot R_L}{U_i} = 1 - \frac{\omega L}{R_i} = 1 - \frac{\omega L}{|Z_i|}. \tag{A.74}$$

The complex impedance Z_i of the input part of the system is:

$$\begin{aligned}
Z_i &= i\omega L + \frac{1}{1/R + i\omega C} = i\omega L + \frac{R}{1 + i\omega CR} \\
&= i\omega L + \frac{R(1 - i\omega CR)}{(1 + i\omega CR)(1 - i\omega CR)} = \frac{R}{1 + \omega^2 C^2 R^2} + i\left(\omega L - \frac{\omega C R^2}{1 + \omega^2 C^2 R^2}\right) \\
&= \mathrm{Re}(Z_i) + i\,\mathrm{Im}(Z_i)
\end{aligned} \tag{A.75}$$
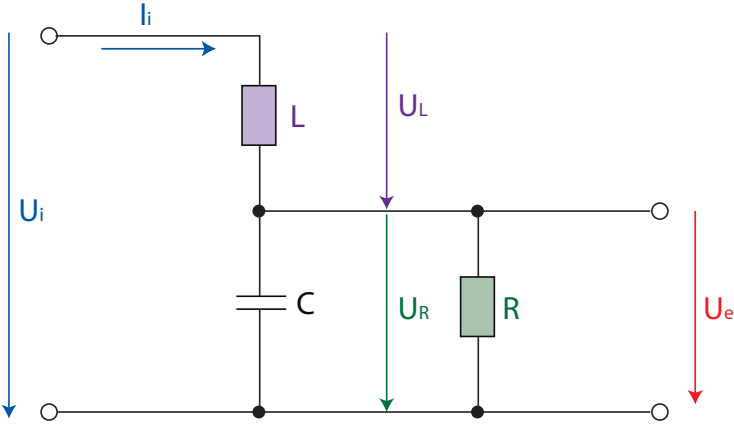
Figure A.6.: Electric scheme for a low pass filter for the VV30 amplifier power supply.

With $|Z_i| = \sqrt{\text{Re}(Z_i)^2 + \text{Im}(Z_i)^2}$, this can be calculated as

$$
\begin{aligned}
|Z_i| &= \sqrt{\frac{R^2}{(1+\omega^2 C^2 R^2)^2} + \left(\omega L - \frac{\omega C R^2}{1+\omega^2 C^2 R^2}\right)^2} \\
&= \sqrt{\frac{R^2(1+\omega^2 C^2 R^2)}{(1+\omega^2 C^2 R^2)^2} + \omega^2 L^2 - \frac{2\omega^2 L C R^2}{1+\omega^2 C^2 R^2}} \\
&= \sqrt{\frac{R^2 - 2\omega^2 L C R^2}{(1+\omega^2 C^2 R^2)} + \omega^2 L^2}
\end{aligned}
\tag{A.76}
$$

In the limits of $R \to 0$ and $R \to \infty$ this results in $Z_i = \omega L$ and $Z_i = \sqrt{\frac{1-2\omega^2 L C}{\omega^2 C^2}} = 1/\omega C - \omega L$, respectively.

For a constant current of about $1\,\text{A}$ it is not trivial to choose the correct type of inductivity L and capacitance C. For the capacitance, usually the electrolytic capacitors have the highest possible values, but they are also very slow at high frequencies. Therefore, ceramic capacitors would be the choice for this type of application, but they are only available up to about $100\,\mu\text{F}$. A similar situation exists for the inductivity. Suited for the application are air-core inductances, but they are huge and only available up to about $120\,\text{mH}$ at the usual stores.

Figure A.7 visualizes the attenuation as a function of the noise signal frequency ω. The values of the different simulated combinations start at $C = 20\,\mu\text{F}$ with $L = 4\,\text{mH}$ and increase exponentially to $C = 10\,\text{F}$ with $L = 2\,\text{H}$.

The low pass filter with the values $C = 600\,\mu\text{F}$ and $L = 120\,\text{mH}$ has been tested, but due to the needed high current of about $1\,\text{A}$, the cut frequency is too high to filter the noise pulses completely. To reach acceptable suppression levels of about $90\,\%$, capacitances and inductances of several Farad and Henry would be needed, which are not available for this high current.

Although the filter is not able to eliminate the noise induced by the randomly occurring signal completely, it still improves the overall quality of the signal visibly, especially in the higher frequencies. Therefore, it is used during the following measurements.
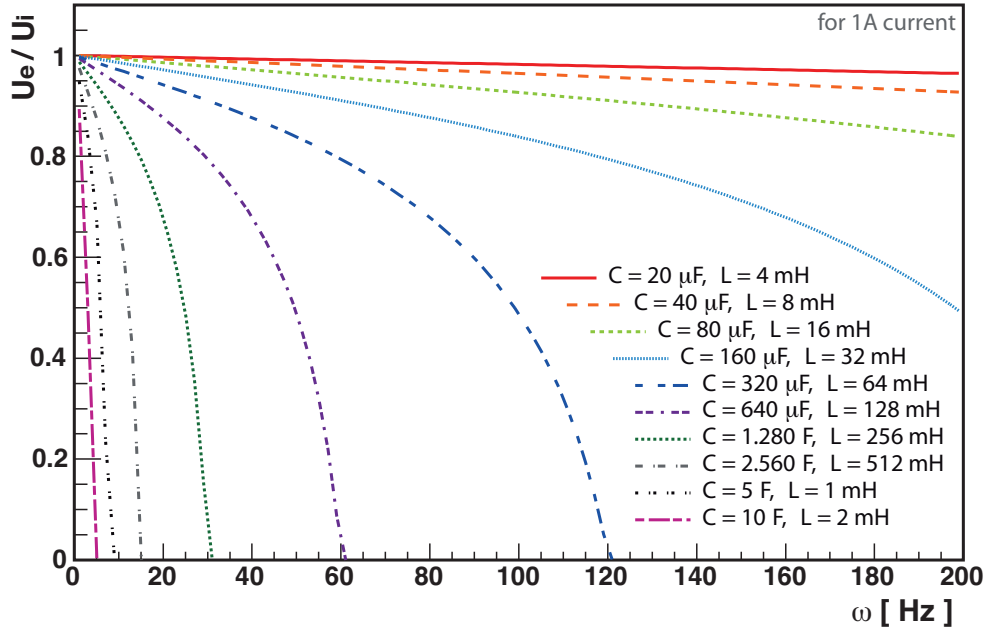
Figure A.7.: Simulation of suppression of noise in the VV30 amplifier power supply with different combinations of L and C.

A.3. Pressure Calculation Using the Atmospheric Pressure

To find the correct absolute chamber pressure without using the imprecise absolut pressure sensors of the pressure regulation system, an independent measurement has been carried out. It is using only the weather station on the chemical high rise building close by, a clear plastic tube and inked water. The setup is shown in figure A.8. The pressure of the chamber p_{ch} causes the water in the tube to rise, until the weight of the water column F_g compensates the difference between the outside pressure p_{out} and the chamber pressure:

$$p_{ch} = p_{out} + p_w. \tag{A.77}$$

The pressure p_w of the water column can be calculated by

$$p_w = \frac{F_g}{A_t}. \tag{A.78}$$

The water surface A_t in the tube can be eliminated using $F_g = m_w \cdot g$ and $m_w = \rho_w \cdot A_t \cdot h$, with h being the height of the water column and ρ_w, the mass density of water, assumed to be equal 1:

$$p_w = \frac{m_w \cdot g}{A_t} = \frac{\rho_w \cdot A_t \cdot h \cdot g}{A_t} = h \cdot g. \tag{A.79}$$

The height difference h of the water column and the outside pressure p_{out} need to be determined. The heights of the water columns are (177.2 ± 0.1) cm and (82.6 ± 0.1) cm, which results in a
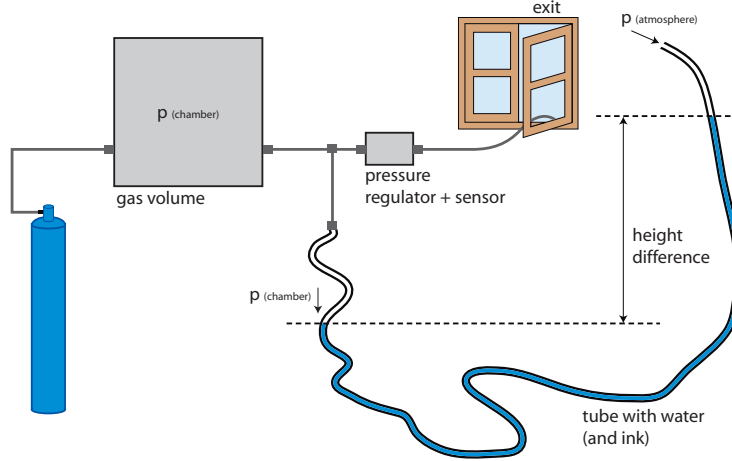
Figure A.8.: Setup for absolute pressure measurement of the chamber pressure.

difference $h = (94.6 \pm 0.2)$. The corresponding pressure of the water column is then $p_w = (92.8 \pm 0.2)\,$mbar. While the height difference can easily be measured with a meter, the determination of the outside pressure needs additional research.

The weather station of the university [45], located on a high rise building about $150\,$m away, measures the whole spectrum of meteorological data, including the air pressure. This is measured at a height of $(323.5 \pm 0.1)\,$m above sea level. The floor of the laboratory is at $(277.06 \pm 0.05)\,$m above sea level according to the architect's plan of the building. The upper level of the water column was positioned at $(177.2 \pm 0.5)\,$cm height in the lab. Therefore the the air pressure $(44.67 \pm 0.05)\,$m below the measuring point on top of the high rise building can be calculated. To calculate the pressure in the lab in relation to the value obtained by the weather station, the classic barometric formula [46] can be used, because temperature and gravitation are constants in these small height differences:

$$p(h1) = p(ho) \cdot \mathrm{e}^{-\frac{m \cdot g}{R \cdot T} \cdot \Delta h}. \tag{A.80}$$

With $M = 0.02897\,$kg·mol^{-1} [47] being the mean molecular mass of the atmosphere gas components, $g = 9.80665\,$m·s^{-1} the acceleration of gravity, $R = 8.314\,$K^{-1}·mol^{-1} the gas constant and $T = 298.13\,$K (constants from [3]), the equation is simplified to:

$$p(h1) = p(ho) \cdot \mathrm{e}^{-1,146 \cdot 10^{-4} \cdot m^{-1} \cdot \Delta h}. \tag{A.81}$$

For the pressure $p(h1)$ measured by the weather station, the pressure $p(h0)$ at the measuring point in the laboratory can now be calculated for a height difference of $(44.67 \pm 0.05)\,$m as $p(h0) = (993.1 \pm 1.1)\,$mbar. Therefore the measured value for the chamber pressure is $p_{ch} = p_{out} + p_w = (1085.9 \pm 1.2)\,$mbar.

B. Drawings, Schematics and Hardware Setup Specifications

B.1. VV30 Amplifiers

Table B.1.: Calibration factors for the analog amplifiers (VV30) of the 18 channels box and FADC channels for different setups: A = wires measurement, B = source measurement. Mean calibration value $(284.4 \pm 0.2)\,\text{mV}$.

A	B	chan.	# amp.	calibr. [mV] $\pm$ 0.2	corr. factor $\pm$ 0.002
x	1-7	0	262	286.2	0.994
1-7	1-6	1	283	283.8	1.002
1-6	1-5	2	204	283.8	1.002
1-5	1-4	3	269	283.6	1.003
1-4	1-3	4	231	285.4	0.996
1-3	1-2	5	140	284.6	0.999
1-2	1-1	6	228	283.2	1.004
1-1	1-0	7	213	283.8	1.002
1-0	x	8	137	285.8	0.995
0-1	0-1	9	234	284.0	1.001
0-0	0-0	10	167	283.4	1.004
x	x	11	265	285.6	0.996
0-4	0-4	12	273	283.4	1.004
0-3	0-3	13	148	284.0	1.001
0-2	0-2	14	158	284.4	1.000
0-7	0-7	15	227	284.2	1.001
0-6	0-6	16	173	285.8	0.995
0-5	0-5	17	242	284.6	0.999

Table B.2.: Calibration factors for the analog amplifiers (VV30) of the 16 channels box and FADC channels for micromegas measurement. Mean calibration value $(284.4 \pm 0.2)\,$mV.

FADC chan.	chan.	# amp.	calibr. [mV] $\pm$ 0.2	corr. factor $\pm$ 0.002
1-7	0	182	283.8	1.002
1-6	1	165	284.6	0.999
1-5	2	125	283.2	1.004
1-4	3	206	286.0	0.994
1-3	4	222	285.4	0.996
1-2	5	224	285.2	0.997
1-1	6	230	283.0	1.005
1-0	7	176	283.8	1.002
x	8	108	283.8	1.002
0-1	9	139	283.0	1.005
0-0	10	146	286.0	0.994
x	11	113	283.0	1.005
0-4	12	121	285.6	0.996
0-3	13	104	285.4	0.996
0-2	14	117	286.2	0.994
0-7	15	135	283.8	1.002
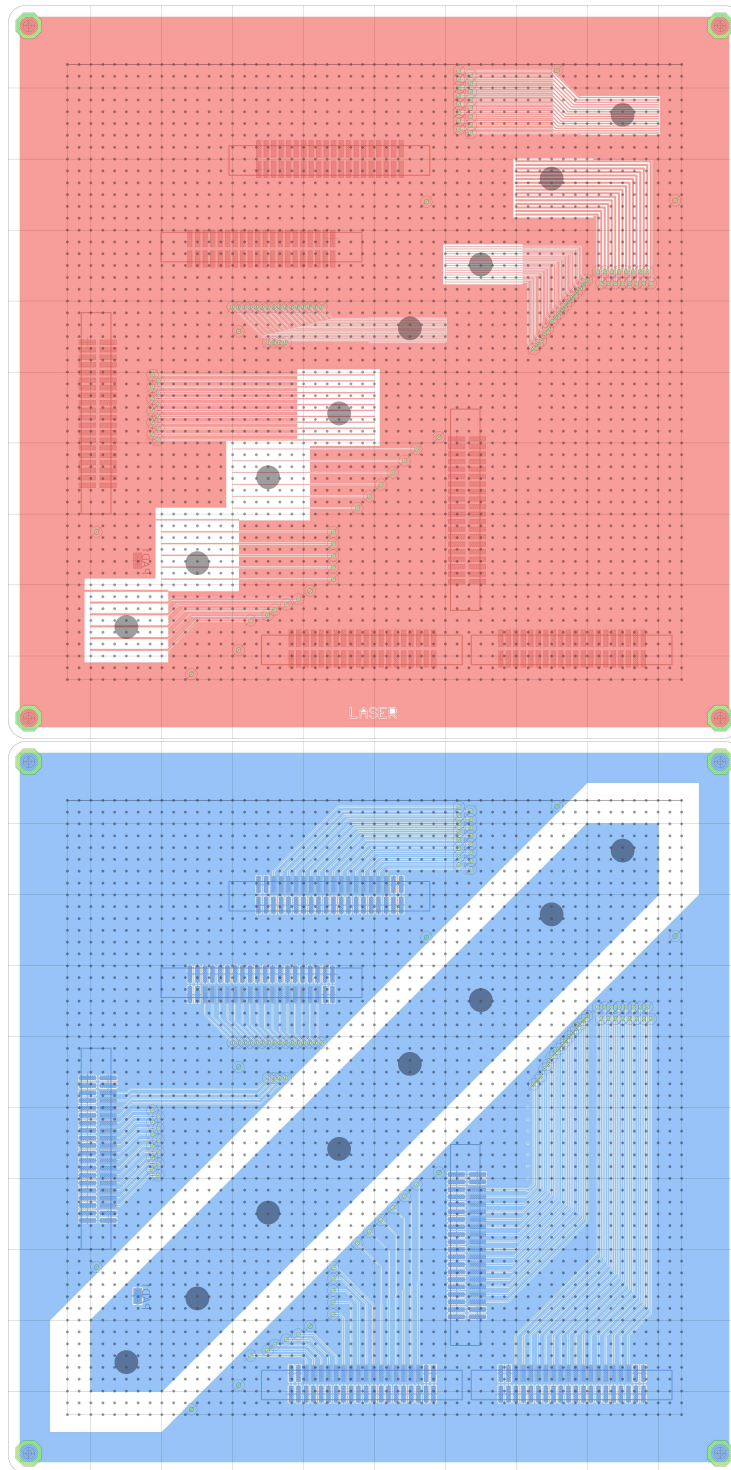
Figure B.1.: Board layout of the Micromegas test candidate, top (top picture) and bottom side (lower picture). Designed with the layout program EAGLE.
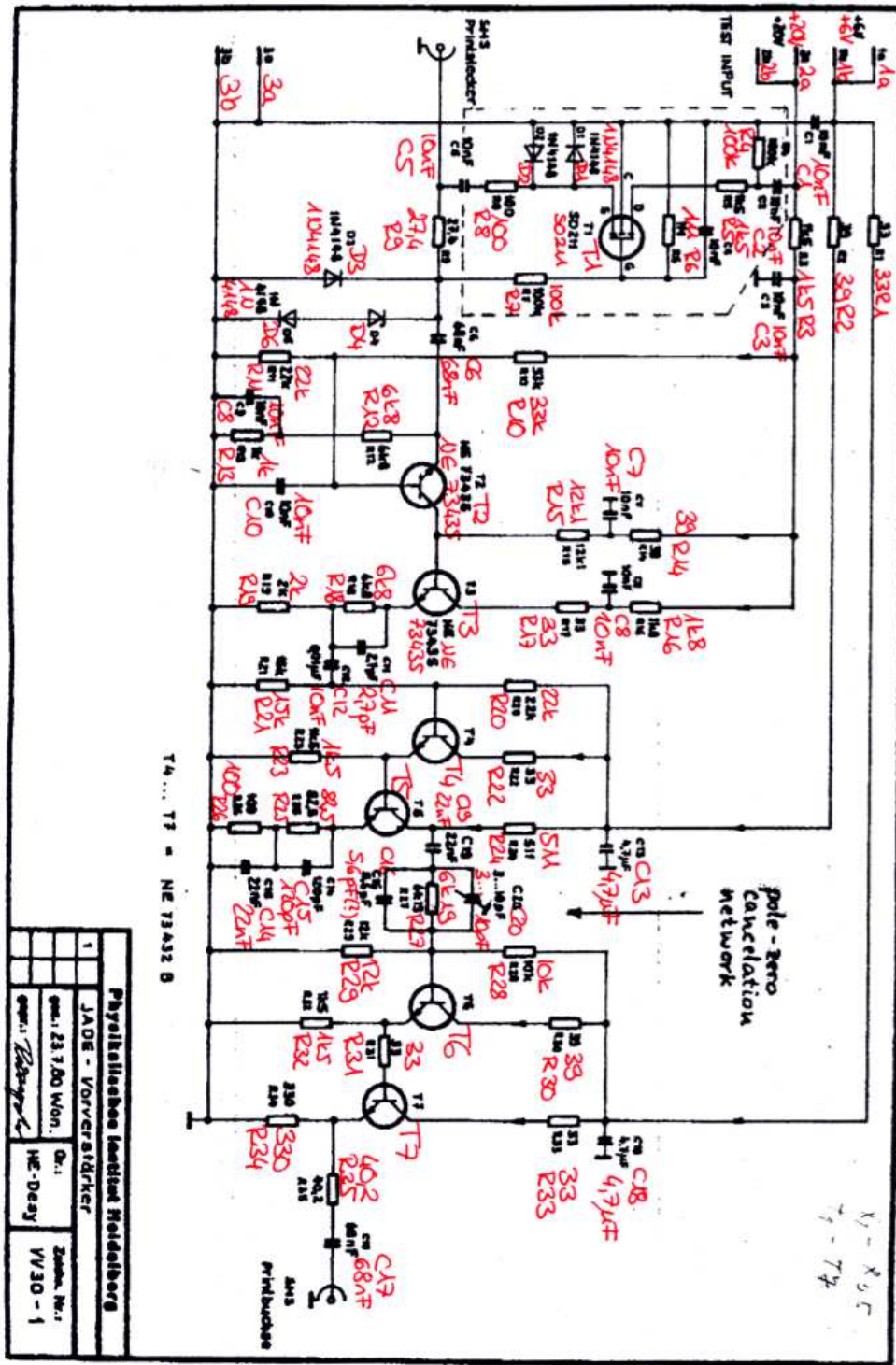
Figure B.2.: Schematic of the VV30 amplifier by Universität Heidelberg with annotations.

Bibliography

[1] K. Temming, G. Herten, U. Landgraf, W. Mohr, S. Weber, and S. Zimmermann, *A setup to study properties of Micro-Pattern Gaseous Detectors with laser-photoelectrons*, in *Nuclear Science Symposium and Medical Imaging Conference (NSS/MIC), 2011 IEEE*, pp. 88–91. 2011.

[2] K. Temming, G. Herten, U. Landgraf, W. Mohr, and S. Zimmermann, *Studies of micromegas chambers using UV-laser-photoelectrons*, in *Nuclear Science Symposium and Medical Imaging Conference (NSS/MIC), 2012 IEEE*, pp. 1768–1771. 2012.

[3] Particle Data Group Collaboration, J. e. a. Beringer, *Review of Particle Physics*, Phys. Rev. D **86** (Jul, 2012) 010001. `http://link.aps.org/doi/10.1103/PhysRevD.86.010001`.

[4] ATLAS Collaboration, G. Aad et al., *Observation of a new particle in the search for the Standard Model Higgs boson with the ATLAS detector at the LHC*, Phys.Lett. **B716** (2012) 1–29, `arXiv:1207.7214 [hep-ex]`.

[5] ATLAS experiment, *ATLAS SUSY exclusion limits summary plot*, 2013 (24.09.). `https://twiki.cern.ch/twiki/pub/AtlasPublic/CombinedSummaryPlots/AtlasSearchesSUSY_SUSY2013.pdf`.

[6] CMS experiment, *CMS SUSY exclusion limits summary plot*, 2013 (24.09.). `https://twiki.cern.ch/twiki/pub/CMSPublic/SUSYSMSSummaryPlots8TeV/barplot_blue_orange_SUSY2013.pdf`.

[7] ATLAS group (ATLAS Experiment © 2013 CERN), *Photo website*, 2013. `http://atlasexperiment.org/photos/index.html`.

[8] The ATLAS Collaboration, *The ATLAS Experiment at the CERN Large Hadron Collider*, Journal of Instrumentation **3** (2008) no. 08, S08003. `http://stacks.iop.org/1748-0221/3/i=08/a=S08003`.

[9] *ATLAS muon spectrometer: Technical Design Report*. Technical Design Report ATLAS. CERN, Geneva, 1997.

[10] Particle Data Group, *Particle Adventure*, 2012. `http:www.particleadventure.org/component_detector.html`.

[11] *ATLAS level-1 trigger: Technical Design Report*. Technical Design Report ATLAS. CERN, Geneva, 1998.

[12] T. Kawamoto, S. Vlachos, L. Pontecorvo, J. Dubbert, G. Mikenberg, P. Iengo, C. Dallapiccola, C. Amelung, L. Levinson, R. Richter, and D. Lellouch, *New Small Wheel Technical Design Report*, Tech. Rep. CERN-LHCC-2013-006. ATLAS-TDR-020, CERN, Geneva, Jun, 2013. ATLAS New Small Wheel Technical Design Report.

[13] The LHC Higgs Cross Section Working Group Collaboration, S. Heinemeyer et al., *Handbook of LHC Higgs Cross Sections: 3. Higgs Properties*, `arXiv:1307.1347 [hep-ph]`.

[14] F. Sauli, *Principles of Operation of Multiwire Proportional and Drift Chambers*, p. 92, CERN. CERN, Geneva, 1977. CERN 77-09, Geneva, 1975 - 1976.

[15] S. König, *Ageing studies for the ATLAS MDT Muonchambers and development of a gas filter to prevent drift tube ageing*. PhD thesis, Albert-Ludwigs-Universität Freiburg, 2008.

[16] C. Grupen and B. Shwartz., *Particle Detectors*. Cambridge University Press, 2008. `http://dx.doi.org/10.1017/CBO9780511534966`.

[17] W. Diethorn, *A methane proportional counter system for natural radiocarbon measurements*. PhD thesis, USAEC Report NY06628 and doctoral dissertation, Carnegie, 1956.

[18] M.Aleksa, *Performance of the ATLAS Muon Spectrometer*. PhD thesis, Technische Universität Wien, 1999.

[19] W. Blum and L. Rolandi, *Particle Detection with Drift Chambers*. Springer Verlag Berlin Heidelberg, 1983.

[20] H. Raether, *Electron Avalanches and Breakdown in Gases*. Butterworth & Co., 1964.

[21] F. Sauli, *Gas detectors: Achievements and trends*, Nucl. Instrum. Methods Phys. Res., A **461** (Jun, 2000) 47–54. 21 p.

[22] F. Sauli, *GEM: A new concept for electron amplification in gas detectors*, Nuclear Instruments and Methods in Physics Research Section A: Accelerators, Spectrometers, Detectors and Associated Equipment **386** (1997) no. 2-3, 531 – 534. `http://www.sciencedirect.com/science/article/pii/S0168900296011722`.

[23] J. Townsend, *Electrons in Gases*. (Hutchinson's scientific and technical Publications). Hutchinson, 1948. `http://books.google.de/books?id=NOafAAAAMAAJ`.

[24] S. Brown, *Basic Data of plasma physics: 1966*. M.I.T. Press, 1967. `http://books.google.de/books?id=hzJRAAAAMAAJ`.

[25] H. Fulbright, *Ionization Chambers in Nuclear Physics*, in *Nuclear Instrumentation II / Instrumentelle Hilfsmittel der Kernphysik II*, E. Creutz, ed., vol. 8 / 45 of *Encyclopedia of Physics / Handbuch der Physik*, pp. 1–51. Springer Berlin Heidelberg, 1958. `http://dx.doi.org/10.1007/978-3-642-45903-0_1`.

[26] E. Schudt, G. Weitz, K. Hellwege, H. Landolt, R. Börnstein, and O. Madelung, *Landolt-Börnstein Zahlenwerte und Funktionen aus Naturwissenschaften und Technik: Neue Serie*. Springer, 1971. `http://books.google.de/books?id=TAO6AQAAIAAJ`.

[27] S. Biagi, *Magboltz Website*, 2012. `http://consult.cern.ch/writeups/magboltz/`.

[28] F. W. Bubb, *Direction of Ejection of Photo-Electrons by Polarized X-rays*, Phys. Rev. **23** (Feb, 1924) 137–143. `http://link.aps.org/doi/10.1103/PhysRev.23.137`.

[29] S. Xie, *A Gas Monitoring Chamber for ATLAS MDTs*. PhD thesis, Albert-Ludwigs-Universität Freiburg, 2011.

[30] S. Weber, *Aufbau einer Messkammer zur Bestimmung der Eigenschaftenvon Micro-Pattern Gaseous Detectors mittels Photoelektronen*, Master's thesis, Albert-Ludwigs-Universität Freiburg, 2011.

[31] W. Haynes, D. Lide, and T. Bruno, *CRC Handbook of Chemistry and Physics*. CRC Handbook of Chemistry and Physics. CRC Press, 2012. `http://books.google.de/books?id=-BzP7Rkl7WkC`.

[32] R. Veenhof, *Garfield 9 Website*, 2010. `http://garfield.web.cern.ch/garfield/`.

[33] CERN, *CERN lib epio*, 1993. `http://wwwasdoc.web.cern.ch/wwwasdoc/WWW/epio/epiomain/epiomain.html`.

[34] The ROOT development team, *ROOT Website*, 2013. `http://root.cern.ch/drupal/`.

[35] G. Audi, O. Bersillon, J. Blachot, and A. H. Wapstra, *The Nubase evaluation of nuclear and decay properties*, Nuclear Physics A **729** (Dec., 2003) 3–128.

[36] Particle Data Group Collaboration, R. e. a. Barnett, *Review of Particle Physics*, Phys. Rev. D **54** (Jul, 1996) . `http://pdg.lbl.gov/pdg_96.html`.

[37] NIST National Institute of Standards and Technology, *stopping-power and range tables for electrons*, 2013-11-13. `http://physics.nist.gov/PhysRefData/Star/Text/ESTAR.html`.

[38] E.Mathieson, *Induced Charge Distributions in Proportional Detectors*. Brookhaven National Laboratory, 1990. `http://www.inst.bnl.gov/publications/Mathieson.shtml`.

[39] Uni Heidelberg, *Datasheet VV30 amplifier*, 1989. `http://www.physi.uni-heidelberg.de/Einrichtungen/EW/Geraete/VV030_Vorverstaerker/VV30_Man.PDF`.

[40] Ö. Şahin, I. Tapan, E.N. Özmutlu, and R. Veenhof, *Penning transfer in argon-based gas mixtures*, Journal of Instrumentation **5** (2010) no. 05, P05002. `http://stacks.iop.org/1748-0221/5/i=05/a=P05002`.

[41] T. Z. Kowalski and A. R. Stopczyński, *The gas gain process in Ar/CO2 filled proportional tubes*, Nuclear Instruments and Methods in Physics Research Section A: Accelerators, Spectrometers, Detectors and Associated Equipment **323** (1992) no. 1-2, 289 – 293. `http://www.sciencedirect.com/science/article/pii/016890029290305N`.

[42] D. Binnie, *Drift and Diffusion of Electrons in Argon CO-2 Mixtures*, Nucl.Instrum.Meth. **A234** (1985) 54.

[43] V. Rehmann, *Messung der Gasverstärkung und Untersuchung von Alterungseffekten in Driftröhren*, Master's thesis, Albert-Ludwigs-Universität Freiburg, 1996.

[44] G. Schultz, *Etude d'un détecteur de particules à très haute précision spatiale (chambre à drift). Analyse des phénomènes physiques liés au fonctionnement de ce détecteur.* PhD thesis, Louis Pasteur U., Strasbourg I, Geneva, 1976. Presented on 8 Jul 1976.

[45] Uni Freiburg, *Wheather Station Uni Freiburg*, 2013. `http://www.mif.uni-freiburg.de/stationlive/`.

[46] W. Demtröder, *Experimentalphysik 1*. Experimentalphysik / Wolfgang Demtröder. Springer, 2008. `http://books.google.de/books?id=wD453JJ6nusC`.

[47] NASA, *Earth Facts*, 2013. `http://nssdc.gsfc.nasa.gov/planetary/factsheet/earthfact.html`.

List of Figures

Acknowlegments

I would like to thank many of my colleagues for all the support that I got during the work for this thesis.

In particular I want to thank Prof. Gregor Herten and Prof. Ulrich Landgraf for giving me the possibility to write my PhD thesis in this working group and also for the interesting PhD topic within an international collaboration like the ATLAS community.

I owe many thanks to my supervisor Prof. Ulrich Landgraf for his ongoing support and encouragement in this research project. He always offered me expert guidance and was open for discussions and questions.

I am very glad that Stephanie Zimmermann who agreed to act as a second advisor for this thesis also helped me with my ATLAS authorship qualification.

Special thanks go to Bernhard Pfeifer and Jürgen Tobias. Without their highly qualified work and help the technical part of this project would not have been possible. I also owe thanks to the whole teams of the mechanical and electronic workshops of the University of Freiburg for their help in realizing my projects.

Many people at CERN also supported this thesis. I want to thank Rui De Oliveira for providing the possibility to get the Micromegas test candidate manufactured in his workshop and special thanks go to Antonio Teixera for helping me during the design and manufacturing process. Furthermore a special acknowledgement goes to Rob Veenhof for having the patience of a saint while helping me with questions regarding my Garfield simulations and also for giving me the possibility to participate in the Garfield simulation workshop.

I am deeply grateful to Wolfgang Mohr for his interest in my work and the numerous and fruitful discussions we had and of course for the ski lessons. I am very happy that I had a great time with Sabrina Bernhard in our girl-power office. I definitely need to thank Kathrin Störig for her incredible nerves and patience helping me with programming and computer issues and teaching me how to fight the bits and bytes (though they still fight back, sometimes).

I would also like to thank all people who supported me in writing this thesis and did the proofreading and corrections, especially Stephanie Zimmermann and Andrea Di Simone.

Last but not least, I would like to thank all colleagues, friends and everybody that I may have forgotten above. This thesis would not have been possible without the support of my family and good friends.